THE DESIGN AND SYNTHESIS OF HETEROGENEOUS CORE SHELL NANOMATERIALS FOR BIOLOGICAL APPLICATIONS

BY NICHOLAS PASQUALE

A dissertation submitted to the

Graduate School-New Brunswick

Rutgers, The State University of New Jersey

In partial fulfillment of the requirements

For the degree of

Doctor of Philosophy

Graduate Program in Chemistry and Chemical Biology

Written under the direction of

Professor Ki-Bum Lee

And approved by

_____

_____

_____

_____

New Brunswick, New Jersey

May 2017

ABSTRACT OF THE DISSERTATION

The Design and Synthesis of Heterogeneous Core Shell Nanoparticles for

Biological Applications

By

NICHOLAS PASQUALE

Dissertation Director:

Professor Ki-Bum Lee

Nanomaterials are a unique class of materials that operate at the same size scale as cellular structures, providing a unique advantage for the study and manipulation of biological systems. Inorganic nanoparticles, in particular, have unique physical and chemical properties associated with them that provide them a unique and powerful advantage in biological applications. For example, metal nanoparticles, most popularly gold, possess plasmonic properties which provide them with imaging, sensing, and therapeutic modalities. Magnetic nanoparticles, on the other hand, although capable of MRI imaging, are a powerful class of materials owing to their ability to respond to magnetic fields. This allows for the manipulation of biological structures in space and time, providing researchers the ability to control cell signaling and behavior.

Over the recent years, researchers have sought to incorporate multiple physical properties into a single nanoparticle, creating a highly multifunctional and versatile therapeutic platform. This has led to the rise of core-shell nanoparticles, where normal core nanoparticles have an additional inorganic shell material grown over their surface.

This imbues the nanoparticle with multiple materials properties, allowing for advanced and novel applications in biomedicine.

The application of core-shell nanomaterials, and nanomaterials in general, in biological settings requires the careful design of the material to imbue it with properties appropriate for the application at hand. In the first third of this thesis, magnetic core gold shell nanoparticles are incorporated into a novel platform for the delivery of a potent anti-cancer peptide (ATAP), and the synergistic application of magnetic hyperthermia. To this end, we demonstrate that the MCNPs provide an ideal anti-cancer platform, circumventing the poor solubility and high IC_{50} of ATAP. Moreover, besides enhancing the anti-cancer properties of ATAP, the magnetic core allowed for the application of magnetic hyperthermia, which we showed to act in synergism with ATAP. Furthermore, the plasmonic gold shell allows for the facile surface functionalization of tumor targeting ligands, to imbue the system with targeted delivery. Moreover, the plasmonic gold shell allows for dark field imaging to track the delivery of the MCNPs and ATAP.

In the second third of this thesis, magnetic core mesoporous silica shell nanoparticles are utilized for stem cell based gene therapy. The core shell nanoparticles in this case provide a means to deliver a heat inducible plasmid encoding TRAIL, a cancer-specific therapeutic protein. After engineering stem cells, which possess tumor homing capabilities, by delivering this plasmid using magnetic core mesoporous silica shell nanoparticles, the magnetic core can be used to apply magnetic hyperthermia. This allows for the site-specific activation of TRAIL in response to magnetic hyperthermia, which is shown to induce significant cancer cell death.

In the final third of this thesis, a novel heterogeneous core shell upconversion nanoparticle architecture was developed to enhance the upconversion efficiency of the

iii

material at low power excitations. This is done by separating the photon harvesting atoms and luminescent lanthanides, to which the energy is transferred, into separate shells in an individual nanoparticle. This serves to mitigate any energy transfer away from the luminescent centers to other atoms. This architecture results in a significant enhancement in upconversion luminescence at low power excitations as compared to other UCNP architectures. Moreover, we demonstrate the utility of this novel UCNP design by constructing a sensitive UCNP FRET-based biosensor capable of detection at three orders of magnitude lower concentrations than most UCNP FRET-based biosensors.

Overall, this thesis has demonstrated the design and synthesis of three multifunctional inorganic core shell nanoparticles for cancer therapy and biosensing: 1) magnetic core gold shell based anti-cancer therapy, 2) magnetic core mesoporous silica shell stem cell engineering for cancer therapy, and 3) heterogeneous core shell upconversion nanoparticles for controlling energy migration for enhanced luminescence and sensitive biodetection.

Acknowledgements

This work, of course, was only possible due collaboration and help from others. I would like to thank my advisor, Professor Ki-Bum Lee, who was instrumental in my success in graduate school. I would not have not been able to see this through to the end without his help and concern. Dr. Lee was always genuinely concerned with my, and everyone's future. I cannot express enough gratitude at my fortune to have worked under an advisor who thought about my future as much, or more, than I did.

I would like to thank Perry Yin, Prasad Subramaniam, and Birju Shah and Jinping Lai who helped me tremendously when I first began my graduate career. They were always there to answer questions, show me techniques, and guide me in the right direction. They made my introduction into graduate school much easier and I will always remember their help and kindness. In particular, Perry was instrumental in helping me prepare for interviews and secure my first job. He provided me with advice and guidance even after he had left the lab – For that I will be forever grateful.

I would like to thank Kholud Dardir and Hudifah Rabie for being excellent friends, lab mates, and peers. They were always around to help me out and cheer me up when things got difficult. I will always appreciate their genuine kindness.

Lastly, but in no way least, I would like to thank my family. My parents sacrificed their entire lives from the moment my siblings and I were born to ensure we had good lives. I cannot possibly understand the magnitude of their love and sacrifice for us, but I will always appreciate it. Similarly, my sisters were always there to cheer me up and take care of me whether I needed it for not. I am truly fortunate to have been blessed with such a loving family. I would also like to thank my grandmother and my aunt.

Unfortunately, they are not here to witness me go through this exciting milestone in my

life, but I do this, and everything, with them in my heart, hoping to make them and

everyone in my family proud.

Chapter 3: Stem Cell-Based Gene Therapy Using Magnetic Core-Mesoporous Silica Shell Nanoparticles and Hyperthermia to Enhance the Treatment of Cancer

List of Figures

Chapter 1:

Introduction

The text and images used in this chapter have been previously published, at least in part, as referenced in the figure.

1.1 An Introduction to Inorganic Nanomaterials

Inorganic nanomaterials have gained significant momentum over the last decade due to their interesting physical and chemical properties. These properties, such as luminescence, magnetism, and plasmonics, have attracted great interest in biological and medical applications, leading to the emergence of a new interdisciplinary field known as "nanomedicine". Nanomedicine is proving to be a powerful set of tools for the diagnosis, treatment, and study of various diseases due to their unique materials properties. Among the different types of nanomaterials, plasmonic, magnetic, luminescent and high surface area nanomaterials have shown to be the most advantageous in medical diagnosis and treatment. For example, plasmonic nanomaterials have found great utility as biosensors, owing to the exquisite environmental sensitivity displayed by the local surface plasmon resonance (LSPR) of the material. Magnetic nanomaterials are currently enrolled in several clinical trials for cancer targeted therapy and imaging[5,6] and have already been FDA approved for their use as extremely sensitive MRI contrast enhancement reagents[7]. Similarly, luminescent nanomaterials have made great strides in advancing the fields of *in vivo* bioimaging and biodetection[8].

All of these materials have been shown to work in tandem and synergistically with high surface area nanomaterials, such as mesoporous silicates, which allow for extremely high loading capacities of various reagents such as medical diagnostic and therapeutic

agents. More interestingly, their ability to deliver high concentrations of payloads can be regulated using clever surface chemistry which, in conjunction with magnetic and luminescent modalities incorporated into the same platform, has led to the development of release systems which can be triggered by external cues which are orthogonal to typical biophysical cues, such as irradiation with light or magnetic fields. As such, the design and synthesis of different heterogeneous core-shell nanomaterials has become an exciting and quickly growing field within nanomedicine, and has made a profound impact on the ability to design complex, yet highly tunable systems capable of biological regulation through external orthogonal triggers.

1.1.1 Plasmonic (Gold) Nanomaterials

The synthesis of gold nanoparticles has been developed by a number of groups
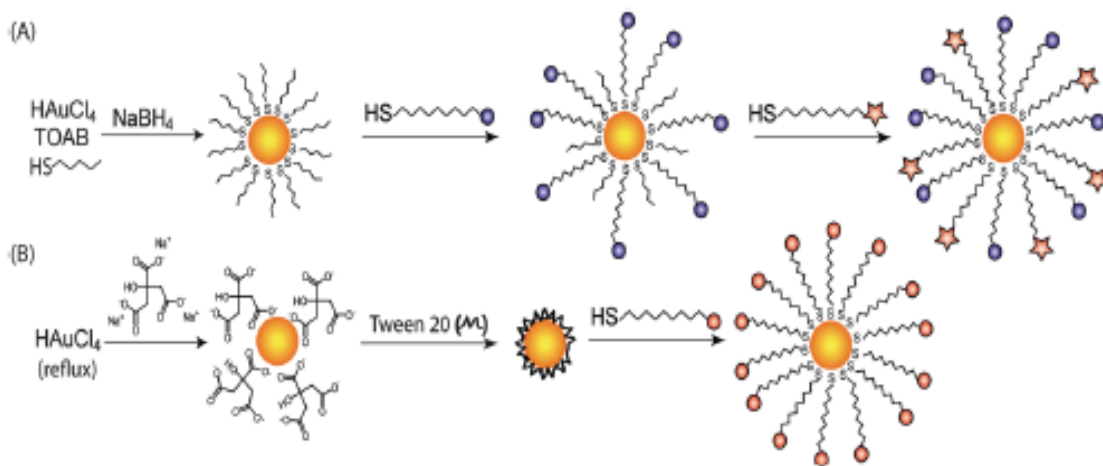
Scheme 1.1.[3] Synthesis of Gold Nanoparticles. A) Biphasic Brust-Schriffin synthesis of Au nanoparticles. Simple post-synthesis thiol exchange for functionalization B) Citrate reduction method, where citrate acts as the reducing agent and capping ligand. Subsequent exchange with alkanethiols in the presence of Tween buffer as an intermediate.

allowing exquisite control over their size[9], morphology[10], and surface functionality[3]. The original synthetic method for making Au nanoparticles was developed by Turkevich et. al. in 1951 and consists of the reduction of hydrogen tetrachloroaurate ($HAuCl_4$) in boiling water with trisodium citrate[11]. In this synthetic protocol, citrate acts as both the

reducing agent and surface ligand to cap the growth, and stabilize the surfaces of the resulting Au nanoparticles. Upon injection of sodium citrate into the boiling gold salt solution, the reaction turns a deep blue purple, indicating the initial nucleation of gold clusters with long "tails", reminiscent of nanowires. Upon boiling for 10 minutes, these gold structures coalesce into spherical nanoparticles via diffusion-mediated crystal growth. This protocol was further refined by Frens to include size control by varying the gold to citrate ratio, resulting in excellent size control from 10-20 nm, though particles as large as 100 nm can be prepared[12]. In this procedure, adding more citrate will result in the formation of smaller particles due to the better stabilization of their higher energy surfaces at higher citrate concentrations. It was later determined that an additional, third major role of citrate in facilitating the size control of Au nanoparticles, besides acting as a reducing agent and surface stabilization ligand, is its ability to control the pH of the reaction.[13] However, despite the simplicity and control afforded by this synthetic route, it often requires the exchange of the citrate ligand for more functional ligands such as 11-mercaptoundecanoic acid (MUA). Unfortunately, the ligand exchange from citrate to MUA can be problematic and result in irreversible aggregation.[14]

To address these limitations, in 1994, Brust and Schriffin created a breakthrough in the synthesis of Au nanoparticles by using a biphasic reduction method involving alkanethiols as the capping ligand.[15] In this synthetic protocol, tetraoctylammonium bromide (TOAB) is used as a phase transfer reagent to aid in the transport of the reducing agent, sodium borohydride, and gold salts from the aqueous to organic phase where the alkanethiols are partitioned. This procedure allows for the synthesis of extremely monodisperse Au nanoparticles from 1.5 to 5 nm by varying the gold to thiol ratio, concentration of reducing agent and reaction temperature. This biphasic reduction serves to control the nucleation and growth kinetics via regulation over the reduction rate

and concentration of the Au precursors in organic solvent. Compared to the citrate

reduction method, alkanethiol-protected Au nanoparticles possess much higher stability,

longer shelf life, and can be repeatedly dried and redispersed without aggregation. This

enhancement in stability originates from the relatively strong gold-thiol interaction, and

the van der Waals interactions between the hydrophobic portions of the alkane chains

(hydrophobic interactions).[16,17] Moreover, the presence of alkanethiols enables for a

facile thiol exchange procedure at the surface of the Au nanoparticles to functional

ligands such as MUA. This is a very large advantage as it allows for a simple and

efficient aggregation-free method to prepare the Au nanoparticles for bioconjugation for

biomedical applications.[18]

Upon reduction in size of metal materials toward the nanoscale their surface

properties begin to dominate, leading to the rise of LSPR specific for each material.[19] For

example, gold nanoparticles possess an intense absorption typically centered around
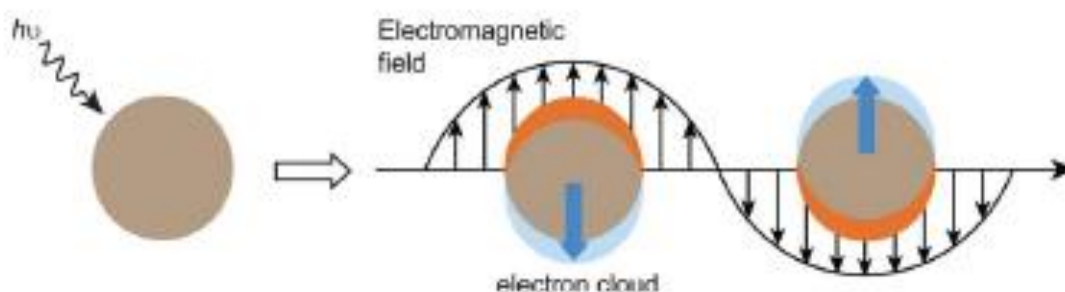
Figure 1.1.[3] Illustration of the collective oscillation of the electron cloud associated with the surface of gold nanoparticles in response to absorption at their LSPR.

520 nm, while silver absorbs near 410 nm. This difference in LSPR is due to the

differences in refractive index and dielectric constant between the materials.[20]

Interestingly, it is also possible to modulate the LSPR of materials based on their size

and morphology. For example, by increasing the size of metal nanomaterials it is possible to red-shift the LSPR. The increase in size causes a decrease in the frequency of oscillation of the electrons associated with the metal surface around the nanoparticle. Similarly, a change in the morphology of metal nanoparticles also has interesting effects on the LSPR.[21] When going from a spherical gold nanoparticle to a gold nanorod, there now exist two LSRPR modes known as transverse and longitudinal modes. These are consequences of the long and short axis of the nanorods and result in the generation of two LSPR peaks, one associated with each axis, where the longitudinal axis is red-shifted as compared to the transverse (shorter) axis.[22] In order to synthesize nanorods, rather than nanoparticles, cetyltrimethylammonium bromide (CTAB) is used typically in the synthesis. The bromide ions have a higher affinity for the facets of gold nanocrystals, causing anistropic growth to take place, resulting in rod-like particle morphologies.[23]

In addition to their LSPR, metal nanomaterials, especially gold, have been widely used as extremely efficient quenchers of luminescence, allowing for more versatility in biosensor design.[24] Their ability to act as extremely efficient luminescent quenchers derives from their intense LSPR absorptions, which can undergo FRET based energy transfer with donor molecules and materials.[25] Conversely, their strong LSPR absorptions can act as extremely intense signal amplifiers for surface enhanced Raman (SERS) based biodetection schemes.[26] Raman scattering is based on the inelastic scattering of photons, and as such, is extremely weak in signal as compared to the prototypical Raleigh elastic scattering measured in FTIR.[27] However, because the Raman scattering is based on the vibrational and rotational characteristics of the particular analyte, it is often used to provide a spectral "fingerprint" of analytes, allowing it to be highly specific at the expense of its sensitivity.[28] In order to address the weak signal from Raman scattering, the LSPR of gold nanomaterials are widely used to

enhance the signal of Raman using SERS, due to the overlap of the LSPR absorption and the SERS signals. Hence, the SERS amplification signals from gold serve to provide the sensitivity necessary for biosensing experiments. This is particularly true in clusters of gold nanoparticles, where the close proximity of the neighboring Au nanoparticles causes the overlap of the LSPR associated field lines, increasing their amplitude and leading to larger SERS enhancements.[29]

These interesting plasmonic properties have found great utility in the realm of biosensing.[30] Since the LSPR of these materials are so sensitive to the environment (changes in the refractive index and dielectric constant) they are often used to construct biosensors. There are two common methods for the construction of such LSPR based biosensors : i) Aggregation based assays, where the state of aggregation (change in size of the metal cluster) causes a shift in the LSPR that can be monitored in response to analyte binding[31] and ii) SERS-based assays, where the particles elicit a 10^6-10^{10} increase in signal, allowing for rapid, sensitive, label-free detection.[32] Between these two methods, there also exist two ways of constructing such biosensors: i) Surface-based methods where the particles relative distance from some chip surface changes in response to analyte binding, resulting in a change in the LSPR intensity[33], or ii) Solution-based methods where the metal nanoparticle is bound to another inorganic material or organic dye, which will typically be quenched by the gold nanoparticle surface. Upon analyte binding, the linkage is broken between the metal and the quenching material/chromophore, causing a return of fluorescent signal.[34]

Besides biosensing, gold nanoparticles have also been extensively used in bioimaging.[35] Gold nanoparticles are extremely efficient at scattering visible light, and as a result, are excellent probes for dark-field microscopy. For example, gold nanoparticles conjugated to Respiratory Synctial Virus have been used to monitor and track the

invasion of HEp-2 (human epidermis larynx carcinoma) cells in real time. Dark field

imaging has also been extensively utilized to monitor the uptake of nanoparticles into

cells to track the successful delivery of therapeutic payloads into cells.[36]

Au nanoparticles have a plethora of properties that make them powerful tools in

the fields of biotechnology and nanomedicine. Their wide range of surface

functionalities, ease of synthesis, highly tunable LSPRs, strong quenching/amplification

of fluorescence, and ability to efficiently scatter light have made them invaluable

biosensing and imaging tools.

1.1.2 Mesoporous Silica Nanomaterials

In 1992 scientists at the Mobil Oil discovered highly ordered mesoporous silica

materials and quickly recognized it as an important material that would have a profound

impact in a number of fields.[37] A variety of interesting physical properties such as i)

extremely large surface area (700-1500 m^2/g), ii) high chemical and thermal stability, iii)

ease of surface functionalization, and iv) biocompatibility make them ideal supports for

applications such as catalysis, adsorption, and biotechnology.[38] Since their discovery,

much effort has gone into optimizing synthetic routes which yield large scale control over

their physical properties with particular emphasis on pore size, particle size, and

morphology.[38] The synthesis of mesorporous silica nanoparticles (MSNs) typically

occurs under highly alkaline conditions (pH=11) to catalyze the hydrolysis of the silica

precursor.[39] The most commonly used silica precursor in the synthesis of MSNs is

tetraethylorthosilicate. Due to the poor leaving ability of the ethoxy groups, TEOS

requires these highly basic conditions to catalyze its hydrolysis and polymerization, as

well as heat (typically ~70-80 $^\circ$C is used). The templating of the mesoporous structure is

based on the formation of liquid-crystalline micellar mesophases by surfactant

molecules, the most typical which is CTAB. Since the diameter of CTAB micelles is 2-3 nm, the resulting pore diameter in MSNs is in register with the size of the CTAB micelles.[38] The surfactant in these reactions is typically kept at low concentrations (mM range) to make the structuring of the ordered mesophase dependent on the electrostatic interactions between the cationic amino group of CTAB and the anionic charge associated with the polymerizing silica oligomers. Once the polymerization is complete, resulting in crystalline hexagonal-pore mesoporous silica nanoparticles, the CTAB micelles must be removed to create accessible pores. This is typically done through calcination or refluxing under acidic ethanol.[40]

It is also possible to control the pore size of MSNs via the use of "swellants". Popular swellants include toluene, and 1,3,5 trimethyl benzene. Depending on the molecular size of the swellant is has been shown that researchers are capable of controlling the pore size from 10-20 nm.[41] This is particularly useful when considering the loading, transportation and delivery of a large biologics such as proteins.

In addition to control over the size of the pores, MSNs are often functionalized to enhance their adsorption properties with regards to the analyte(s) of interest. Moreover, there are two surfaces one can consider functionalizing: the inner mesoporous surface, as well as the outer surface of the MSNs. In order to functionalize the outer surface of MSNs one can simply adopt a post-synthetic grafting strategy since the exterior surface is kinetically more accessible than the internal surfaces of the mesoporous structure. This is especially true if the post-synthetic grafting is done before removal of the surfactant.[42] In this strategy, the purified MSNs are reacted, typically under some heat in dry ethanol or toluene overnight, with functional organoalkoxysilanes such as aminopropytriethoxysilane (APTES) for decorating the exterior surface with primary amines, or mercaptopropyltriethoxysilane (MPS) for decoration of the exterior surface

with thiols. In order to functionalize the interior mesoporous surface in MSNs it is necessary to adopt a co-condensation strategy.[38] In this method, the organoalkoxysilane is added into the synthesis in the presence of CTAB, NaOH, and TEOS, allowing them to undergo co-condensation polymerization. It is also possible to selectively functionalize, to an extent, the inner and outer surfaces of the MSNs. This is because more hydrophobic organoalkoxysilanes will prefer to orient themselves into the CTAB micelles during the polymerization, thus functionalizing the inner mesoporous walls with hydrophobic ligands. Meanwhile, more hydrophilic organoalkoxysilanes can be used in the same reaction to selectively impart the exterior surface with hydrophilic functionalities, which tend to be more amenable towards further functionalization (APTES, MPS, etc.). In order to enhance the partitioning of hydrophobic organoalkoxysilanes into the pores, while maintaining hydrophilic grafting on the exterior surface, one can also add a small amount of organic reagent to the reaction during post-functionalization, such as butanol. This will better partition the hydrophobic organoalkoxysilanes into the mesopores by better solvating them in the hydrophobic interior environment, promoting their site-selective hydrolysis and functionalization.[43]

This ability to selectively functionalize MSNs makes them particularly attractive for the transportation and delivery of therapeutic molecules in nanomedicine.[44] The majority of small molecule therapeutics are relatively hydrophobic, which can contribute to a relatively higher EC_{50}. However, by encapsulating these hydrophobic therapeutics into high surface area mesoporous silicas, whose adsorption capacity can be increased by functionalization of the inner pores with the appropriate organoalkoxysilane, the EC_{50} of hydrophobic therapeutics can be improved greatly.[45] Furthermore, by selectively grafting the outer surface of MSNs with ligands amenable toward functionalization, it is possible to "cover" or "cap" the pores to increase the retention time and lower the

leakage of the therapeutic loaded MSNs. More interestingly, there have been many

demonstrations of the ability of researchers to design cleaver "nanovalve" systems,

whereby the covered pore can be selectively opened in response to a number of

different stimuli such as light and different redox and pH conditions.[46]

As one example, MSNs loaded with small molecules were capped by CdS

quantum dots.[44] The MSN exterior surface had been functionalized by MPS, allowing the
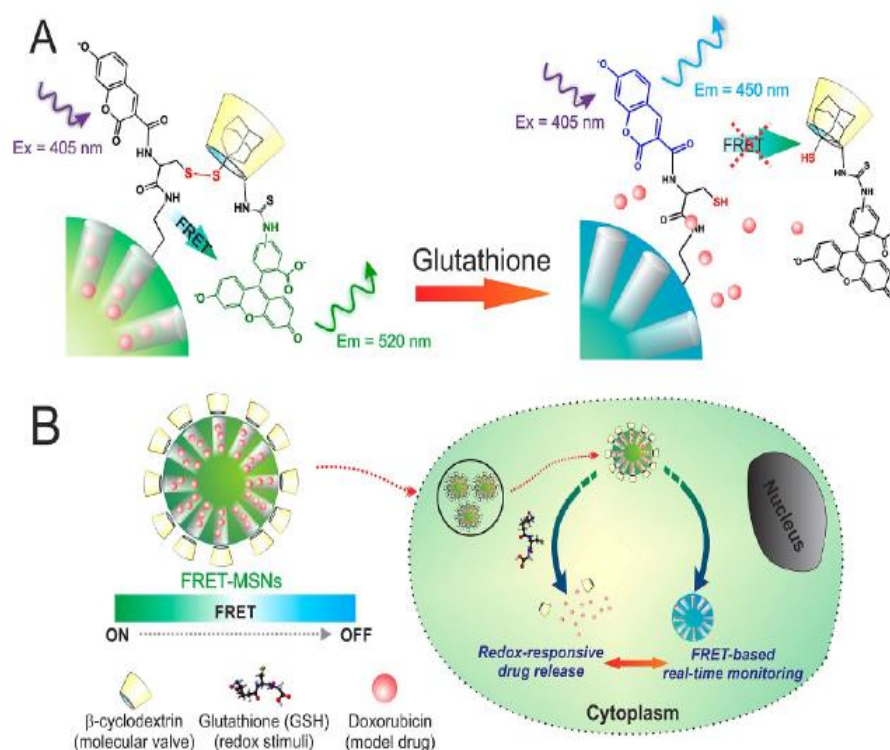
Figure 1.2.[1] MSN-FRET Based Monitoring of Drug Delivery. A) (Left) The FRET system is intact, due to the retention of the disulfide bond. (Right) Upon disulfide reduction to thiols, the FRET signal is lost B) Upon entering the cell cytoplasm, where there are high concentrations of Glutathione, the disulfide bond is cleaved, diminishing FRET, and releasing the drugs while allowing for estimating the dose released.

use of free thiol groups for the conjugation of the thiol capped CdS quantum dots via

disulfide linkages. Since the CdS quantum dots physically blocked the mesopores, it

mitigated leakage of drug, allowing for long-term and on-demand kinetic release profiles.

Upon exposure to reducing chemicals such as glutathione, which is present in the 1-10

Mm concentration range in the cellular cytoplasm, the disulfide bond is reduced and cleaved, allowing the CdS quantum dots to diffuse away and the drug to diffuse out of the pore. This design has been exploited many times for the delivery of therapeutics on demand to the cellular cytoplasm with minimal prior leakage.

To take this type of redox-responsive linker a step further, our group has shown the design of MSNs also capable of reporting the release event in cells.[1] This was accomplished by making cysteine-modified coumarin functionalized MSNs which could then be conjugated to adamantanethiol via a redox-responsive disulfide linkage. The pores were then efficiently capped by (fluorescein isothiocyanate) FITC-β-cyclodextrin (complexing with adamantanethiol) until they were transported into the highly reducing cytoplasm of cells. While outside of the cell, with the linkage intact, there was efficient FRET from the coumarin donor to the FITC acceptor. Then, upon cleavage in the cytoplasm, the FITC-β-cyclodextrin diffuses away, allowing a recovery of coumarin based emissions. This clever design allowed for the real-time monitoring of uncapping-release kinetics without the need for model drugs, whose profiles are often very different from each other based on the kinetic diameter, solubility, and interactions with the pore walls.

Other than redox-responsive linkers, such as disulfides, there have been many examples of photolabile linkers. One such example is the use of coumarin derivative-guest β-cyclodextrin-host capping system. This complex blocks the pores, but the carbamate bond holding the coumarin to the nanopore is cleaved in response to 2 photon stimulation at 800 nm.[47]   Rather than using the concentration of chemicals to control the release kinetics of cargo, which is cumbersome and impossible in practical clinical applications, the use of light as a trigger presents a unique advantage. By

controlling the power density of excitation, it is possible to control the number of
nanocaps which are cleaved from the surface of the MSNs. This presents the
experimenter additional control over the release profile.

As the linker systems used for the release of therapeutics from MSNs become
more complicated they better allow us to study and control complicated physiologic
processes such as endocytosis or the response of different tumor types to various drug
release kinetic profiles. In particular, these materials have great potential in the
intracellular release of biological materials due to the potential incorporation of external
stimuli which act orthogonally to biological systems, yielding exquisite non-invasive
control over biological processes.

1.1.3 Magnetic Nanomaterials

Due to their unique and interesting magnetic properties, and their large-scale
utility in material and biological applications over the last few decades, magnetic
nanoparticles, and in particular iron oxides, have been synthesized by a number of
different established synthetic methods.[48] The most popular protocols for the synthesis
of iron oxides include the co-precipitation of divalent and trivalent iron salts,
hydrothermal synthesis, the hot-injection method and thermal decomposition.

Co-Precipitation

The co-precipitation of ferric and ferrous ions is the most traditional method for
the synthesis of iron oxide nanoparticles.[49] This is typically done under highly alkaline

conditions at room or elevated temperatures- often under a nitrogen atmosphere. The reaction mechanism can be summarized as:

$$Fe^{2+}_{(aq)} + 2Fe^{3+}_{(aq)} + 8OH^-_{(aq)} \leftrightarrow Fe(OH)_{2(aq)} + 2Fe(OH)_{3(aq)} \rightarrow Fe_3O_{4(s)} + 4H_2O_{(l)}$$
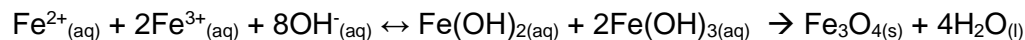
Due to the presence of OH^- in the reaction mechanism, pH plays an important role in the synthesis of MNPs via co-precipitation. When the pH is lower (typically below 11) the nucleation of MNPs is more thermodynamically favorable, whereas at higher pH (typically above 11) the growth of MNP nuclei into nanoparticles is thermodynamically favored.[50] This is due to the fact that the hydroxyl group, as one of the reactants to form the precursors to iron oxide nuclei, will be present at lower concentrations for lower pH values. As such, growth cannot dominate, resulting in the nucleation of small sub-nanometer iron oxide clusters. However, at higher pH values, there is an abundance of hydroxyl groups throughout the reaction medium, yielding a steady supply of $Fe(OH)_x$, which can supply the growing iron oxide nanoparticles with a steady supply of 'monomer'. By varying reaction conditions such as pH, temperature, and time it is possible to control the size of the resulting MNPs from 2-25 nm.[50] Additionally, this synthetic method was the first to produce MNPs in gram-scale quantities, making it highly attractive for industrial scale synthesis. However, co-precipitation has several draw backs such as difficulty in controlling the i) particle size, ii) morphology, iii) phase, and iv) composition due to the complex equilibria involved in the aqueous based synthesis, the use of different types of iron salts (chlorides, perchlorates, sulfates, nitrates, etc.), the pH value of the solution, and v) the phase of the resulting iron oxide due to the low reaction temperatures as a result of the low boiling point of water.[50] Furthermore, the resulting particles are highly aggregated due to the lack of surface ligands besides hydroxyl groups which do not sufficiently lower the surface energy of the particles so as to occlude their aggregation, making them unsuitable for biological

applications.[51] Moreover, the particles are also poorly crystalline, resulting in low M_s

values and poor performance in biological and material applications. One way to

enhance the M_s values is to anneal at high temperatures (~1000 ^{o}C). These high

temperatures provide the means to overcome the energy barrier for the rearrangement

of atoms within the crystal lattice, resulting in phase changes from the alpha or gamma

phase, to the highly crystalline and ordered Fe_3O_4 phase.[52] However, annealing tends to

worsen the aggregation of the MNPs, resulting in a large increase in the size of the MNP

aggregates towards several hundred nm. In an attempt to produce higher quality Fe_3O_4

nanocrystals, the hydrothermal synthetic route was developed to allow for the use of

high reaction temperatures.

Hydrothermal

Hydrothermal synthesis is similar to co-precipitation except that it often occurs at

or near neutral pH and involves the crystallization of substances under high temperature

(~130-250 ^{O}C) and vapor pressure (~0.3-4 MPa) aqueous conditions in a sealed Teflon

lined container.[53] Advantages of hydrothermal synthesis over co-precipitation involve the

use of high temperatures and pressures to overcome the thermodynamic potential

necessary for the creation of highly crystalline phases which possess superior M_s, such

as α-Fe_2O_3, γ-Fe_2O_3, and Fe_3O_4. In particular, it allows for the growth of crystal phases

which are not stable at their melting point, as well as materials which have high vapor

pressures at or near their melting points. Moreover, it allows for facile control over the

composition of different types of iron oxides.[54] Also, similar to co-precipitation, due to the

solubility of various ions in aqueous medium and the preference that different ions

possess for particular crystal facets during the growth of MNPs, hydrothermal synthesis

can afford the user a high degree of control over the morphology of the resulting

nanoparticles. However, this method suffers from similar limitations as compared to co-

precipitation. Although the resulting MNPs typically undergo better phase control and have higher M_s values, as well as better dispersity in water due to the ability to perform synthesis in the presence of capping ligands – most often polymers such as poly(vinylpyrrolidone) (PVP), they often still possess fairly high polydispersity and inferior M_s values when compared to particles made by more recently optimized synthetic methods. As a result, particles made via the hydrothermal synthetic method, similar to co-precipitation, often require annealing at high temperatures, to obtain high M_s values, affording them with strong magnetic properties which are necessary for materials science and biological applications.

Thermal Decomposition

The above aqueous phase synthetic routes involve complex equilibria and therefore do not offer precise size control or narrow size distributions. Furthermore, they often require annealing of the resulting particles to increase the M_s, which inevitably strips the ligands from the surface, leading to irreversible particle aggregation. To circumvent these limitations, the organic phase thermal decomposition method was developed. Originally, this method was coined as the 'hot injection' method because it involved the injection of metal precursors into hot (200-300 ^{O}C) organic solutions.[55] This effectively shortened the nucleation phase of the reaction such that all crystal nuclei simultaneously formed upon injection and then immediately entered the growth phase in unison. This method affords extremely high control over particle size and yields very narrow size distributions.[56] However, this protocol typically involves violent reaction conditions due to the injection of room temperature liquid precursors into extremely hot solvent/surfactant mixtures. Accordingly, researchers developed the 'heat-up' method, where the organic solvent, surfactant, and organometallic metal precursors are heated up in a one pot reaction.[57] In this reaction scheme, the temperature is initially held above

(typically ~200 ^{O}C) the decomposition temperature of the metal precursors (typically ~165 ^{O}C) before heating to higher temperatures (260-300 ^{O}C) to promote particle growth. This has the effect of separating the nucleation stage (burst nucleation) after the thermal decomposition of the metal precursors to form metal oleates, from the growth stages where smaller crystals dissolve due to Ostwald Ripening and coalesce to form larger singly crystalline MNPs.[55] As such, the particles, similar to the hot-injection method, all finish nucleation together at lower temperatures, and enter the growth stage in a commensurate fashion when elevated to higher temperatures to allow an extremely high degree of control over particle size with narrow size distributions. Furthermore, the high temperatures used in the presence of surfactant afford the crystallization of highly magnetic and monodisperse Fe_3O_4 MNPs.[58] This abrogates the need for high temperature annealing, which irreversibly aggregates the particles. Furthermore, thermal decomposition affords a facile means for controlling the doping of particles, which is important for engineering the magnetic properties of the MNPs. For example, it is known that by doping Zn^{2+} into Fe_3O_4 dramatically increases the M_s value by replacing Fe^{3+} in tetrahedral holes, causing the Fe^{3+} to replace the Fe^{2+} in the octahedral holes. This serves to partially disrupt antiferromagnetic coupling between tetrahedrally positioned Fe^{3+} and octahedrally positioned Fe^{3+} in the cubic inverse spinel structure of Fe_3O_4. Due to the change of composition, the $Zn^{2+}_x Fe^{2+}_{(1-x)2} Fe^{3+}O_4$ nanoparticles actually change to a spinel structure.[59] The small size and the ability to easily dope the iron oxides, by just replacing some of the Fe^{2+} with Zn^{2+}, allows the facile engineering of their magnetic properties. This makes MNPs extremely versatile in materials science and biological applications. As such, it is critical to understand the origins of the magnetic properties of these single domain magnetic particles in order to understand the different types of

magnetism that can arise depending on the resulting size, shape, and particle composition.

Magnetic Properties of MNPs

Arguably, one of the most interesting aspects of nanoparticles is the 'quantum confinement effect', whereby upon reduction in size past a critical limit the quantum mechanical properties of the material dominate over the bulk.[60] This is especially true of magnetic nanoparticles when the particle size becomes comparable to single magnetic domains. Namely, bulk magnetic materials consist of many nanoscale magnetic domains, whereas nanoparticles can consist of as little as few to a single magnetic domain.[61] This leads to two interesting types of magnetic behavior, which play very important roles in biological and materials applications: i) single domain ferromagnet nanoparticles, and ii) single domain superparamagnetic nanoparticles.

Similar to bulk ferromagnetic materials, an array of single domain magnetic nanoparticles will exhibit magnetic hysteresis which is dependent upon the applied field.
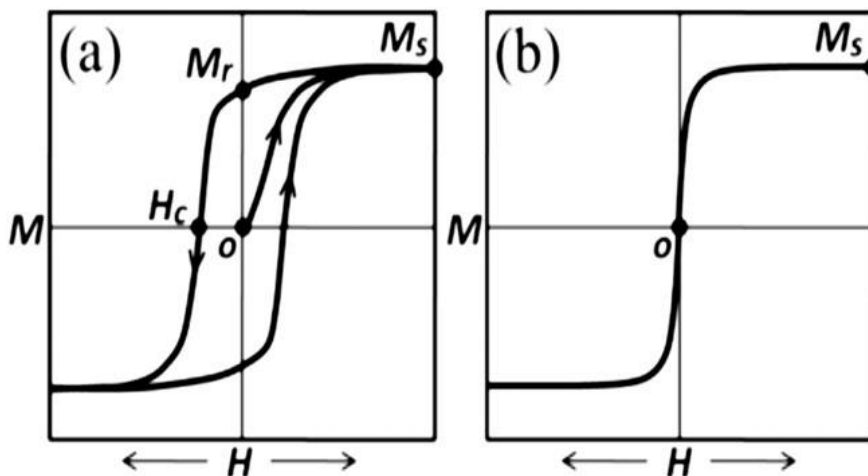
Figure 1.3. Hysteresis of MNPs.[2] A) Expected hysteresis loop for an array of single domain ferromagnetic nanoparticles and B) an expected hysteresis curve for superparamagnetic nanoparticles.

However, this magnetization vs field dependency operates upon different mechanisms when going from bulk ferromagnets to single-domain ferromagnetic nanoparticles. In bulk ferromagnetic materials, the magnetization increases with increasing field strength due to the growth of magnetic domains via domain wall movement, resulting in a net magnetization in the presence of an applied field.[62] However, in a single-domain particle array, the magnetic moment of each nanoparticle (or atom in the case of an array of atoms within a single nanoparticle) will interact with both the applied field and the single domain moments of its neighbors (given they are within a critical distance of one another) to align along the direction of the applied field.[63] When all of the moments are aligned along the applied field, this is known as the saturation magnetization (M_s). Upon the removal of the external field there remains a measurable magnetization of the sample. This is referred to as the remnant magnetization (M_r).[2] Field reversal in the direction opposite to that of the M_r causes the renewed randomization of the magnetic moments. The field necessary to bring the net magnetization of the sample to zero is known as the coercivity (H_c).[64] These terms contribute to the way in which the magnetization is cycled through the hysteresis loop, and is the main difference between traditional bulk ferromagnetic materials and an array of single domain ferromagnets. In short, in bulk ferromagnetic materials, the magnetization increases in response to the applied field due to domain wall nucleation and rotation as well as the rotation of the magnetization vector away from the easy axis of magnetization. However, in single-domain nanoparticles, there can be no domain wall movement due to their complete absence. Consequently, only coherent magnetization along the field lines is possible to overcome the effective anisotropy (K) of the particle.[65] Accordingly, in single domain

materials, the coercivity drops significantly. The critical diameter for a magnetic nanoparticle to reach the single domain limit is equal to

$$R_{sd} = 36\sqrt{AK} / \mu_o M_s^2$$

Where A is the exchange constant, K is the effective anisotropy constant, and M_s is the saturation magnetization.[66] For most magnetic material compositions, this size falls in the 10-100 nm range. However, there do exist examples of very high-anisotropy materials in the single domain limit which can reach several hundreds of nanometers.[66]

For single-domain magnetic nanoparticles, the amount of energy required to cross the energy barrier and reverse the magnetization from one stable configuration to the other is proportional to KV/k_bT, where V is the volume of the particle, k_b is Boltzmann's constant, and T is temperature.[67] If the thermal energy at or above room temperature is enough to overcome the energy barrier associated with the effective anisotropy energy, resulting in the abrogation of magnetization upon removal of the external field, the particle is said to be superparamagnetic. As a result of the return of the magnetization to zero in response to thermal fluctuations upon removal of the external field, both M_r and H_c are zero for superparamagnetic materials. This process is analogous to the behavior of electrons in traditional magnetic materials, except instead of applying to individual electron spins the collective magnetic moment of the entire particle is considered, giving rise to the term "superparamagnetism".[68]

Interestingly, it is possible, typically through control over the size and composition, to tune the magnetic properties of these materials, which find great utility in biological applications. One such important parameter to tune is known as the blocking temperature, T_B.[69] This is the temperature at which the thermal energy in the system can overcome the effective anisotropy energy. The blocking energy, as well as the coercivity,

have important implications for materials applications such as high density magnetic storage, as well as biological applications such as magnetically facilitated delivery to specific regions of the body or cell.[69]

High density magnetic storage media can be built upon an array of single domain ferromagnetic nanoparticles with high coercivity. In this case, the coercivity in response to the applied field leads to a remnant magnetization, M_r, which can be used as a sort of logic gate to store information based upon the value and presence of magnetization after the removal of the applied field.[70] Conversely, magnetic nanoparticles for biological applications are often better served by superparamagnetic nanoparticles. One such example is magnetically facilitated delivery, whereby superparamagnetic MNPs are injected intravenously, and are guided by an external magnetic field to the desired therapeutic site.[71] Once they are located at the therapeutic site they can be used to achieve local hyperthermia via their exposure to an alternating magnetic field (discussed in more detail below).[69] This has been shown to sensitize drug resistant cancer cells to chemotherapeutics, and has been used to facilitate the on demand delivery of therapeutic reagents.[72] Furthermore, superparamagnetic MNPs make ideal probes for MRI contrast enhancement, potentially providing very large enhancements in MRI signal.[73] For all of the aforementioned bioapplications of superparamagnetic MNPs, it is critical that there is no M_r or H_c after removal of the external field. In the case of freely diffusing MNPs, the application of an external field will cause the moments of the MNPs to tilt in plane, leading to their flocculation and aggregation, during, for example, magnetically guided delivery of particles to a disease site.[74] As such, it is of paramount importance that the particles are superparamagnetic in nature for biological applications as the irreversible (rather than reversible) aggregation of MNPs (as would be the case for single domain ferromagnets) would lead to difficulties in cell uptake and removal,

general cytotoxicity, poor renal and hepatic clearance, embolism and other associated adverse events.[75]

Besides simple magnetically-facilitated delivery, whether by holding a magnet near the disease site, or using complex computer generated magnetic field gradients to steer the particles through circulation, the superparamagnetism of MNPs allows them to be used for hyperthermia. This is when the particles, under the presence of an alternating magnetic field (AMF), release heat to the surrounding tissue. Both in vitro and in vivo it has been show that MNP enabled hyperthermia can achieve temperatures from 41-45 ^{O}C within an hour.[69,76] Hyperthermia works by taking advantage of the delay between the relaxation time of the magnetic moment of the MNPs and the relaxation time of the applied sinusoidal magnetic field lines. The relaxation moment of the particle depends on a number of factors such as the surface magnetic anisotropy, which is proportional to the particles surface area, and as such, holds special weight for nanoparticles. It also depends on the particles volume and composition.[69] When no magnetic field is present, the particles magnetic vector will align along the easy axis, which is the orientation of the magnetic moment in the particle that corresponds to an energy minimum. Then, under the application of an external magnetic field with a relaxation time slower than that of the MNPs, the magnetic moment of the MNPs will attempt to follow the field lines of the applied field. However, since their relaxation time is faster than that of the applied field, they will shed the excess energy in the form of heat in order to follow the applied field.[69,77] This causes extremely high increases in local temperature (up to 90 ^{O}C) in the surround nanovolume, which leads to an increase of the bulk solution temperature.[78] The achievable temperature with magnetic hyperthermia depends on the concentration of particles present, the time of the applied field, and the particle composition and size, as well as environmental factors, such as ionic strength of

the media and solution viscosity.[69] However, it remains possible to adjust the composition and size of the MNPs to tune their blocking temperature, which puts an upper limit on the achievable temperature with magnetic hyperthermia. This can act as a safe guard to avoid overheating and the damage of healthy tissue.

MNP-mediated hyperthermia has also been used to create an on demand delivery system to combat cancer using a hyperthermia-mediated drug delivery system.[79] In this work, by Yoo et al., they conjugated geldanmycin, an inhibitor of heat shock proteins (HSPs), to the nanoparticle surface using a thermosensitive azide-based covalent bond. After exposure to an AMF, geldanmycin was released via the thermally-mediated cleavage of the azide based linker, allowing for the inhibition of HSPs during hyperthermia. Without the protecting effects of HSPs in response to elevated temperature, the cancer cells could no longer evade hyperthermia-mediated apoptosis. The interesting physical properties of MNPs has embedded their use in the fields of nanomedicine and materials science. Moreover, when combined with other materials, they allow for the design of even more interesting and intricate systems.

1.1.4 Luminescent Upconversion Nanoparticles

Luminescent materials such as quantum dots or fluorescent dyes typically undergo a Stokes-Shift, whereby they absorb light of a relatively shorter wavelength, and emit at longer wavelengths. These linear optical materials face severe challenges in biological applications due to the low penetration depth of UV-Visible excitations in biological tissues[80], severe photobleaching, photoblinking, and possibly photo-damage to organisms.[81] Moreover, most biological tissues exhibit a large auto fluorescent background in response to UV-Visible excitations, and as such, the signal to noise ratio of conventional probes are largely dampened.[82] Upconversion nanoparticles (UCNPs),

most famously NaYF$_4$, have the potential to overcome these challenges. They are typically inorganic in nature, and as such do not exhibit photobleaching or photoblinking due to the stability of their crystal structure and the energy levels of the luminescent atoms.[83] Furthermore, upconversion materials undergo Anti-Stokes shift processes, and emit UV-Visible light in response to near infra-red (NIR) excitations. As a result, the NIR excitations of these non-linear optical materials can penetrate much more deeply into biological tissues, with experiments showing a penetration depth of up to 2.5 cm.[84]

Until recently, these nanocrystals were typically synthesized via the annealing of cubic phase products, or hydrothermal procedures with very long reaction times to achieve β-hexagonal phase products, which have higher upconversion efficiencies (discussed below). Even still, the resulting products were a mixture of cubic phase and hexagonal phase, and often had large sizes and high polydispersity.[85] Efforts to improve the purity of hexagonal phase products with smaller sizes and narrow size distributions led to the development of thermal decomposition procedures.[86,87] However, the thermal decomposition of trifluoroacetate species (lanthanide trifluoroacetates) can produce HF vapors and fluorinated and oxyfluorinated species, which are highly dangerous. As such, all reactions carry extreme safety concerns.[87] Recently, Z. Li and Y. Zhang pointed out that it would be convenient and safe to convert all of the reactive fluoride species to solid-state products (small crystal nuclei) in solution at or near room temperature before the subsequent growth and Ostwald Ripening phase.[88] From their efforts, they developed a safe and robust way to synthesize UCNPs. In this method, lanthanide triacetates are heated at high temperature (150 ^{O}C) under vacuum in the presence of oleic acid and 1-octadecene (ODE) to form lanthanide-oleate precursors. Then, the reaction is cooled to room temperature and a mixture of NaOH and NH$_4$F (NaF) is injected into the reaction mixture. This results in the co-precipitation of lanthanide

oleates and NaF to form $NaLn_xF_4:Ln_yLn_z$. This is the point in the reaction at which small

crystal nuclei are formed. The reaction temperature is then raised and held at 50 ^OC to

promote the coprecipitation and nucleation of $NaYF_4$. From here, the reaction

temperature is raised, typically to 300 ^OC, to promote the Ostwald Ripening and growth

of β-hexagonal phase $NaYF_4$.[89] This co-precipitation type synthesis allows for excellent

size control from sub-10 nm UCNPs to 30 nm. Moreover, larger sized UCNPs can be

easily synthesized by using the UCNP cores from previous rounds of synthesis as seeds

in another reaction to promote epitaxial growth.

As previously mentioned, β-hexagonal phase $NaYF_4$ is the most popular
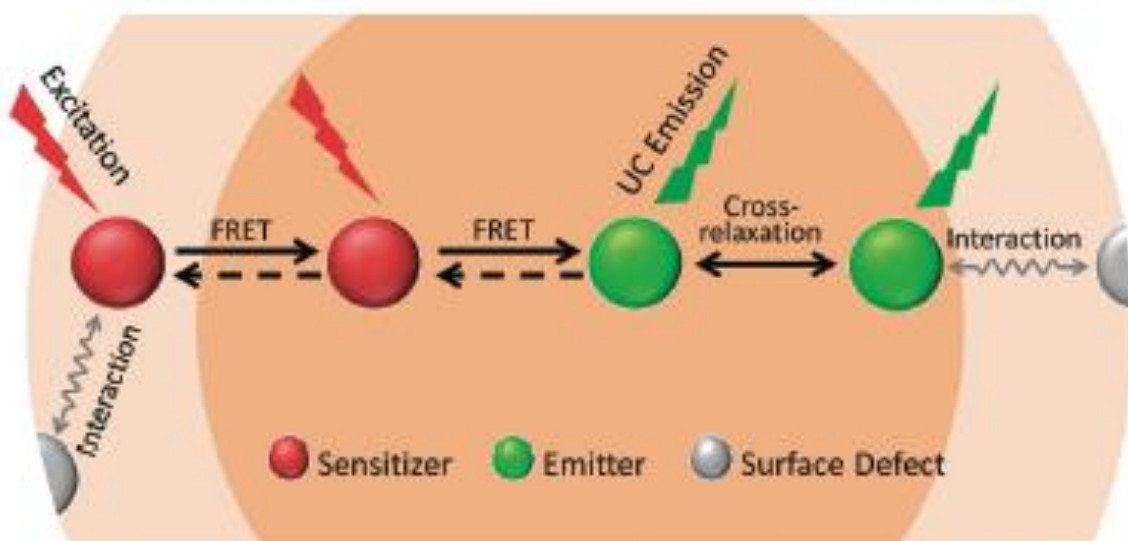
Figure 1.4.[4] Schematic illustration of the upconversion process in lanthanide doped $NaYF_4$ UCNPs.

upconversion host to date due to its low lattice phonon energies, and relatively higher

upconversion efficiency.[90,91] The β-hexagonal is preferred over the α-cubic phase as it

better distributes the lanthanides throughout its matrix, which reduces lanthanide

clustering. Furthermore, it changes the space group from P63/m to Fm3m. The lower

symmetry of the P63/m space group associated with β-hexagonal UCNP nanocrystals

allows for the removal of the degeneracy of free-ion states with a concomitant increase

in transition probabilities within the f orbitals of the lanthanide ions due to an increase in crystal field strength.[92] However, even though the lanthanides in $NaYF_4$ possess the ability to undergo f-f electronic transitions, resulting in UV-Visible emissions in response to NIR excitations, they possess small absorption cross-sections and no innate NIR absorption.[93] As such, $NaYF_4$ is typically co-doped with Yb^{3+} to synthesize $NaYF_4$:Yb/Ln, where the Yb^{3+} and Ln (Tm^{3+}, Er^{3+}, Ho^{3+}, etc.) replace a stoichiometric amount of Y in the lattice. In this system, Yb^{3+} endows the system with relatively 980 nm NIR absorption. After the ground state absorption in Yb^{3+}, the excited state electron transfers its energy via Forester Resonance Energy Transfer (FRET) to a neighboring Yb^{3+} ion within the lattice. Energy is transferred around the delocalized quasi-exciton Yb^{3+} sub-lattice of the crystal until it is transferred to an emitting lanthanide such as Er^{3+}, Tm^{3+}, or Ho^{3+}.[94] Here, the energy can either be transferred back to Yb^{3+} (energy back transfer), to another emitting lanthanide (cross-relaxation), or it can stay in the excited state long enough to absorb another quanta of energy to be promoted to the next available excited state, until it finally reaches an emitting state, resulting in its radiative decay. Of course, not all of the transitions perfectly match the energy of the 980 nm excitation, and as such there are some phonon-mediated energy transfer events.[93]

Cross-relaxation between emitting lanthanides is detrimental to luminescence and, as such, is kept at a minimum by using low concentrations of emitting lanthanides (typically <2 mol%) in order to separate them in space, making FRET between them unlikely, as it scales with distance to the inverse sixth power.[95] However, there have been fewer attempts to minimize energy back transfer from emitting lanthanides to Yb^{3+}, resulting in a decrease in luminescence resulting from transitions requiring a higher number of photons. The ability of lanthanides to undergo FRET-mediated multi-photon absorptions is due, in part, to their characteristically long lifetimes. Whereas organic

fluorophores and conventional fluorescent probes typically have lifetimes in the ns range, UCNPs (due to lanthanide-based composition) exhibit lifetimes that last for hundreds of microseconds to several milliseconds.[96,97] Furthermore, due to the electronic shielding of 4f orbitals by the 5d orbitals, the luminescence of the lanthanide ions does not depend on host material or environment as much as organic fluorophores. This also makes the positions of their ladder-like energy levels stable, resulting in narrow emission peaks which exhibit minimal (a few nm) blue or red-shifting.[98] Coupled with the enhanced tissue penetration of 980 nm NIR light from Yb^{3+} doping, UCNPs make ideal probes for biological applications.

Due to their interesting photophysical properties UCNPs have found utility in a wide range of applications in materials and biological sciences. Particularly, in biomedical applications, they have found strong utility as bioimaging agents and biosensors.[99] The suppression of autofluorescence and high penetration depth in biological tissues due to their unique NIR excitations garners them with very high signal to noise ratios, and as result, makes them ideal biological probes. For example, UCNPs have been used extensively as bioimaging agents to track cells and sub-cellular structures both *in vitro* and *in vivo*.[83,100,101] They have also been used extensively as fluorescent biosensors.[91,102,103] The suppression of autofluoresence enables UCNP-based biosensors to regularly reach nM sensitivities for various substrates and biosensor designs. Though UCNPs already possess interesting luminescent characteristics, their real power comes shines when designed as core-shell structures. This allows for the experimenter to modulate the energy migration dynamics within

UCNPs to tailor their photophysical properties for the desired application, as discussed in chapter 1.2.5.

1.2 An Introduction to Inorganic Core-Shell Nanomaterials in Biological Systems

Inorganic nanomaterials serve as interesting platforms in biological applications due to their unique physical properties such as LSPRs, high surface areas, magnetism, and upconversion luminescence. However, the true potential of inorganic nanomaterials is realized when they are designed as core-shell structures. Inorganic core-shell nanoparticles give researchers a vast toolbox of materials properties with which to mix, match, and modulate. The properties between the two materials can be additive, as with magnetic core-plasmonic shell nanomaterials. These materials will exhibit characteristics of both materials – they can be used as MNPs would with magnetically facilitated delivery, hyperthermia, etc.; however, they can also be used in a similar manner to gold for SERS, dark-field imaging and plasmonic applications. Another example includes the possibility to combine high surface area materials with either magnetic or luminescent triggers and gating mechanisms to make MSN-based drug delivery responsive to external stimuli. However, it is possible to design core-shell nanoparticles whose properties will synergize to allow previously unachievable control over materials properties. For example, in MNP@MNP and UCNP@UCNP architectures it becomes possible to tune the magnetism and energy migration dynamics, respectively, of the material in previously unachievable ways. This is the power of inorganic core-shell nanomaterials – It essentially expands the library of available materials and associated

properties researchers have available to them by making it possible to mix, match, and modulate several materials and their associated properties into one new material.

1.2.1 Magnetic Core-Plasmonic (Gold) Shell Nanomaterials

The integration of magnetic core-plasmonic gold shell nanoparticles allows researchers to manipulate the particles position in space using magnetic fields with simultaneous tracking from the plasmonic gold shell. This unique ability, in conjunction with their biologically comparable size, offers exciting new applications and areas in biological manipulation, imaging, and sensing. The design and synthesis of magnetic core-gold shell nanoparticles for biological applications requires several considerations as there is always a necessary trade-off, even under optimally designed architectures, between the physical properties emanating from the magnetic core and plasmonic shell. For instance, it has been demonstrated that the gold shell can be used for facile surface chemistry to capture analytes of interest.[104] The magnetic core can then be used to easily separate and concentrate the analytes followed by subsequent spectroscopy from the LSPR of gold to analyze the captured analytes. To properly design the nanoparticles one needs to ensure that the magnetic core is large enough as to have high M_s value for the efficient manipulation and separation of biomolecules through solvent or space.[105] However, it is also important to remember that the larger magnetic cores will red-shift the LSPR of the gold shell.[106] Then, one needs to consider the desired properties from the gold shell. Thicker gold shells add more non-magnetic weight to an individual nanoparticle, resulting in a decrease in M_s.[107] However, thicker gold shells also blue-shift

the location of the LSPR absorption spectra and enhance the intensity of absorption, as well as scattering.[108] Clearly, there is a need for compromise when synthesizing these particles and, as such, careful control and understanding of the synthetic conditions are necessary in order to control the physicochemical properties of the particles.

The synthetic challenges associated with MNP-Au core-shell nanoparticles are largely due to the large lattice mismatch between cubic Fe_3O_4 and cubic Au. This mismatch is upwards of 50%, causing the growth of the gold shell over iron oxide cores to be highly thermodynamically unfavorable.[109] As such, to get over the energy barrier, high temperatures are often used.[110] Upon return of the reaction to room temperature it is possible to isolate the kinetically-trapped core-shell structured product. The true thermodynamic products of the reaction will always be separate MNP and Au nanoparticles, as the high degree of lattice mismatch yields interfacial lattice strains on the GPa scale.[111] To kinetically isolate such a highly strained product requires careful control over the synthetic conditions. Among the most important are the reaction temperature and reaction time.[110] The high temperature promotes the desorption/readsorption of ligands (in the presence of excess ligand to prevent particle aggregation). It also controls the reduction rate of the metals, as well as their coalescence (via surface melting) into a complete shell.[110] If the reaction temperature is maintained for too long, the reaction will go over the energy barrier completely, trending towards thermodynamic products which are separate MNP and Au nanoparticles in solution. Despite the difficulties associated with the reaction, MNP-Au core-shell nanoparticles have attracted considerable attention due to their interesting physicochemical properties. As such, there has been a large effort towards synthesizing MNP-Au nanoparticles. Though there have been aqueous based synthetic protocols, these tend to yield poor size control over the resulting MNP-Au core-shell structure,

giving very large and aggregated particles. Additionally, due to the various aqueous

equilibria that exist, as well as the reaction's dependence on pH, aqueous based

synthetic protocols are extremely difficult to optimize and adapt. As such, organic based

syntheses are largely reported for the synthesis of monodisperse MNP@Au core-shell

nanoparticles of small size with uniform size-controlled gold shells. This is especially

important in aqueous-based protocols because if the particles grow too much and/or
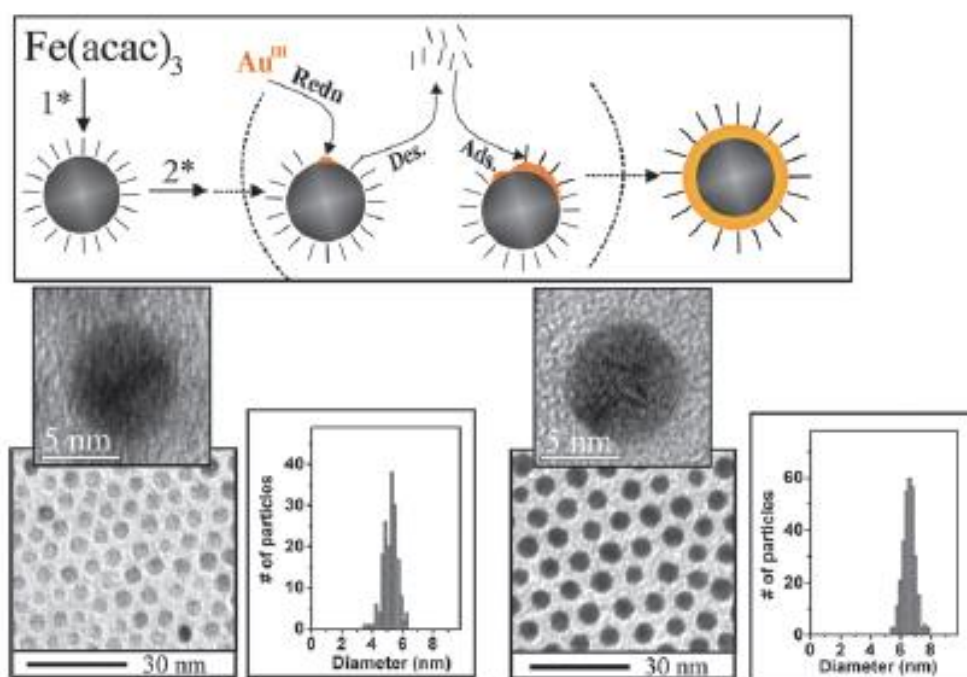
Figure 1.5. Synthesis of MNP-Au Core-Shell Nanoparticles via Molecular Precursors.
(Top Panel) Schematic of the synthesis of Fe3O4 nanoparticles (1*=reducing agent),
followed by the formation of Fe3O4-Au core-shell nanoparticles (2*=gold precursor,
reducing agent, capping agent, and temperature control) (Bottom Panel) TEM and
HRTEM images of Fe3O4 (left) and Fe3O4-Au (right) nanoparticles.

aggregate, they will be larger than the size scale of proteins and biomolecules, rendering them unusable for biological applications.

There are two main synthetic methods for synthesizing MNP-Au core-shell nanoparticles. The first involves the synthesis of MNP cores as seed nanoparticles. Then, a gold precursor (usually $Au(CH_3COO)_3$ or HAuCl4) is reduced under high temperatures (typically 180-200 ^OC) in the presence of surfactants such as oleylamine, oleic acid, and 1,2 hexadecanediol.[110] This synthetic strategy requires careful control over temperature as it dictates the kinetics of ligand desorption/readsoprtion, which allows Au access to the MNP seed surface. The temperature plays a further role by also controlling the kinetics of Au reduction. This is particularly important, as reduction kinetics which are too fast will promote the nucleation and subsequent growth of gold
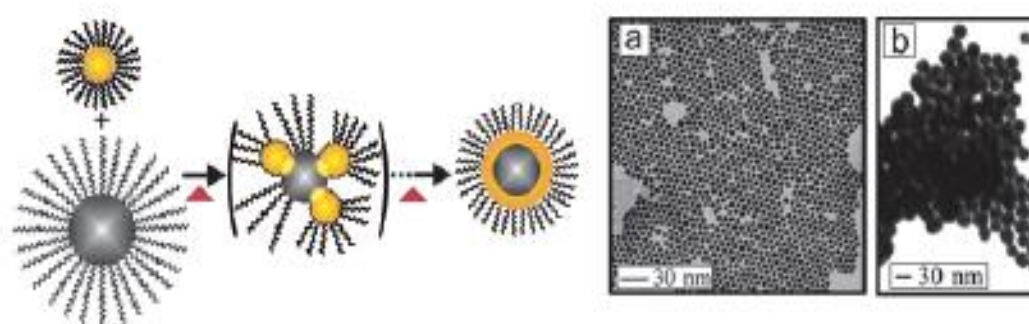
Figure 1.6. Synthesis of MNP-Au Core-Shell Nanoparticles via Au Nanoparticle Precursors.
(Left) Schematic of the heterogenesous inter-particle coalescence of Small Au seeds (1-2 nm) with iron oxide cores. (Right) TEM images of the core and core-shell particles.

nanoparticles in bulk solution. Rather, the ideal temperature of the reaction should promote the nucleation of gold seeds on the surface of the MNP cores. The high reaction temperatures also promote the melting and coalescence of the Au seeds into a uniform shell over the MNP surface. Bulk Au melts at 1,064 ^OC, but nanoparticles have significantly depressed surface melting temperatures.[112] The small sub-nanometer size of the Au seeds means that almost all of the atoms are surface atoms. This promotes

their rearrangement to deposit in register with the Fe_3O_4 crystal lattice, and undergo non-epitaxial growth via surface melting, coalescence, and the deposition of further gold atoms and seeds.

The second method involves the use of small pre-formed gold seeds (1-2 nm) and MNP cores under milder temperatures (140-160 $^\circ$C) in the presence of surfactant to promote ligand desorption/readsoprtion to the MNP core surface.[113] Upon initial adsorption of the Au seeds to the MNP core surface, they melt and coalesce into a gold shell. Because the size of the Au precursor in this reaction is 1-2 nm, as opposed to molecular precursors and subatomic clusters in the in-situ strategy discussed previously, the resulting gold shells tend to be much thicker than when molecular precursors are used. This has a tendency to further suppress the magnetic properties, namely Ms. However; it enhances the plasmonic properties of the Au shell, resulting in much more intense LSPR absorptions centered closer to 520 nm, due to the thicker shell. Moreover, the shell will also possess better light scattering abilities and larger SERS amplifications due to the more intense LSPR absorption.

In our own lab, we have adopted the former *in situ* protocol as it makes it possible to minimize the shell thickness on the resulting nanoparticles. This is desirable in biological applications because it provides the facile surface functionalization associated with Au nanoparticles due to the shell, but also retains a large portion of the M_s, while red-shifting the LSPR absorption from the gold shell. This is highly desirable as shorter wavelength UV-blue excitations can be more cytotoxic to cells than red light of comparable power density. Although it will minimize the ability of the particles to scatter light, we have already shown their viability as dark-field imaging agents in previous publications. Key to their translation into biological settings is the successful phase transfer of the MNP-Au core-shell particles from organic to aqueous phase. In our lab we

have adopted a sonication based procedure where the particles, suspended in a small amount of chloroform, are mixed in a concentrated tetramethylammonium hydroxide (TMAOH)/trisodium citrate solution. The sonication heats up the solution, evaporating the chloroform, while keeping the particles dispersed. The TMAOH acts to decrease the surface tension along the particle surface to promote ligand adsorption/desorption and stabilizes the particles with an electrical double layer, allowing citrate to easily come in and cap the surface.[114] From here, the particles can be easily capped with MUA, just as normal gold nanoparticles would be. This provides them with facile bioconjugation routes, allowing for their use in biological settings.

One of the first areas of application of MNP-Au core-shell nanoparticles was biological separations. The use of MNP-Au core-shell nanoparticles for biological separations originates from the well-established protocols used in molecular biology to separate DNA or proteins using labelled magnetic microbeads.[115] However, the gold shell now allows or facile surface functionalization to allow for flexibility of use.[116] For example, the MUA has a fee carboxyl ligand which can undergo EDC/NHS coupling to form amide bonds with proteins, peptides, or amino-labelled oligonucleotides, all of which possess primary amines. One study took this design further and utilized the SERS capabilities of the gold shell to analyze the bound biomolecules.[117] In this study, they coupled MUA-capped Fe_2O_3-Au core-shell nanoparticles to a gold surface using dithiobis(succinimidyl propionate) (DSP), forming a DSP-derived nanoparticle surface monolayer on top of the original bulk gold surface. IgG Antibody was bound to the MNP-Au core-shell particle surface via DSP coupling, forming an IgG antibody-coated surface. Then, the antibody-immobilized MNP-Au core-shell nanoparticles were reacted with Au nanoparticles capped with protein A, which was labelled with mercaptobenzoic acid (MBA), a SERS reporter probe. In order to further enhance the signal, a magnetic field was applied to the

sample, separating and concentration the magnetic core gold shell particles, bound to the SERS reporter through protein A. This allowed for an amplification in the SERS signal of the ring breathing modes of the MBA SERS reporter. This work was one of the first to demonstrate the viability of MNP-Au core-shell nanoparticles for bioseparation and biosensing.

1.2.2 MNP or UCNP Core-Mesoporous Silica Shell UCNPs

The design and synthesis of core-MSN shell nanoparticles offers exciting new methods for on demand drug release systems by integrating the high surface area and ability to tailor mesoporous silica surfaces to the desired applications, with the ability to remotely trigger the drug release using the properties of the core nanoparticle. The two systems that have attracted the most attention are MNP-MSN core-shell nanoparticles and UCNP-MSN core-shell nanoparticles. This is due to the unique ability of both core materials to be used as external, highly-penetrating cues for drug release which are orthogonal to biological systems. This is a particularly powerful advantage, as it allows for the remote triggering of biological events with minimal perturbations to baseline cellular processes.

Part of the reason for the extensive research surrounding these interesting core-shell structures is their ease of preparation. The synthesis of MNP or UCNP core-MSN shell nanoparticles follows very typical conditions for MSN synthesis, except with the addition of CTAB-coated cores added into the reaction mixture. This procedure was in large part pioneered by Taeghwan Hyeon.[118] To ensure the synthesis of monodisperse core-MSN shell nanoparticles it is important to start with initially monodisperse CTAB-coated core nanoparticles. To accomplish this, sonication is typically used and is the most effective means of doing phase transfers to ensure monodispersity. For this

process, a probe type sonicator is typically used at 400W power, with the probe on/off

for 1/1 second, to prevent rapid solution heating, which can lead to aggregation. To

further prevent this, it can be advantageous to further modulate the solution temperature

with an ice bath. After the small amount of chloroform used to suspend and transfer the

core nanoparticles has been evaporated, and the particle-CTAB mixture thoroughly

sonicated, the off duration in the on/off profile of the probe is increased to slowly bring

the solution temperature, with the help of the ice bath, back down to room temperature.

The resulting CTAB-coated nanoparticles are typically centrifuged to remove any

aggregates that may have formed. This is typically very minimal to none. The synthesis

conditions are best constructed such that the amount of core to be coated in the reaction

(typically ~5mg in 500 uL or less of chloroform) is present in the initial sonication, and is

then mixed with ~15 mL of water and ~1g of CTAB for sonication. This entire mixture,

after removal of aggregates, is then diluted to 50 mL of water and brought to pH=11 at

70 $^{\circ}$C. Then, 500 L of TEOS is slowly added into the reaction mixture, typically with the

aid of a syringe pump. Then, after the finial TEOS addition, the reaction temperature is

held for at least 4 hours. Then, the solution is cooled, and the particles are collected by

repeated rounds of centrifugation and washing in ethanol.[76,118]

For UCNP-MSN nanoparticles, extraction of CTAB from the pores can be carried

out under acidic ethanol conditions (typically pH=1) or using an ion exchange approach.

This is typically done with ammonium nitrate under reflux or room temperature

conditions for 3 rounds at 3-4 hours each. However, the ion exchange method is the only

viable procedure for extracting MNP@MSN nanoparticles.[119] The acidic ethanol

conditions will cause the particles to be etched, leaving behind hollow MSNs, with a cavity the size of the original core nanoparticle.

The relative ease of and robust nature of the synthesis has allowed this interesting core-shell structure to be utilized extensively in research. MNP@MS structures have been extensively used for magnetic resonance imaging (MRI) contrast enhancement.[118] These particles allow for excellent sensitivity in MRI, even though the magnetic properties are slightly dampened by the MSN shell. This is because the mesopores of the MSN shell allow for the diffusion of water molecules along the field lines emanating from the MNP core to pass very closely to the MNP core surface. In solid silica shell nanoparticles, water cannot diffuse along the field lines as close to the MNP core and so they have largely suppressed MRI capabilities. The presence of the mesoporous structure also allows for bi-modal imaging capabilities. In addition to MRI, it is possible to load the mesopores with fluorescent dye, allowing for bi-modal imaging in biological specimens.

To gain further control over the release kinetics of dyes or therapeutics loaded into the mesopores of MNP-MSN nanoparticles, poly (N-isopropylacrylamide) (PNIPAM) is a commonly used thermoresponsive polymer, which allows for the temperature-gated release of molecules loaded within the mesoporous structure.[120] This is often done by an *in situ* polymerization of the polymer with the particle surface to ensure covalent conjugation of the nanoparticle to the polymer for system stability.[121] Furthermore, since the volume phase-transition temperature (VPTT) of PNIPAM, which allows it go from a water-swollen state, to a hydrophobic, globular state when heated above its lower critical solution temperature (LCST) in water, is 32-33 $^\circ$C. As a result, PNIPAM will be present in the shrunken state at physiological temperatures (37 $^\circ$C)[122], preventing it from carrying large amounts of dye or therapeutic. Moreover, it will prevent it from shrinking in

response to the solution temperature being elevated above physiological temperature, abrogating its ability to release drug in response to magnetic hyperthermia. To address this, Shoukuan Fu and co-workers grafted a thermosensitive co-polymer, poly (N-isopropylacrylamide-co-N-hydroxymethyl acrylamide) [P(NIPAM-co-NHMA)] is grafted the MNP@MSN core-shell nanoparticles.[123] This co-polymer shifts the VPTT to 38-44 ^{O}C, allowing for its use in physiological systems. They loaded Zn(II) phthalocyanine tetrasulfonic acid ($ZnPcS_4$), a well-known photodynamic therapy sensitizer, into the pores of the drug to assess its ability to release the cargo in response to magnetic hyperthermia. The authors found that they could release the drug in a burst release kinetic profile over 24 hours at 39 ^{O}C, suggesting potential targeted applications in tumor treatments. (PNIPAAM NHMC coating of mnp@ms for thermoresponsive shell). Many other such example systems exist, even those utilizing designs not centered around polymers. For example, Jeffrey I. Zink, et al., coated MNP-MSN nanoparticles with pseudorotoaxanes.[124] In this design, under an alternating magnetic field to initiate hyperthermia, the psuedorotaxane-based molecular machines would disassemble. As such, they no longer occluded access of the drug in the pores from diffusing into solution. This was shown to be an effective way to initiate targeted release of doxorubicin to kill MDA-MB-231 breast cancer cells.

UCNP-MSN core-shell nanoparticles have also been utilized for similar applications such as controlled drug release and bimodal imaging in response to NIR excitations, rather than magnetic hyperthermia. In one such example, Jianlin Shi and coworkers demonstrated that $NaYF_4$:Tm/Yb/Gd UCNPs could be sued for bimodal upconversion fluorescence and MRI-based imaging *in vivo*.[99] Gd3+ chelates are a well-known T1 MRI contrast-enhancing agent, and allow the UCNPs to give a strong T1 signal in response to a 3.0T clinical MRI instrument. Then, in response to 980 nm NIR

excitation, the Yb/Tm co-doped system produces fluorescence located at 800 nm. It is also possible to use dual-mode fluorescence imaging, as has been demonstrated by several groups.[125,126] This will be discussed more in the next section (1.2.5).

Our group has also used UCNP@MSN core-shell nanoparticles to make stimuli-responsive drug delivery vehicles. In this work, we developed polypeptide-wrapped mesoporous silica coated multicolor UCNPs.[127] The exterior surface of the UCNP@MSN nanoparticles was functionalized with a zinc-dipicoylamine analogue (TDPA-Zn^{2+}), while the interior mesopores were loaded with small-molecule therapeutics, such as chemotherapeutics. The drugs remain entrapped within the mesopores due to steric occlusion from the branched polypeptide wrapped around the UCNP-MSN nanoparticles. Furthermore, the Aspartate moieties present in the polypeptide formed complexes with the TDPA-Zn^{2+}, leading to luminescence resonance energy transfer (LRET) from the UCNPs to the entrapped drugs due to the fact that they typically possess some UV-Visible absorptions. This resulted in the quenching of UCNP emission in the UV-Visible range, while retaining its intense NIR emissions. However, upon addition of ATP, a competitive displacement reaction between ATP and the surface-wrapped polypeptide took place, removing the polymer from the UCNP-MSN nanoparticles, and allowing for drug release. Furthermore, monitoring in the ratiometric LRET changes allows for real-time tracking of drug release. These types of on demand release systems, further coupled with the ability to track and monitor or engage in bimodal *in vivo* imaging have great potential in cancer and stem cell therapies, cell

control, and imaging. (real-time monitoring of atp-responsive durg release using mesoporous silica coated multicolor upconversion nanoparticles)

1.2.3 Heterogeneous UCNP-UCNP Core-Shell Nanoparticles

Near-infrared (NIR)-to-visible upconversion nanoparticles (UCNPs) are a powerful class of tools which have the potential to revolutionize biomedical and photonic applications. These include but are not limited to the development of solar cells which can utilize the intense NIR portion of the solar spectrum[128-131], optical biomedical probes[100,101,132], biosensing[133,134], next-generation phototriggers and photoswitch modulators for advanced drug delivery and therapies[135-137], and surface manipulation/display technology[125,126,138]. However, the most efficient upconversion material to date, NaYF4:Yb,Ln (where Ln=Lanthanide), suffers from relatively poor upconversion efficiencies of only a few percent.[90,91] This is due to the non-linear characteristics of the process, as well as the low absorption cross-section of Yb, which sensitizes the UCNPs to the absorption of 980 nm NIR light, and the parity forbidden nature of the 4f-4f transitions of the lanthanides[139]. Because of this, UCNPs generally cannot harvest enough photons to produce their characteristic UV-Visible multiphoton emissions at relatively low excitation power densities. Furthermore, the surfaces of UCNP cores are exquisitely sensitive to luminescence quenching due to the coupling of vibrational modes from water and surface ligands to the luminescent centers.[140] As such, UCNPs require irradiation with relatively intense (W/cm^2) continuous (cw) lasers under biological settings. Although the UCNPs are stable under cw lasers due to their inorganic nature, many other materials are not, such as the organic materials that constitute a large portion of many devices as well as biological specimens. Furthermore, high power

980 nm excitation can significantly damage devices/biological specimens due to its large heating effect owing to the NIR absorption of water at 980 nm.[100]

To address this limitation, heterogeneous core-shell UCNP-UCNP nanoparticles were developed which consist of epitaxially grown shells of $NaYF_4$, where each shell contains a different dopant composition, or sometimes no dopant at all. This allows researchers to protect the core-shell UCNPs from quenching due to surface ligands and/or control the energy migration dynamics within the core-shell UCNPs.[93] Their synthesis follows the same procedure as that for core UCNPs, except at room temperature, after the initial heating at 150 ^{O}C to form the lanthanide-oleate complexes, the core UCNPs are added into the reaction. Then, the NaOH and NH4F mixture (NaF) are injected into the reaction, which proceeds as normal. This promotes the nucleation and growth on the surface of the core UCNPs, via epitaxial growth. Since the growth regime is epitaxial, it is more thermodynamically favorable for the $NaYF_4$ to nucleate and grow, via Ostwald Ripening, onto the core UCNPs than in bulk solution at high temperatures.[55]

One of the first utilizations of synthesizing heterogeneous UCNP@UCNP core-shell structures to manage energy migration was to coat core UCNPs with $NaYF_4$ to prevent surface-related luminescence quenching.[140] As previously mentioned, water and surface ligands bound to the exterior of UCNP crystals can vibrationally couple to the luminescent lanthanide ions on the interior of the particle. This work showed that a thin $NaYF_4$ layer, which is photon inert without any lanthanide doping, can serve to de-couple the surface bound ligands and/or water from the interior luminescent lanthanide atoms. This greatly enhanced and retained the emissions of the UCNP core-shell crystals and also served as a platform to begin modulating the emission spectra of the UCNPs. The inert shell minimizes surface relating quenching, and as such, can better promote higher

order photon transitions (transitions involving a higher number of photons). This is because the lower order transitions are energetically closer to the vibrational stretches of the surface ligands and/or adsorbed water.[141] As such, there will be a higher ratio of shorter wavelength peaks vs longer wavelength peaks. The exact ratio will depend on the size of the core-shell UCNP, its exact composition, and the power density of excitation.[8,102] Larger UCNPs will promote higher order photon transitions due to the relatively lower surface rea to volume ratio. However, upon coating with an inert shell size plays a less important role as the surface has been vibrationally decoupled from the luminescent lanthanides in the core-shell UCNPs. (ucnp surface quenching)

Another example of utilizing core-shell architectures in UCNPs involves the use of Nd^{3+} as a sensitizer in $NaYF_4$:Yb/Nd/Ln based UCNPs.[142] Nd^{3+} imbues the UCNPs with 808 nm absorption. It then transfers the excited state energy to Yb^{3+}, which then, as discussed in section 1.15, is transferred to the luminescent lanthanides, resulting in upconversion fluorescence. However, Nd^{3+} has a very large quenching effect, and as such, must be doped at extremely low concentrations, typically below 1 mole percent. In order to address this, C.-H. Yan and coworkers coated the triply doped Nd/Yb/Ln UCNP cores with a NaYF4:Nd(20%) shell.[142] This resulted in luminescence 7 times more intense than the same cores coated with an inert $NaYF_4$ shell, showing that the affect was not due to the mitigation of surface quenching from the luminescent lanthanides.(8 from transition layer) To take this idea one step further, J. Yao and coworkers developed a multi-shell UCNP structure which allowed them to load the outer shell with $NaNdF_4$.[143] The prevent extreme quenching between the $NaNdF_4$ shell and the core interface, they used a transition layer, doped with Yb^{3+} to carry the excitation energy from the Nd^{3+} doped sensitizing shell to the luminescent core. This clearly shows the utility of heterogeneous core-shell UCNP structures, which allow researchers to modulate the

energy migration through the UCNP, to produce characteristic emission and excitation profiles.

A recent interesting example of this ability to control energy migration through core-shell UCNPs was shown to occur in response to excitation pulse width modulation.[144] In this work, X. Liu and coworkers constructed a UCNP composed of a NaYF4:Nd/Yb core. This provided the ability to excited at 808 nm. Then, the first shell was epitaxially grown of the core. This first shell was doped with Yb^{3+} and Tm^{3+}, imbuing the particle with both 980 nm excitation and blue emission. The following shell was an inert NaYF4 shell, to prevent energy migration between the blue emitting core-shell structure just described. The next layer contained Yb^{3+}, Ho^{3+}, and Ce^{3+}. Finally, an inert shell was grown on top of this to preserve the emissions. This last luminescent layer triply doped with Yb^{3+}, Ho^{3+}, and Ce^{3+} allows for the core-multishell UCNPs to emit both red and green, depending on the excitation pulse width at 980 nm. This is due to the ability of Ce^{3+} to act as an energy migration modulator, depending on the excitation pulse width. In this shell layer, a short pulse width (≥ 200-500 us) will promote non-steady state energy migration dynamics, such that the kinetically populated energy levels of Ho^{3+}, $^5F_4$, and $^5S_2$, are populated and emit green light at 541 nm. However, during the application of a long pulse width (≥ 1-5 ms), steady-state energy migration dynamics take over, allowing for the eventual energy transfer from the $^5I_6$ state of Yb^{3+}, through Ce cross-relaxation, to the $^5I_7$ state of Ho^{3+}. This state is then continually pumped by the long pulse width 980 nm excitation light, promoting the red upconversion emissions at 646 nm from the $^5F_5$ state of Ho^{3+}. This gives these multi-shell UCNPs the capability to produce RGB emissions in response to excitation wavelength and pulse-width modulation. Furthermore, they were able to show the ability to tune the multi-shell UCNPs, using their RBG emissive profiles, to show their ability to tune the UCNPs color, by mixing the different RGB emissions in various ratios. Impressively, combined with the

narrow emission bandwidths of the lanthanides, allowing access to color spaces much wider than currently accessible with conventional high-definition televisions. Demonstrations such as these show how powerful the use of core-shell UCNP architectures to manage energy migration can be. They offer researchers the ability to completely define the excitation and emission profiles within the lanthanides for their application at hand. This has important implications in biological imaging and sensing.

1.3 The Characterization of Nanoparticles for Biological Applications

Careful characterization of nanoparticles for biological applications is an important part of getting the material ready for bioconjugation and cell delivery. This confirms that you have the intended material, and know how many biomolecules are present on the surface, etc., so one can discern the effects of the nanoparticle construct on the biological system. One of the first things to check is that the particles are of the appropriate size and morphology. If the particles are too big or too small, they may not effectively serve the application at hand by changing, for example, either their magnetic or luminescent properties. The easiest way to get an estimate of the size is Dynamic Light Scattering (DLS). This gives a size and distribution profile, typically by number so it is representative of the nanoparticle population, to check and see if the synthesized material is the right size for the application.

To further check the size, morphology, and any aggregation in the particles, Transmission Electron Microscopy (TEM) is often the next step. TEM is a powerful tool which allows researchers to check the particle size and morphology by actual visualization of the nanoparticles. If the nanoparticles will not form nicely packed layers, and are of regular shape, the particles will be aggregated to some extent. This should also show on the DLS profile, as a small peak, typically from several hundred nanometers to several microns in size depending on the sample and the state of aggregation. However, High Resolution TEM (HRTEM) can prove to be even more

powerful as it allows visualization of the crystal facets and the ability to measure the spacing between the atomic planes in the crystals. This allows researchers to characterize the phase of their nanoparticle, which can be particularly important for maintaining good magnetic and luminescent characteristics, as previously discussed.

To verify that the phase of the nanoparticles is indicative of the entire sample, it is often a good idea to couple the nanoanalysis with bulk analysis. In this case, powder X-Ray diffraction (PXRD) is a convenient and simple method to determine the phase of nanoparticle powder. This ensures that the phase of the entire sample is indicative of the nanoparticles analyzed during lattice imaging under HRTEM. This trend of complementary nano and bulk analysis can be furthered through the use of nano energy dispersive X-Ray (EDX) and nano electron energy loss spectroscopy (EELS) with bulk compositional characterization methods, such as inductively-coupled plasma optical emission spectroscopy (ICP-OES). EDX or EELS analysis, when coupled with scanning TEM (STEM) can provide composition information with resolution comparable to or smaller than individual nanoparticles. This offers the ability to characterize the elemental distribution within single nanoparticles to correlate the relationship between the composition of individual nanoparticles and their physicochemical properties. These techniques can even provide the means to study compositional changes from core nanoparticles to individual shell layers of a few nm in thickness. To confirm that these compositional profiles are indicative of the entire bulk sample, ICP-OES can be performed to obtain atomic compositional information from a bulk nanoparticle sample. The correlation between bulk composition and nanocomposition is an important facet of core-shell nanomaterials characterization.

Once the inorganic portion of the nanoparticles has been confirmed, it is equally as important to understand the nanoparticle surface before engaging in bioconjugation. One way to initially characterize particles in aqueous conditions, typically after ligand

exchanges, along with DLS, is to measure the particles zeta potential. This is typically done using a Zetasizer machine, which is also how DLS is performed. Zeta potential measurements give a measure of the charge associated with the particle surface. If, for example, core-MSN shell nanoparticles are grafted with APTES to yield a surface covered in primary amines, the zeta potential would change from negative (associated with the silica oxide surface) to positive from the primary amines. This allows researchers to know the number of ligands associated with the particles surface and the use of stoichiometric amounts of reagents and biomolecules during functionalization and bioconjugation. In order to quantify the number of ligands on the particle surface, titration is often used. For example, with primary amines, Snyders Test is typically performed to quantify the number of primary amines. Any functional ligand can be titrated by careful choice of the appropriate indicator and pH range to work in. In order to quantify the surface area of the sample, so that researchers can estimate the number of ligands per particle, yielding well characterized surfaces, N_2 gas adsorption isotherms can be used to approximate the surface area associated with a particular mass of sample. This can be of particular importance when one needs to understand the number of proteins or biomolecules associated with a single nanoparticle surface to ascertain their effects in cells.

The last important thing to characterize when doing surface and bioconjugation chemistry is to verify that the bonds are indeed being formed from various coupling reactions. In most cases, NMR is a powerful and simple tool to characterize the creation of bonds by looking for unique signals associated with the bond type. Often, amides, disulfides, and N-succinimide containing ligands are formed, making this a simple way to characterize the surface. Unfortunately, this is not the case for magnetic materials as their field lines make it difficult to get a lock on NMR, and preventing the collection of accurate spectra. To get around this, the simplest and most efficient method is the use

of FTIR. This allows for the visualization of vibrational modes from the newly formed ligand and biomolecule bonds connecting them to the particle surface.

In the end, it is important to track the construction of the nanoparticle platform from beginning to end. Initially, it is pertinent to check the size, size distribution, and morphology of the inorganic particles. Likewise, it is equally important to verify that the material is the desired phase, yielding the desired material properties. Then, upon initiation of surface functionalization and bioconjugation, it is imperative to track the creation of new bonds and to titrate and characterize the number of bonds and biomolecules associated with the particle surfaces. Only then can we truly know how the material will interact with and affect the biological systems under study.

1.4 Overview of Dissertation

Inorganic heterogeneous core-shell nanoparticles are an extremely interesting and diverse class of materials. They allow researchers to combine and modify the materials properties and functionalities from multiple platforms into a single, multifunctional nanoparticle. This class of nanoparticles has shown its great potential in advancing technological, and biomedical applications. More interestingly, they allow new scientific discoveries and findings which would have been unachievable using two distinct and separate materials. From new magnetic properties, enhanced and controlled luminescence, and the ability to couple these properties together from different materials has had and will continue to have a profound impact on the way nanomaterials are used in biomedical applications. As more control over the system and material are required, novel core-shell structures will be designed, synthesized, and utilized to offer researchers an even greater degree of control. This will continue to push the boundaries in biomedical applications and technologies.

In my attempt to do this, in the first two-thirds of my thesis, I designed and developed magnetic core-shell nanomaterials for cancer therapies. In the first third of the

dissertation the magnetic cores are combined with a gold shell to enhance the efficacy of an anti-cancer peptide, imbue it with targeting capabilities, and act In synergism to enhance cell death through the use of magnetic hyperthermia.

In the second third of my thesis, I design and synthesis a magnetic core mesoporous silica shell nanoparticle to deliver a heat inducible plasmid encoding a therapeutic anti-cancer protein, TRAIL. Furthermore, the use of the mesoporous silica shell, due to its low density, allows for the maintinence of strong magnetic properties in the MNP core. This allows us to initiate magnetic hyperthermia at low particle concentrations, enhancing cellular viability. Through mild magnetic hyperthermia, we were able to activate the expression of therapeutic anti-cancer TRAIL protein and induce significant cancer cell death.

In the last third of this thesis, I design and synthesize a novel heterogeneous core-shell structured UCNP, in order to mange energy migration within the particle and enhance its upconversion efficiency significantly at low power excitations. This mitigated the heating effect of 980 nm NIR excitation. Furthermore, we designed a simple UCNP-FRET based biosensor to demonstrate the utility of our novel structured UCNPs. Through them, we were able to sense at three orders of magnitude lower concentrations (pM) than similarly design UCNP FRET-based biosensors. Overall, this thesis demonstrates three heterogeneous inorganic core-shell nanoparticles for cancer therapy and biosensing.

Chapter 2

2.1 Core—Shell Nanoparticles-Based Peptide Therapeutics and Combined

Hyperthermia for Enhanced Cancer Cell Apoptosis

The text and images used in this chapter have been previously published in ACS Nano

as an original manuscript (Shah, B.P; Pasquale, N; De, G; Tan, T.; Ma, J; Lee, K.-B.

ACS Nano 8 (9) (2014) 9379-9387.)

2.1.1 Introduction

Despite the progress made towards cancer therapy, there is a lack of clinical

advances and approaches available to administer the drugs to the patients.[145,146] There

remains challenges in delivering the therapeutic moieties to the tumor site as well as

increasing drug efficiency with minimal side effects.[147] To this end, developing a

nanoparticle based platform that can (i) allow access of the therapeutic drugs to the

tumor sites by penetrating physiological barriers,[148,149] (ii) enhance targeted drug

delivery,[150] and (iii) working synergistically with other treatments to enhance their

chemotherapeutic effects[145,151] is vital to successfully overcome the aforementioned

challenges.

Despite the efficacy of tumor and cellular targeting of chemotherapeutics,[148,150] there

has been a growth of research aimed towards targeting subcellular organelles such as

the mitochondria.[152,153] The mitochondria plays a critical role in cellular apoptosis and its

damage lead to irreversible cell death, which can be employed for cancer therapy.[154,155]

Various types of Small molecules that target the mitochondria, such as peptides and

RNA-interference (RNAi) molecules, show therapeutic effects by promoting

apoptosis.[156-159] Of these small molecules, peptide delivery is a promising approach to

initiate apoptosis since they have high affinity interaction with mitochondria and are readily delivered to the cells, such as amphipathic tail-anchoring peptide (ATAP).[160]

ATAP, a novel mitochondrial targeting peptide, has been demonstrated to induce irreversible mitochondria-dependent apoptosis by selectively targeting the mitochondria and promoting the release of cytochrome c which leads to apoptosis.[161,162] One the main advantages of ATAP is not only its ability to induce apoptosis, but it can do so with the need of pro-apoptotic proteins or the influence of by concertation of anti-apoptotic proteins, which can be mutated in the neoplasm. Despite the novelty of ATAP and it high potential for cancer therapy, it is hindered for clinical use due to its poor solubility and
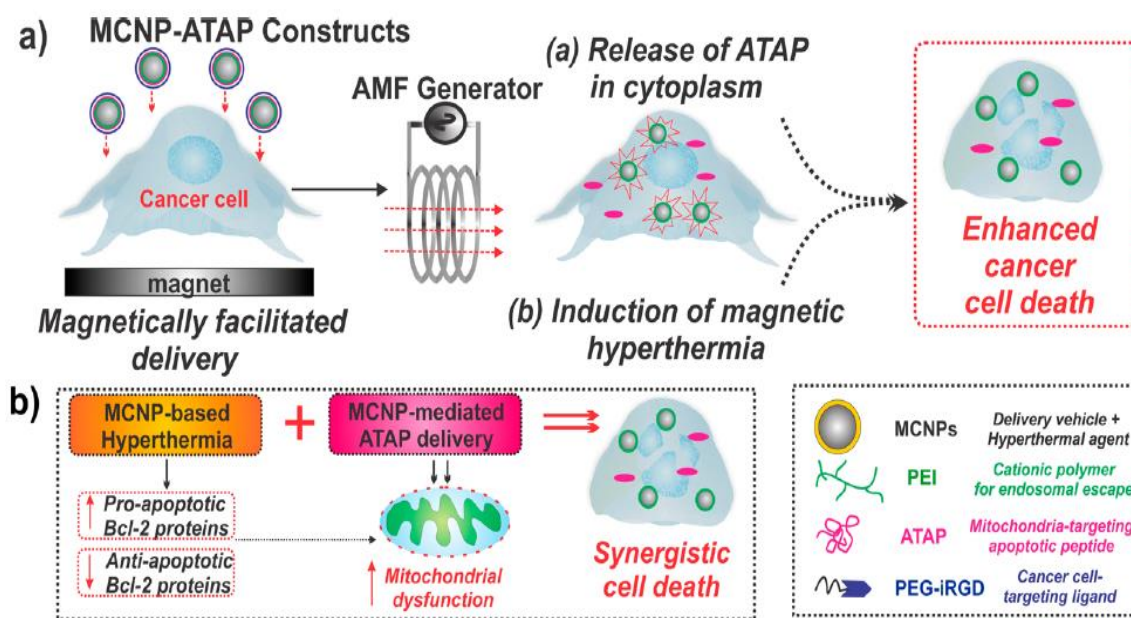
Figure 2.1. A) Schematic diagram portraying the delivery of MCNP-ATAP to brain and breast cancer cells via magnetically facilitated targeted delivery. The release of ATAP in the cytoplasm along with the induction of hyperthermia in the presence of an alternating magnetic field (AMF) allows for synergistic cell apoptosis. B) MCNP-based hyperthermia leads to inactivation of anti-apoptotic bcl-2 proteins along with an increase in pro-apoptotic bcl-2 proteins. Meanwhile, MCNP-ATAP allows for permeabilization of the outer mitochondrial membrane, inducing mitochondrial dysfunction. The combined effects of hyperthermia and ATAP synergistically enhance cancer cell death. Key: MCNP, magnetic core–shell nanoparticles; PEI, polyethylenimine; ATAP, amphipathic tail-anchoring peptide; PEG, polyethylene glycol; iRGD, internalizing RGD.

stability in physiological conditions due to its amphipathic structure and its lack of tumor-targeting capabilities.[160,163]

To overcome the aforementioned challenges, nanoparticle-based platforms have been shown to improve delivery and drug efficacy. Their unique physiochemical properties and their ability to incorporate additional properties, such as hyperthermia, photochemical therapy and imaging allow for enhanced drug delivery and alternate therapeutic effects.[164,165] The properties are dependent on the composition, for example, magnetic nanoparticles (MNP), which are composed of highly magnetic zinc doped iron oxide, afford localized hyperthermia (an increase in temperature) in the presence of an alternating magnetic field.[166,167] Localized hyperthermia has been demonstrated to enhance therapies such as sensitizing tumors to chemotherapy and radiation therapy[168,169] as well as increase the pro-apoptotic abilities of peptides by directly inhibiting anti-apoptotic Bcl-2 family members[170] and increasing the permeabilization of the mitochondrial membrane.[171-173] Moreover, MNPs can be further modified with a gold shell, which enables plasmonic properties for biological applications including imaging cell targeting and chemotherapy.[174]

Herein we describe the development of a magnetic core—shell nanoparticle (MCNP) based platform for targeted delivery of ATAP as well as localized hyperthermia for enhanced cancer cell death (Fig. 2.1). As a proof-of-concept demonstration, we chose malignant brain cancer cells, glioblastoma multiforme (U87vIII), and metastatic breast cancer cell (MDA-MB-231), which contain subpopulation of cancer stem cell to test the efficiency of MCNP-ATAP.[175] The gold shell allowed for facile bioconjugation of both ATAp and tumor targeting peptide, iRGD,[150] while the magnetic core allowed for a magnetically facilitated delivery of the MCNP-ATAP platform for enhanced cellular uptake.[174,176,177] Additionally the MCNP enabled local hyperthermia[178] combined with

ATAP will synergistically enhance cancer cell apoptosis leading to significant improvements in cancer therapy.

2.1.2 Results and discussion

Synthesis and Characterization of MCNP-ATAP Conjugates
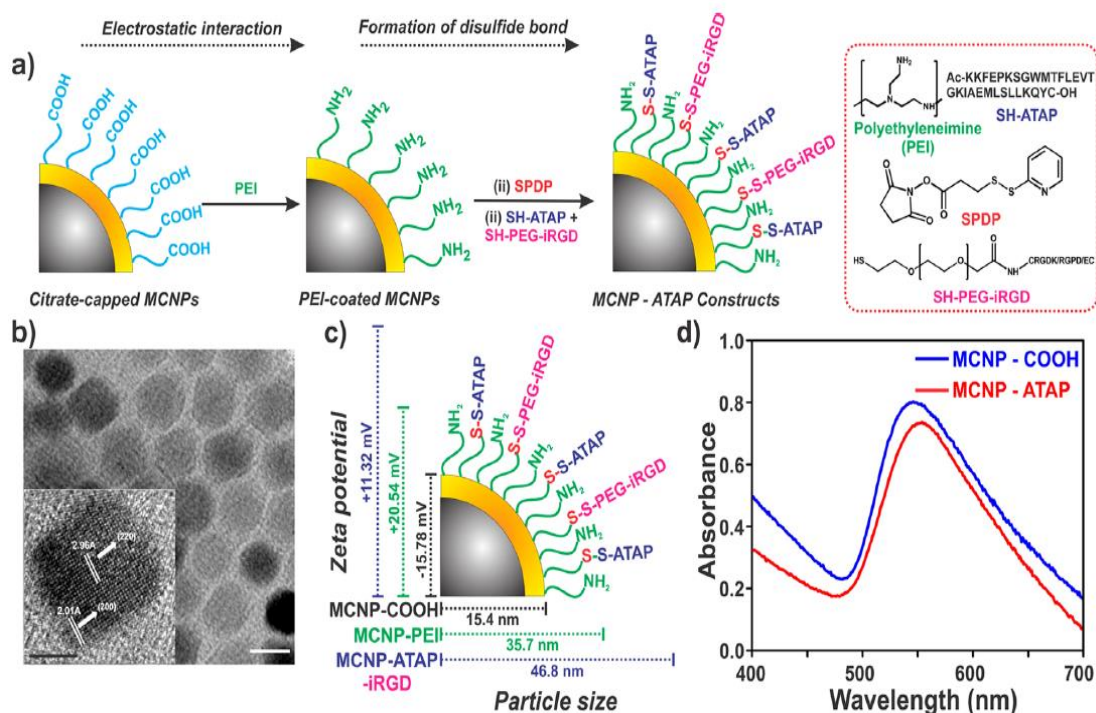
Figure 2.2 A) Conjugation of ATAP and iRGD (targeting ligand) to MCNPs. Key: PEI, polyethylenimine; ATAP, amphipathic tai lanchoring peptide; SPDP, N-succinimidyl 3-(2-pyridyldithio)propionate; PEG, polyethylene glycol; iRGD, internalizingRGD. B) TEM image of MCNP-ATAP. High-resolution TEM image of MCNPs with crystalline Fe and Au lattices. C) Hydrodynamic and Zeta potential measurements of each step of the construction of the

To construct MCNP-ATAP, the MNP cores (Fig. 2.2A) were first synthesized by making slight modifications to a previously reported protocol.[179] The gold shell was deposited onto the MNP cores using a slight modification of a previously reported protocol[174] to synthesize citrate-capped MCNPs with a hydrodynamic diameter of 15.4nm (Fig. 2.2B). To provide the particles with a positive charge, The MCNPs were

coated with a branched polyethlenimine (PEI, MW = 10 kDa) via electrostatic interactions. The PEI will also act a proton sponge and induce endosomolysis with the cytoplasm[180] to shield the MCNP-ATAP platform for the highly acidic endosomal platform.

The amine-terminated MCNPs were then conjugated to thiol-terminated ATAP moieties via a heterobifunctional cross-linker, N-succinimidyl-3-(2-pyridyldithio) propionate (SPDP), to form the MCNP-ATAP construct. Furthermore, using the same SPDP linker, thiol-PEG-iRGD were also conjugated to the MCNPs to allow for targeted delivery of the platform to the cancer cells as well as increased aqueous solubility.[181] The diameter and zeta potential of the final MCNP-ATAP construct was found to be 46.8 ± 2.3 nm and positively charged with a charge of + 15.78 mV using dynamic light scattering (Fig. 2.2C). The positive charge allowed for increase in cellular uptake. UV-visible spectroscopy confirmed the presence if ATAP moieties on the surface of the MCNPs by showing a slight red shift. To calculate the amount of ATAP present on the surface of the MCNPs, the concertation of unconjugated ATAP in the supernatant was calculated using UV—Vis spectroscopy. It was found that 10nM ATAP was conjugated to 1 μg/mL of MCNPs, which is approximately 500 ATAP per MCNP and 50% loading amount of ATAP.

The cell viability of either U87vIII or MDA-MB-231 cells were not affected by the MCNP concentrations within a range of 5-50 μg/mL, thus concluding that the particles

are biocompatible. Additionally the biocompatibility of the MCNPs coated with PEI were

tested and were found to also not induce cytotoxic effects on the cells.

Integrin-Mediated Targeted Delivery of MCNP-ATAP Constructs to Cancer Cells.
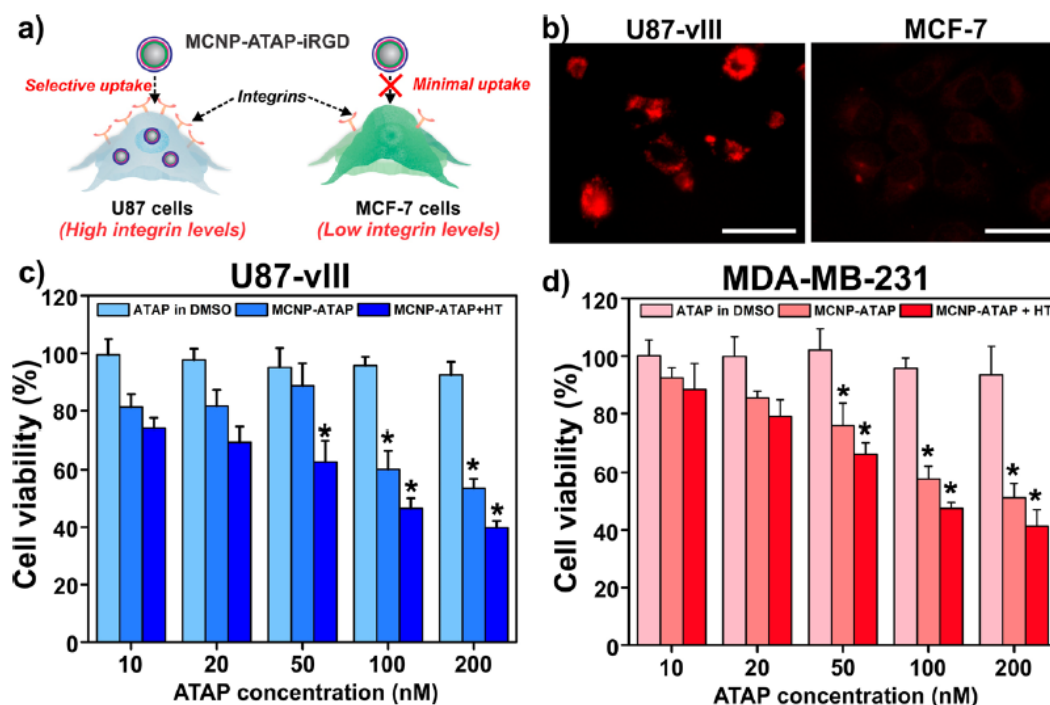
Figure 2.3 A) MCNP-ATAP modified with internalized RGD (iRGD) were delivered to U87 cells as opposed to MCF-7 cells, due to high levels of integrins expressed on the membrane of U87 cells, which readily interact with iRGD. B) Epifluorescent images comparing the targeted delivery of MCNP-ATAP modified with iRGD to U87 cells and MCF-7 cells. C) Cell viability of ATAP, MCNP-ATAP and MCNP-ATAP in the presence of hyperthermia treated U87vIII cells 48 h after initial transfection. D) Cell viability of ATAP, MCNP-ATAP and MCNP-ATAP in the presence of hyperthermia treated MDA-MB-231 cells 48 h after initial

Once the synthesis of the MCNP-ATAP platform was confirmed and characterized,

their targeted delivery and apoptotic efficacy in brain cancer cells (U87vIII)

overexpressing the mutant epidermal growth factor receptor vIII (EGFRvIII) were

tested.[182] The overexpression of EGFRvIII has been implicated in enhancing the

tumorigenicity and resistance to radiation and chemotherapy in GBM.[183] As previously

mentioned, since ATAP lacks tumor targeting capabilities, the MCNPs were conjugated with iRGD, which has been reported to home to the Rvβ3 integrin surface receptors present in glioblastoma and other cancer cells (Fig. 2.3A).[184] To visualize the MCNPs in the cells using a fluorescence microscope, the MCNPs were also conjugated with a fluorophore, Alexa Fluor 594.

The iRGD-conjugated MCNPs were then incubated withU87vIII and MCF-7 (breast cancer) cells, which have low integrin expression.[185] The cells were then washed with PBS (3 times) to remove any excess MCNPs and imaged using fluorescence microscopy. U87vIII cells, having higher integrin levels show significantly higher uptake of the iRGD conjugated MCNPs as compared to MCF-7 cells, which have low levels of integrins (Fig. 2.3B). Based on the results, the MCNP-ATAP platform has efficient targeting capabilities by simply conjugating targeting ligands, all without making any structural modifications to ATAP, which can compromise its efficacy.

Apoptotic Efficacy of MCNP-ATAP Constructs in Cancer Cells.

Next, we tested the apoptotic efficiency of the MCNP-ATAP platform in both glioblastoma (U87vIII) and breast cancer (MDA-MB-231) cells. We first tested the effect of varying the concentration of unconjugated ATAP in DMSO on the viability of the cells using the MTS assay, which showed a negligible effect on the viability of both cell lines, even at concentrations as high as 200 nM (Fig. 2.3C). We then tested the chemotherapeutic effect of the MCNP-ATAP platform delivered to the both cell lines via magnetically facilitated delivery.[176,177] Upon optimization of the magnetic field exposure, we found that 30 min was the optimal exposure time, resulting in a significantly higher uptake of the MCNP-ATAP platform.

To test the apoptosis-inducing ability of MCNP-ATAP platforms in both cell lines, we delivered varying concentration of the particles to cells using magnetically facilitated delivery and determined the cell viability using a 48 h post-transfection MTS assay.

Compared to unconjugated ATAP, the MNCP-ATAP platform resulted in a significant increase in cell death for both cell lines. The results thus far indicate that the potency and efficacy of ATAP is significantly enhanced when conjugated to MCNPs, which can possibly be attributed to its increase in aqueous solubility.

We also tested whether the release of ATAP from the MCNPs would allow for a maximal effect on cell viability. We compared the effects of cell viability of brain cancer cells using the previously described MCNP-ATAP platform in two forms one with a i) cleavable disulfide bond and the other with a ii) noncleavable amide bond. The noncleavable bond showed a modest decrease in the cell viability compared to the cleavable construct. These results indicate that even though we see an overall increase in chemotherapeutic effects with the conjugation of ATAP to the MCNPs, a release mechanism of ATAP from the MCNPs is essential to achieve maximal apoptotic effect.

Effect of MCNP-Mediated Combined ATAP Delivery and Hyperthermia in Cancer Cells.

Previously we mentioned that MCNPS could induce localized hyperthermia in the presence of an alternating magnetic field, which can act synergistically with ATAP to increase the overall apoptotic effect (Fig. 2.1B).[170,171] To evaluate this we initially tested the combination of MCNP-ATAP and water-bath hyperthermia. The MCNP-ATAP treated cells were exposed to 45 min of water bath hyperthermia at 43 $^{\circ}$C and the percent viability was quantified as before. This combined treatment did not significantly increase cancer cell apoptosis. We then tested the MCNP-ATAP treated cells with MCNP induced hyperthermia. Once the duration of exposing cells transfected with MCNP with hyperthermia was optimized, it was found that 45 min of hyperthermia was optimal to induce further cell death (an additional ~20% based on MTS).

The U87vIII and MDA-MB-231 calls were then transfected with MCNP-ATAP constructs and exposed to hyperthermia 24 h post-transfection. The cell viability

following the combined therapy was determined 48 h post-transfection using an MTS cell

viability assay. We were able to demonstrate that that the combined therapy of MCNP-

ATAP ([ATAP] = 200 nM) and hyperthermia (45 min) caused significant cell death, as
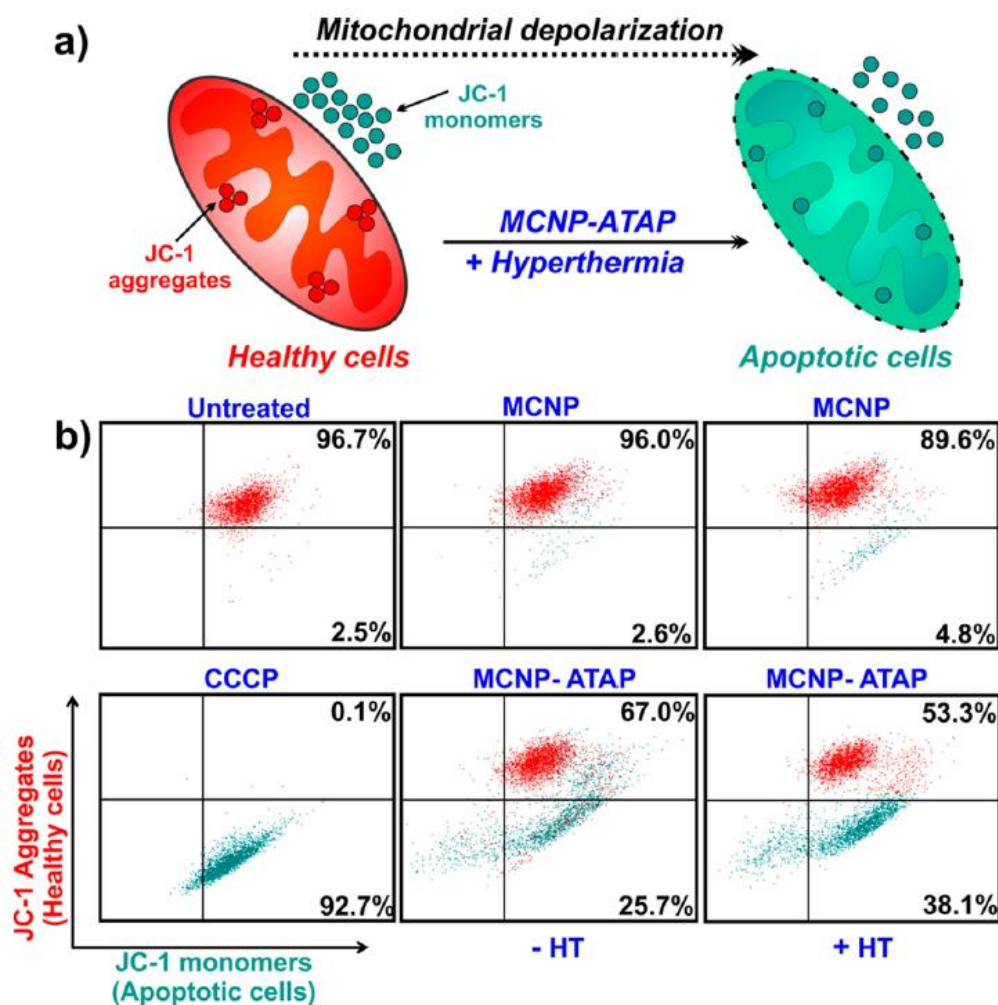
Figure 2.4 A) Schematic diagram portraying the JC-1 aggregates in healthy cells before treatment with MCNP-ATAP and JC-1 monomers in apoptotic cells after treatment with MCNP-ATAP. Key: red, healthy cells; green, apoptotic cells). B) Flow-cytometry-based JC-1 assay to measure the mitochondrial depolarization induced by MCNP-ATAP. Key and amounts: CCCP, carbonyl cyanide 3-chlorophenylhydrazone (positive control); MCNP, 20 μg/mL;ATAP, 100 nM; hyperthermia (HT), 45 min.

compared to either treatment alone. The results are indicate that MCNP-mediated

hyperthermia significantly enhances ATAP-mediated cancer cell death.

Effect of MCNP-ATAP Constructs on Mitochondrial Depolarization of Cancer Cells.

The next step was to confirm that the MCNP-ATAP-mediated cancer cell death

was indeed caused by mitochondrial dysfunction. This was achieved by investigating the

mitochondrial membrane potential ($\Delta\Psi$m) using a flow-cytometry-based JC-1 assay.[155]

Mitochondrial dysfunction leads to mitochondrial depolarization which ultimately results

in apoptosis (Fig. 2.4A). JC-1 is a lipophilic, cationic dye, which selectively translocates

to the mitochondria and under goes a color change as a function of the mitochondrial

membrane potential ($\Delta\Psi$m).[186] In healthy cells with high $\Delta\Psi$m, JC-1 spontaneously

forms intense red colored complexes known as J-aggregates, whereas in apoptotic cells

with low $\Delta\Psi$m, JC-1 remains in the green monomeric form.[187]

Upon treatment of cells with MCNPs alone, there is no obvious change in the

mitochondrial membrane of U87vIII, with 96.0% formation of red J-aggregates and 2.6%

formation of green JC-1 monomers. On the other hand, when the U87VIII cells were

treated with MCNP-ATAP, there was a decrease in red fluorescence, of about 67.0%

and a significant increase in JC-1 monomer in the cytoplasm of about 25.7%. This gave

an increase in green fluorescence which suggests an increase in mitochondrial

polarization and hence apoptosis. Furthermore, we quantified the ATAP-induced

mitochondria-dependent apoptosis of U87vIII cell by conducting a flow-cytometry-based

annexin V-FITC/PI assay. Combined treatment of MCNP-mediated ATAP and

hyperthermia (MCNP-ATAP+HT) showed the highest percentage of apoptotic cells

(38.3%), as compared to the individual MCNP-ATAP only and MCNP-induced hyperthermia treatments.

Preliminary in Vivo Testing of ATAP-iRGD Constructs.

Once the potency of MCNP-ATAP was established, we went on to test its potency using an in vivo mouse xenograft model. To test immune responses in the mouse model we systemically injected the MCNP-ATAP-iRGD platform in mice and found that no obvious immunogenicity was observed when tested over a period of 3 weeks. Additionally, we tested the tumor targeting capability of ATAP-iRGD constructs in an esophageal cancer (KYSE)[188] xenograft model, which showed that that ATAP-iRGD had similar tumor suppression effects to those of BH3-iRGD peptide in equal molar concentration. This indicated that ATAP-iRGD suppresses esophageal tumor growth with limited off-target toxicity in the mouse model. Compared to ATAP-iRGD which had an IC_{50} of 4-5 µM, MCNP-ATAP had a significantly improved IC_{50} from µM range to the 50 nM range in the MTT assay. These preliminary in vivo experiments strongly suggest the potential of MCNPs to enhance the delivery and efficacy if ATAP in tumors.

2.1.3   Conclusion

In conclusion, the combination of the MCNP-based targeted delivery of ATAP along with the magnetic hyperthermia leads to a synergistic effect on mitochondrial dysfunction and results in cancer cell death. The conjugation of PEG and iRGD provided the solubility and targeted specificity that ATAP lacked on its own. Our MCNPs provided us with a single platform that can both deliver ATAP and induce localized magnetic hyperthermia, therefore significantly enhancing the chemotherapeutic efficacy of ATAP. Furthermore, the materials composing the MCNPs allowed for noninvasive imaging, which can afford additional information for diagnosis and therapy. The magnetic nanoparticle core and the gold shell allow for MRI imaging and dark-field imaging respectively. This study establishes a proof-of-concept demonstration of the effects of

ATAP molecules conjugated to MCNPs on the cellular processes such as mitochondrial permeabilization and apoptosis. Further studies will evaluate the chemotherapeutic efficacy of the platform in xenograft models.

2.1.4   Material and Methods

Synthesis of Core-Shell Nanoparticle

The first step in constructing the MCNP platform is to synthesize the magnetic nanoparticle cores.[59] In a 100 mL three-neck round-bottom flask, 1 mmol of zinc chloride (ZnCl2), 2 mmol of iron(III) acetylacetonate (Fe(acac)$_3$, C15H21FeO$_6$), 6 mmol of oleic acid, 6 mmol of oleylamine, and 10 mmol of 1,2-hexadecanediol were mixed in 20 mL of trioctylamine under a high stir rate. The reaction mixture was heated to 200 ^{o}C for 2h and then to 300 ^{o}C for 1h. The reaction mixture was then cooled to room temperature and the magnetic nanoparticles were then purified (by repeated centrifugation and sonication) and precipitated in ethanol. The nanoparticles were then dried under vacuum overnight.

To coat the cores with gold,[179] 2.5 mg of the magnetic nanoparticle dispersed in chloroform were mixed with 10 mL of tri-n-octylamine and heated to evaporate the chloroform. The mixture was brought to room temperature to then add 15 µL of a 5mg of HAuCl$_4$ in 300 µL of ethyl acetate stock solution drop wise as well as 0.306 µL of 1-doddecanethiol. The reaction mixture was then heated to 150 ^{o}C for 4 h. After the 4 h of heating, the mixture was brought to room temperature and Au-coated particles were centrifuged, washed and magnetically decanted several times with chloroform to separate the core—shell nanoparticles from any pure gold nanoparticles that may have formed.

Thus far the MCNPs are hydrophobic and contain hydrophobic surface ligands. To render the particles water soluble, a ligand exchange reaction is performed.[189] The particles are suspended in minimal amount of chloroform and slowly added to 5 mL of a

1M TMAOH solution containing 0.06 g of trisodium citrate in a slightly acidic condition while sonicated on a probe sonicator for 30 min. The water dispersible particles were then purified several times by magnetic decantation.

Formation of MCNP-ATAP Platform

The next step in constructing the platform is to coat the MCNPs with PEI. The water soluble MCNPs described above were diluted to 0.1 mg/mL in Dulbecco's Phosphate Buffered Saline (DPBS). Excess 1 mg/mL 10 kDa branched PEI (Sigma-Aldrich) was added dropwise to the diluted particles and left to spin overnight. The PEI coated MCNPs were filtered and purified using a centrifugal unit (EMD Millipore, 10,000MW). The particles were then mixed with heterobifunctional linker and SPDP (0.1 mM) and incubated at room temperature for 4 - 6 h with continuous shaking. In parallel, the PEG-iRGD moieties were prepare by linking SH-PEG-COOH to iRGD-NH$_2$ using EDC coupling. Both the PEG-iRGD and the thiolated ATAP were added to the MCNP-PEI complex in various ratios and allowed to react overnight. The resulting MCNP-ATAP was purified using centrifugation and dispersed in sterile DPBS. The MCNP-PEI complex was also conjugated with Alexa-Fluor594-succinimide to allow for monitoring the MCNPS using fluorescence microscope.

Quantification of ATAP Conjugated to MCNPs Using UV-Visible Spectroscopy

The amount of ATAP present was calculated by measuring the absorbance of different concentrations of ATAP solutions at 280 nm using a UV—visible spectrometer (Cary US) and constructing a standard curve of ATAP in 8 M urea. To calculate the amount of ATAP conjugated per milligram of MCNP, the MCNP-ATAPs were incubated with 0.1 M DTT solution to cleave the disulfide bonds between the ATAP and MCNPs. The mixture was then centrifuged and the supernatant, which contained the ATAP, was

collected. Absorbance of the supernatant was measured at A280 nm and the equation used to calculate the concertation was:

mg ATAP per mL = (A280 × Dilution Factor × MW) / [(1 × 5560) + (1 + 1200)]

Particle Size and Zeta Potential Analysis

To determine the size and charge of the particles, dynamic light scattering and zeta potential analysis were performed using a Malvern instrument Zetasizer ZS-90 instrument (Southboro, MA, USA). Sequential measurements were collected and compared to verify the reproducibility of the procedures. Each step of the construct, MCNP, MCNP-PEI and MCNP-ATAP, were prepared and analyzed for DLS and zeta potential measurements in purified water (resistivity = 18.5 MΩ-cm). DLS measurements were performed at a 90° scattering angle at 25 °C. Zeta potential measurements were collected at 25 °C. For both tests, the Z-average potentials following three sequential measurements were collected and analyzed.

Cell Culture

U87-EGFRvIII cells were cultured in DMEM(Dulbecco's modified Eagle's medium) with high glucose(Invitrogen), 10% fetal bovine serum (FBS), 1% streptomycinpenicillin, 1%Glutamax (Invitrogen), and hygromycin B (30 µg/mL),while MDA-MB-231 and MCF-7 cells were cultured in DMEM/F-12with 10% FBS, 1% streptomycin–penicillin, and 1% Glutamax.

Magnetically Facilitated Delivery of MCNPs

2 × 105 cells in a volume of 500 µL were seeded into each well of a 24-well plate to reach 80–90% confluency at the time of transfection. After 24 h, varying amounts of MCNP-ATAP constructs were mixed with OptiMEM and added to each well. The Cell culture plates were then placed on a Nd–Fe–B magnetic plate (OZ Biosciences, France)

for 15 min and then placed back into the incubator. After 1–2 h of incubation, the media was replaced with growth medium.

Cytotoxicity Assay

A MTS assay was conducted in triplicates and averaged to determine the percentage of viable cells, following a protocol described by the manufacturers. The MTS data were represented as formazan absorbance at 490 nm after 48 h of initial transfection, using untreated cells with a 100% viability as a control.

Targeted Delivery

In 24-well plates, at a density of 5 × 104 cells per well, high-tumorigenic U87-EGFRvIII cells and low-tumorigenic MCF-7 cells were cultured. The Media used for MCF-7 cells was composed of DMEM/F-12 (with high glucose, Invitrogen), 10% FBS, 1% Glutamax, and 1% penicillin–streptomycin. For the delivery of iRGD-conjugated MCNPs, media was exchanged with serum-free DMEM media, and the cells were incubated with iRGD-MCNPs for 6–8 h. To obtain fluorescence images, serum-free media was replaced with regular media.

Magnetic Hyperthermia

As described above, the MCNP-ATAPs were delivered via exposure to a magnetic plate for 15 min. For magnetic hyperthermia, we used varying concentrations of 5–20 μg/mL of MCNP-ATAPs. After a 1 h incubation time, the cells were washed with DPBS and the transfection medium was replaced with fresh growth medium. The cells were then washed again with DPBS after 24 h of initial transfection and trypsinized, and exposed to an alternating magnetic field (5 kA/m, 300 kHz) for a specific amount of time. The cells were then plated back into 12-well plates with fresh media.

Measurement of Mitochondrial Membrane Potential

To analyze mitochondrial stability, flow cytometry after incubation with5,59,6,69-tetrachloro-1,19,3,39-tetraethylbenzimidoazolylcarbocyaninoiodide (JC-1; Molecular

Probes, Eugene, OR, USA) following the manufacturer's protocol was performed. 28 h

after initial transfection, the cells were analyzed using flow-cytometry-based JC-1 assay.

The cells were trypsinized, resuspended in warm DPBS, and incubated with JC-1 (2 µM)

for 15–30 min at 37 °C and 5% CO2. The cells were then centrifuged, resuspended in

500 µL of PBS. Immediately after they were analyzed on a flow cytometer (Gallios,

Beckman Coulter, Inc.) with 488 nm excitation using emission filters appropriate for

Alexa Fluor488 dye at 520 nm and R-phycoerthyrin at 590 nm. Standard compensation

was performed using the carbonyl cyanide3-chlorophenylhydrazone (CCCP)-treated

cells as positive control while untreated cells (no MCNP and no ATAP) were used as

negative controls.

Apoptosis Assay

To assay for apoptosis, we used annexin V-FLUOS abnd propidium iodide staining

(Roche). 10^6 cells were prepared in 1 mL of PBS with 10% FBS in each test tube. The

cells were centrifuged and resuspended in 100 µL of ice-cold annexin V binding buffer

and annexin V-FLUOS and propidium iodide (PI) were added following the

manufacturer's recommendation. The samples were incubated at room temperature in

the dark for 15 min. 400 µL of additional ice-cold annexin V binding buffer was added,

and the samples were kept on ice under foil until they were ready for analysis using flow

cytometry (Gallios, Beckman Coulter, Inc.). Early apoptotic cells with exposed

phosphatidylserine but intact cell membranes bound to annexin V-FITC but excluded

propidium iodide. Cells in necrotic or late apoptotic stages were labeled with both

annexin V-FITC and propidium iodide.

Xenograft Studies in Nude Mice

Following the protocols approved by the Institutional Animal Care and Use

Committee (IACUC) of the The Ohio State University, five-week-old NCR nude mice

(Taconic Farms, Germantown, NY, USA) were implanted subcutaneously in both flanks

with 2×10^6 KYSE cells. After tumors reached 4 to 7 mm in diameter, which took about 9–14 days after implantation, the mice were randomly divided into two groups so that both the mean and the variance of the tumor diameters are of no significant difference among the groups prior to treatment. The ATAP-iRGD-M8 peptide was injected through the tail vein once every 2 days during the whole procedure. Tumor volume was measured by a digital caliper (Thermo Fisher Scientific, Waltham, MA, USA) and determined from the orthogonal dimensions (length, width) using the following formula: tumor volume = $1/2(\text{length} \times \text{width}^2)$. The experiments were terminated when tumors reached 1.5 cm in diameter, in accordance to the IACUC guideline. Mice were sacrificed and xenografts were removed and weighed. Mouse body weights were measured every 4 days for toxicological evaluation of peptide treatments. After euthanizing animals, organs (kidney, heart, liver, lung, and spleen) were expanded, fixed in 10% neutral buffered formalin, paraffin embedded, and stained with hematoxylin-eosin (H&E) for pathological analysis.

Chapter 3

3.1 Stem Cell-Based Gene Therapy Using Magnetic Core-Mesoporous Silica Shell

Nanoparticles and Hyperthermia to Enhance the Treatment of Cancer

The text and images used in this chapter have been previously published in Biomaterials

as an original manuscript (Yin, PT; Shah, S; Pasquale, N; Garbuzenko, O.B.; Minko, T.;

Lee, K.-B. Biomaterials 81 (2016) 46-57.) and Perry Yin was the first author.

3.1.1 Introduction

Ovarian cancer is currently the fifth deadliest cancer among women and is the

leading cause of gynecological malignancies.[190] The conventional mode of therapy

consists of cytoreductive surgery, followed by adjuvant platinum/taxane-based

chemotherapy treatment.[191] However, while most ovarian cancer patients exhibit initial

sensitivity to chemotherapy, over 70% of these patients are diagnosed at a late stage,

when the cancer has already metastasized throughout the peritoneal cavity.[192] As a

consequence, the majority of ovarian cancer patients experience recurrence within 18-

24 months and only 20% of them survive longer than 5 years after initial diagnosis.[193]

To enhance the treatment of late-stage cancers, such as advanced ovarian

cancer, mesenchymal stem cell (MSC)-based therapies are emerging as an attractive

alternative to overcome traditional therapies, which lack tumor-targeting capabilities.[194]

MSCs have the innate ability to self-renew and differentiation into multiple lineages.[195]

Interestingly, these cells also demonstrate the intrinsic ability to migrate to tumors

including those of ovarian origin, even following system administration.[196-199] While the

exact mechanism is still unknown, the tumor tropism displayed by MSCs have promoted

the development of stem cell-based gene therapies, in which MSCs are genetically

engineered to express therapeutic molecules, acting as a delivery vehicle to enhance the ability to treat metastatic cancers.[200,201]

To this end, many different therapeutic molecules are being investigated, including agonists of apoptosis such as cytokines, ineterferon-β (IFN- β), and tumor necrosis factor-related apoptosis inducing ligand (TRAIL)[202] and interleukin 12 (IL-12).[203] Of these therapeutic molecules, TRAIL is a particularly attractive therapeutic choice owing to its ability to selective induce apoptosis in malignant cancer cells, but not in most normal healthy cells.[204] However, while TRAIL has been mostly demonstrated to be biocompatible towards normal healthy cells, there have been a number of studies showing the potential hepatotoxicity associated with TRAIL, greatly dampening its clinical potential.[205,206] As such, to limit the hepatotoxic effects of TRAIL, there is a pressing need to develop therapies which can transport TRAIL and deliver it to targeted cancer tissues in a precise spatiotemporal manner.

Herein, we report the novel application of magnetic core-mesoporous silica shell nanoparticles (MCNPs), composed of a highly magnetic zinc-doped iron oxide core ($ZnFe_2O_4$) and a biocompatible mesoporous silica (mSi) shell. This allows for delivery and activation of a heat-inducible gene vector which encodes a secretable form of TRAIL in MSCs (Fig. 3.1). For this purpose, we developed a plasmid encoding heat shock protein 70B' (HSP70B') promoter (Fig. 3.1B), which has previously been demonstrated to be more specific for heat than other heat shock promoters.[207] As such, the MSCs can first be engineered with MCNPs carrying the heat-inducible TRAIL plasmid *in vitro*. Afterwards, these engineered MSCs can be injected *in vivo* and can migrate towards the targeted tumor sites. From here, TRAIL can be specifically expressed in response to mild magnetic hyperthermia (~41 ^{O}C). In this study, we demonstrate the efficient and biocompatible uptake of MCNP-plasmid complexes into MSCs. We observed that the engineering process has no significant effects on MSC differentiation or proliferation.

Furthermore, the engineered MSCs maintain their tumor tropism towards disseminated

peritoneal ovarian cancer xenografts. Critically, we have shown that mild magnetic

hyperthermia, via exposure of the engineered MSCs to an alternating magnetic field, can

be used to specifically raise the intracellular temperature to ~41 $^{\circ}$C, which resulted in the

spatiotemporally selective expression of TRAIL in engineered MSCs. As a result,

significant ovarian cancer cell death and apoptosis were observed both *in vitro* and *in*

vivo. Overall, by combining the tumor targeting capabilities of MSCs with the
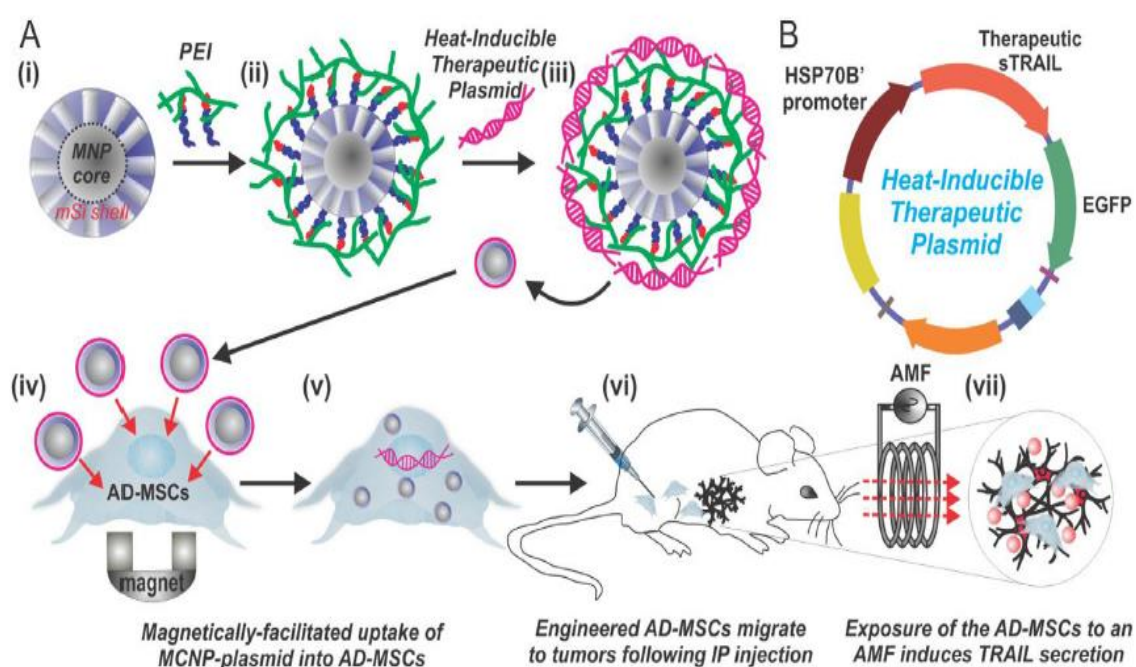
Figure 3.1. Mild Magnetic Hyperthermia Activated Stem Cell Based Gene Therapy. A) MCNPs composed of a $ZnFe_2O_4$ magnetic nanoparticle core (MNP) and a mesoporous silica (mSi) shell (i) are functionalized with PEI to complex to the heat inducible therapeutic plasmid (ii-iii). The MCNPs enhance the delivery of the plasmid into the ADMSCs via magnetically facilitated cellular uptake (iv-v). The engineered ADMSCs can then be injected *in vivo* (vi), where they naturally migrate towards tumors/metastases. Lastly, mild magnetic hyperthermia, via exposure to an AMF, can be utilized to activate the secretion of therapeutic TRAIL from the head inducible plasmid from the engineered ADMSCs (viii). B) The heat inducible plasmid in composed of a HSP70B' promoter and a secretable form of TRAIL (sTRAIL), which can be fused to EGFP to confirm sTRAIL expression.

spatiotemporal MCNP-based delivery and activation of secretable TRAIL, this platform

provides an attractive method to enhance control over the activation of stem cell-based gene therapies.

3.1.2 Results and Discussion

Synthesis and Characterization of the Magnetic Core-Shell Nanoparticles For the dual purpose of both delivering a heat-inducible therapeutic plasmid to the MSCs, we synthesized multifunctional MCNPs with a zinc-doped iron oxide core. These cores have been previously demonstrated to possess significantly higher saturation magnetization as compared to traditional undoped iron oxides.[59] As such, we synthesized $Zn_{0.4}Fe_{0.6}Fe_2O_4$, as these are shown to be the most magnetic composition of Zn-doped iron oxide. This was synthesized via the thermal decomposition of iron pentadionate, iron chloride, and zinc chloride in the presence of oleic acid, oleylamine, and tri-n-octylamine. This protocol was established by others and modified by our group.[174,208-210] Following the synthesis of the magnetic core, a biocompatible mSi shell was formed around the MNP cores via the condensation and polymerization of TEOS in the presence of a micellar CTAB template.[118] TEM showed that the diameter of the cores was 18.93 ± 1.6 nm and that the MNP cores were uniformly coated with a 33.91 ± 3.8 nm thick mSi shell. This increased the overall diameter of the MCNPs to 88.03 ± 8.22 nm **(Fig. 3.2C)**. Based on HR-TEM, the pores were estimated to be approximately 3 nm in diameter (**Fig. 3.2B)** as well as previous literature.[118] To show that the iron oxide cores were monocrystalline cubic spinels, we performed HR-TEM lattice imaging. The fringes were measured to be 4.8A, which is characteristic of the (111) plane of cubic

spinels.[59,174] Finally, FTIR was performed to confirm that the CTAB template was completely removed from the mSi shell (**Figure 3.3C**).

The strong magnetic properties of the MCNPs resulted in a specific absorption rate (SAR) of 564 W/g, based on an AMF with an amplitude of 5 kA/m and a frequency of 225 kHz. This SAR is shown to be consistent with the literature.[208] Furthermore, we demonstrated that these MCNPs, suspended at a concentration of 25 ug/ml, could reach temperatures as high as 47 ^{O}C with an hour exposure to an AMF (Figure 3.2B). Furthermore, we were able to maintain mild magnetic hyperthermia (~43-45 ^{O}C), by
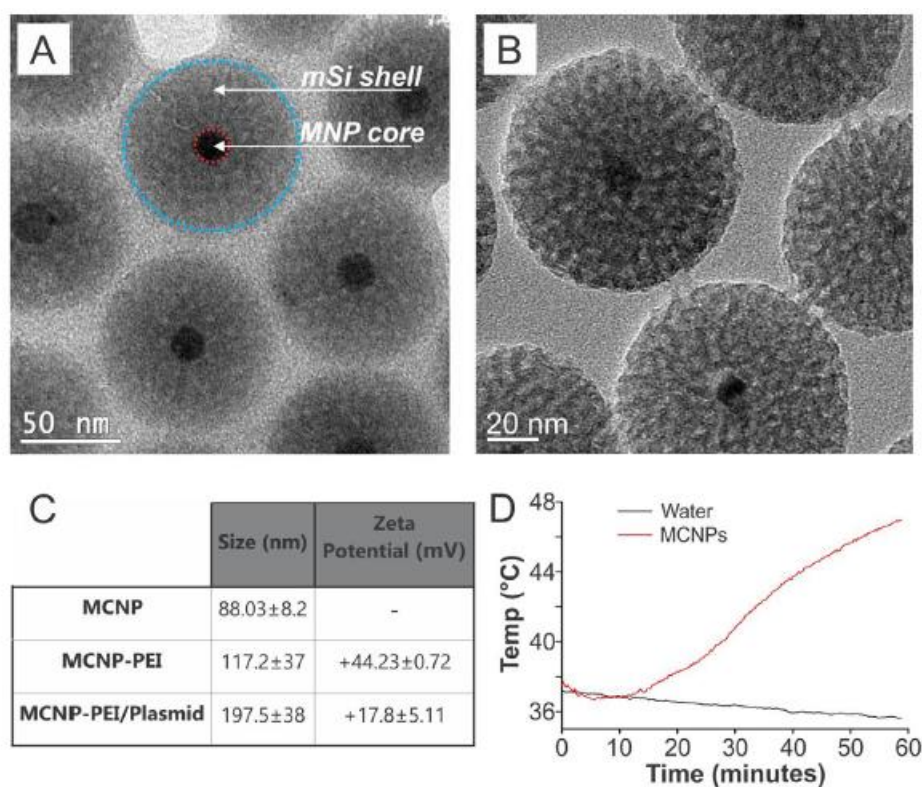
Figure 3.2. Physical Characterization of the MCNPs and their Hyperthermia Potential. A) TEM image of the MCNPs. B) HR-TEM image of the MCNPs, showing that the pores are about 3 nm in size. C) Sizes were determined via TEM and dynamic light scattering (DLS). Zeta potential confirmed on Zetasizer. All Values reported as mean ± standard deviation. D) The MCNPs (25 ug/mL) can be heated to elevated temperatures up to 47 ^{O}C after exposure to an AMF (5 kA/m, 225 kHz) for 1 hour.

periodically exposing the MCNPs to an AMF. As such, we were able to synthesize

monodisperse and water-dispersible MCNPs with narrow size distributions and excellent

magnetic properties to facilitate magnetic hyperthermia, even after the addition of the

non-magnetic mSi shell.
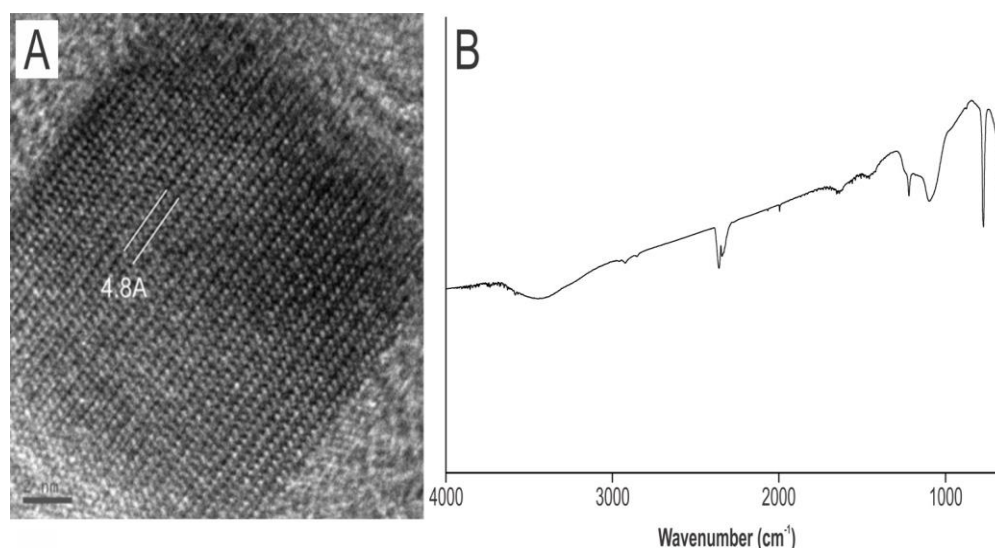
Figure 3.3. Characterization of the MCNPs. A) HRTEM image showing the 4.8 A lattice fringes associated with the (111) planes of cubic phase spinel oxides. The lattice extending uninterrupted across the particle is indicative of its monocrystalline nature. (Scale bar = 2 nm) B) Fourier-Transform infrared spectra (FTIR) analysis of MCNPs after extraction. The absence of methylene C-H stretches ~3,000 cm-1 (symmetric stretch at 2,849 cm and asymmetric stretch at 2,918 cm), originating from CTAB, verifies the success of the extraction and removal of CTAB from the MCNP pores.

Heat-Inducible Plasmid Construction

To gain control over the secretion of TRAIL from MCNP engineered MSCs, we

constructed a heat-inducible TRAIL plasmid using the HSP70B' promoter (Figure 3.1B).

To construct the plasmid, we first cloned the recombinant gene encoding a secretable

form of the human TRAIL protein into the pEGFNP-N1 backbone (Clonetech), to create

a secretable TRAIL-EGFP fusion protein that was constitutively active due to the CMV

promoter (sTRAIL-EGFP plasmid, Fig. 3.4A(i)). In particular, this recombinant TRAIL

gene was composed of the soluble form of the human Flt3L gene (hFlex) at its 5' end

and the human TRAIL gene at the 3' end. Furthermore there was an isoleucine zipper at

the N-terminal of TRAIL, which has been shown to enhance its antitumor activity.[211]

Following insertion of the recombinant TRAIL gene into pEGFP-N1, the CMV promoter

of the resulting TRAIL-EGFP plasmid was replaced with a HSP70B' promoter (Fig. 3
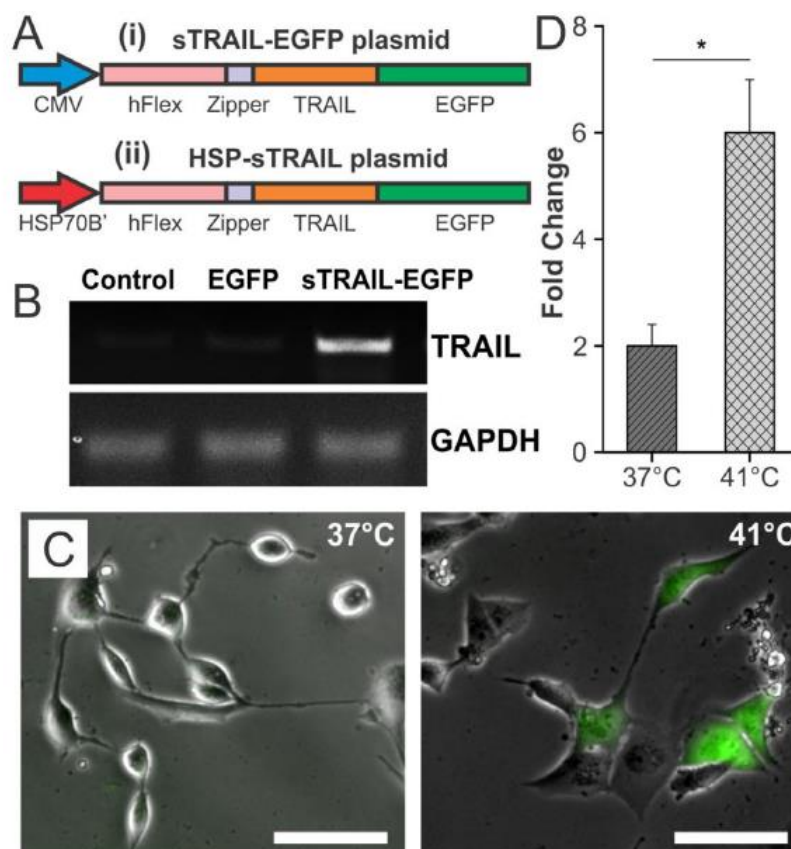
Figure 3.4. Characterization of the Heat Inducible Plasmid. A) Schematic depicting the sTRAIL-EGFP plasmid (i), which expresses sTRAIL-EGFP that is constitutively active, and the HSP-sTRAIL plasmid (ii) which expresses the same sTRAIL-EGFP fusion under the control of a heat inducible HSP70B' promoter. B) RT-PCR showing successful synthesis of the sTRAIL-EGFP plasmid, transfected into A2780 ovarian cancer cells. C) Proof-of-concept showing that the HSP-sTRAIL plasmid can be specifically activated by heat (1 hour at 41 $^{\circ}$C in a water bath) as visualized using fluoresence microscopy due to the fusion of TRAIL with EGFP. (Scale bar = 50 um) D) Confirmation of heat specific TRAIL activation was obtained using qPCR (*$p<0.05$) and was normalized to transfected cells incubated at 37 $^{\circ}$C. GAPDH was utilized as the housekeeping gene.

A(ii)) to enable precise remote control of gene expression utilizing MCNP-mediated mild

magnetic hyperthermia. The precise control is enabled through the HSP70B' promoter,

which has been previously shown to be more specific to heat than other HSPs, which

can be activated by a variety of stresses such as ionizing radiation and oxidative
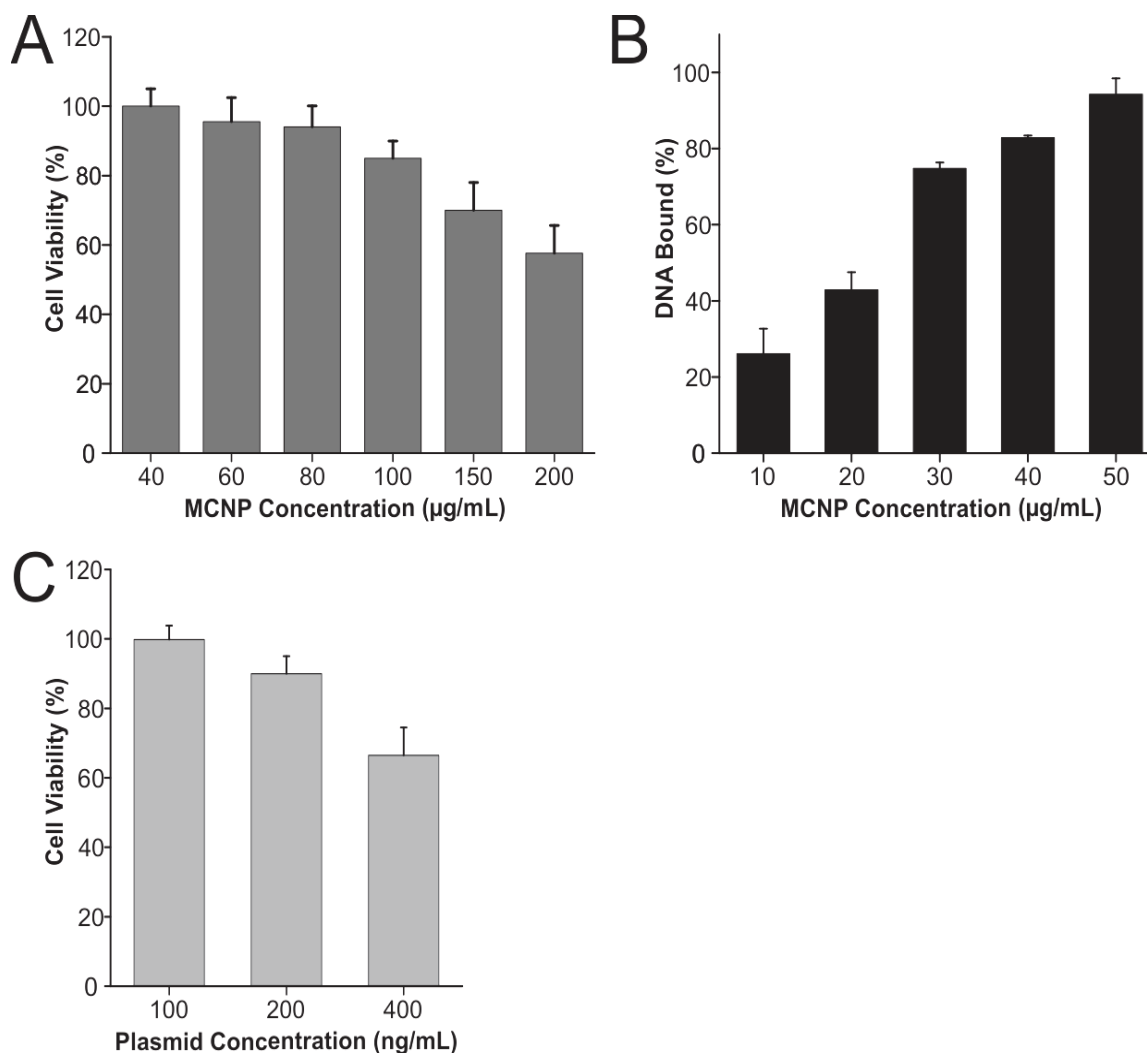
Figure 3.5. Biocompatibility of MCNP-PEI/plasmid complexes. A) Increasing concentrations of MCNP-PEI delivered to A2780 ovarian cancer cells, which was enhanced using magnetofection for 10 min. MTS assay 48 hours after transfection even at concentrations as high as 100 µg/mL shows that the constructs are not cytotoxic to the cell. B) Picogreen assay was used to determine that 50 µg/mL of MCNP-PEI would complex all of the 200 ng/mL of plasmid. C) To determine the highest concentration of plasmid that can be delivered, we complexed 50 µg/mL of MCNP-PEI with increasing plasmid concentrations. We confirmed that 200 ng/mL was optimal for use with the rest of our studies.

stress.[207] To confirm the successful construction of our heat-inducible plasmid, all steps were characterized using restriction enzyme analysis and DNA sequencing.
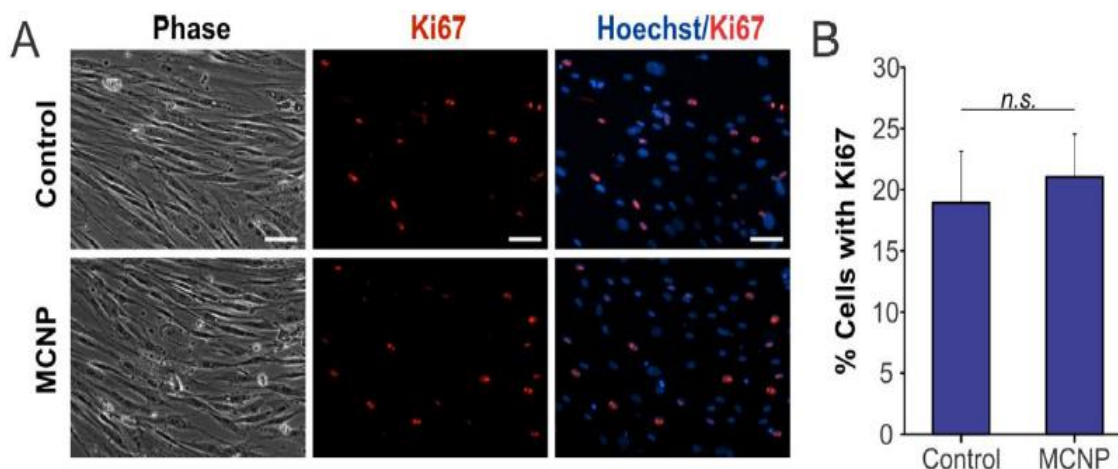
Figure 3.6. Proliferation of Engineered ADMSCs. A) The proliferation of control unengineered and MCNP-PEI-Plasmid engineered ADMSCs was evaluated using Ki-67 (red). The nuclei were stained blue with Hoechst (blue). (Scale bar = 50 um). B) Approximately 20% of ADMSCs expressed Ki-67. There was no statistically significant difference between groups (p>0.05).

Following successful construction of our plasmid, we determined whether they were capable of inducing TRAIL secretion. For this purpose, we performed a proof-of-concept study by delivering constitutively active sTRAIL-EGFP plasmid into A2780 ovarian cancer cells. 48 hours after transfection, total RNA was collected and used to perform reverse transcription PCR (RT-PCR) (Fig. 3.4D). From these results, we were able to confirm that TRAIL is produced in our engineered cells, but not in control. Lastly, we confirmed that heat could be used to induce the secretion of TRAIL in cells engineered with the HSP-sTRAIL plasmid. As such, 24 hours after transfection, the cells were subjected to mild hyperthermia (41 $^{\circ}$C) for 1 hour via exposure to a water bath. Then, 24 hours later, fluorescence microscopy was performed on cells engineered with our plasmid both exposed to and not exposed to (control cells) an AMF to initiate mild

magnetic hyperthermia (Fig. 3.4C). These images show that only cells engineered with

our MCNP-delivered plasmid and exposed to an AMF display green fluorescence

associated with the sTRAIL-EGFP fusion protein. To confirm, total RNA was collected

from engineered cells both exposed to and not exposed to an AMF to initiate mild

magnetic hyperthermia for 1 hour. In the cells exposed to an AMF, TRAIL expression
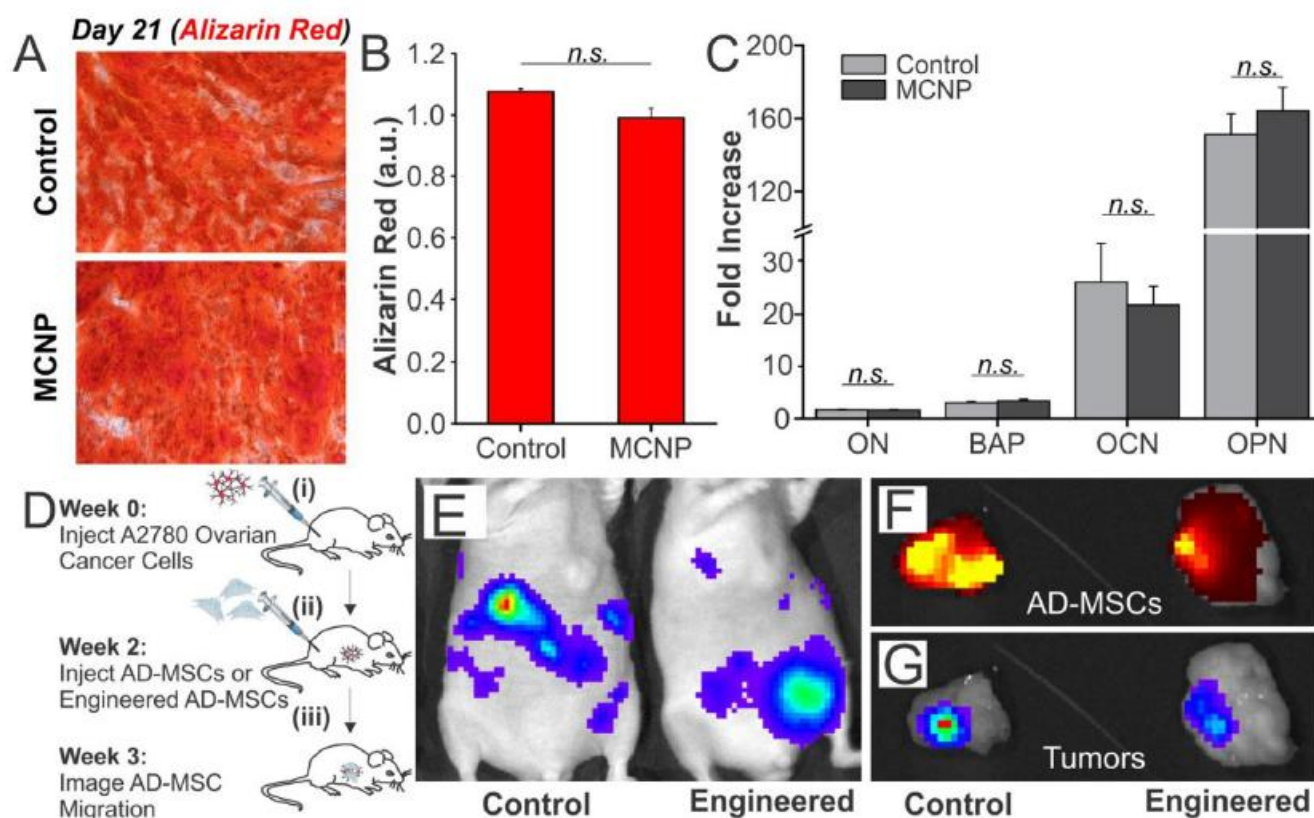
Figure 3.7. Differentiation and Migration of ADMSCs Engineered with MCNP-PEI/Plasmid Complexes. A) To evaluate ADMSC osteogenic differentiation, engineered and unengineered ADMSCs were differentiated for three weeks. Osteogenesis was quantified using Alizarin Red staining (ARS). B) Quantification of ARS suggests that there is no statistically significant difference between the two groups (p>0.05). GAPDH was the housekeeping gene. D) Timeline of studies for evaluating tumor homing capability of the engineered and unengineered ADMSCs. E) Luciferase labelled A2780 cells. Luminescence imaging verifies establishment of disseminated A2790 tumors. The luminescence intensity is color coded where blue is the weakest and red is the strongest. F) One week after the injection of ADMSCs, tumors were harvested. Fluorescence images show the DiD-labeled engineered and unengineered ADMSCs. The fluorescence intensity goes from dark red to yellow, with dark red being the weakest, and yellow the strongest. G) Luminescence images of the conglomerated tumors, demonstrating that the engineered and unengineered ADMSCs can home in to the tumor.

was increased 3 fold (p<0.05) , compared to cells not exposed to an AMF (Fig. 3.4D).

Together, these results clearly demonstrate our ability to construct the heat inducible

plasmid and use MCNP-mediated mild magnetic hyperthermia to induce the expression

of TRAIL.

Engineering MSCs with MCNP-PEI/Plasmid Complexes

In order to optimize the transfection of our MCNP-PEI/Plasmid complexes into

ADMSCs, we initially transfected ADMSCS with MCNP-PEI to determine the optimal cell

loading while maintaining minimal cytotoxicity. ADMSCs were chosen because they

represent an abundant and easily accessible source of adult stem cells with the ability to

differentiate into multiple lineages.[212] After the initial optimization, we used a

concentration of 50 ug/mL, as it induced negligible cytotoxicity (~95% cell viability) and

still provided robust hyperthermia in response to an AMF.

 Next, we complexed the HSP-sTRAIL plasmid with the MCNP-PEI complexes by mixing

them together in solution for 20 minutes. We determined the maximal loading amount of

our plasmid into 50 ug/mL of MCNP via Picogreen assay, which is a dye that binds to

free double –stranded DNA (Fig 3.5B). Final characterization revealed the size of the

MCNP-PEI/Plasmid complexes to be 197.5 ± 38 nm (PDI=.410) with an associated zeta

potential of +17.8 ± 5.11 mV (Fig. 3.2C). Under optimal transfection conditions, we were

able to maintain cell viability at 90% for our engineered ADMSCs (Fig. 3.5C). To

characterize the engineering effect of the proliferation of the ADMSCs, we performed Ki-

67 staining (Fig. 3.6A), which stains for the mitotic marker Ki67. It was shown that there

was no statistically significant difference between our engineered ADMSCs and unengineered ADMSC controls (Fig. 3.6B).

Characterizing the Engineered ADMSCs

After engineering our ADMSCs, we sought to determine whether the engineering affected their ability to differentiate and, most importantly, whether if affected their ability to migrate to cancer *in vivo*. ADMSCs are well known to differentiate into an osteogenic lineage under the appropriate conditions, and, as such, we sought to compare the osteogenic differentiation of our engineered ADMSCs with that of unengineered ADMSCs. This was done via exposure of the cells to osteogenic differentiation media for three weeks (Fig. 3.7).[213] Following week three, we used Alizarin Red S (ARS), which is a typical stain used to evaluate calcium deposition in the extracellular matrix of osteoblasts, as well as qPCR. ARS staining revealed similar calcium deposition between engineered and control ADMSCs (Fig. 3.8A,B). To further confirm that the engineering process had no effect on the behavior of ADMSCs, we performed qPCR on important osteogenic genes such as osteonectin (ON), bone alkaline phosphate (BAP), osteocalcin (OCN), and osteopontin (OPN). No significant difference was found in gene expression between our engineered ADMCSs and control.

Finally, we confirmed that the cell engineering does not impact the ability of the ADMCSs to migrate to tumors *in vivo* (Fig. 3.8E,F,G). As such, we established a metastatic ovarian cancer model where two million A2780 cells were injected intraperitoneally (i.p.) into female nude mice (Fig. 3.8D(i)). To confirm the colocalization of the engineered ADMSCs with tumor cells, the mice, which had disseminated peritoneal A2780 tumors, were injected with a half million engineered or unengineered ADMSCs i.p. at one week post tumor implantation (Fig. 3.8D(ii)). The mice were

harvested after an additional week (Fig. 3.8D(iii)). Multimodality imaging was used to identify the different components, while luciferase was used to identify the A2780 ovarian cancer cells (Fig. 3.8E) and a lipophilic DiD dye was used to label the engineered and unengineered ADMSCs. From Fig. 3.8F and G it can be seen that the
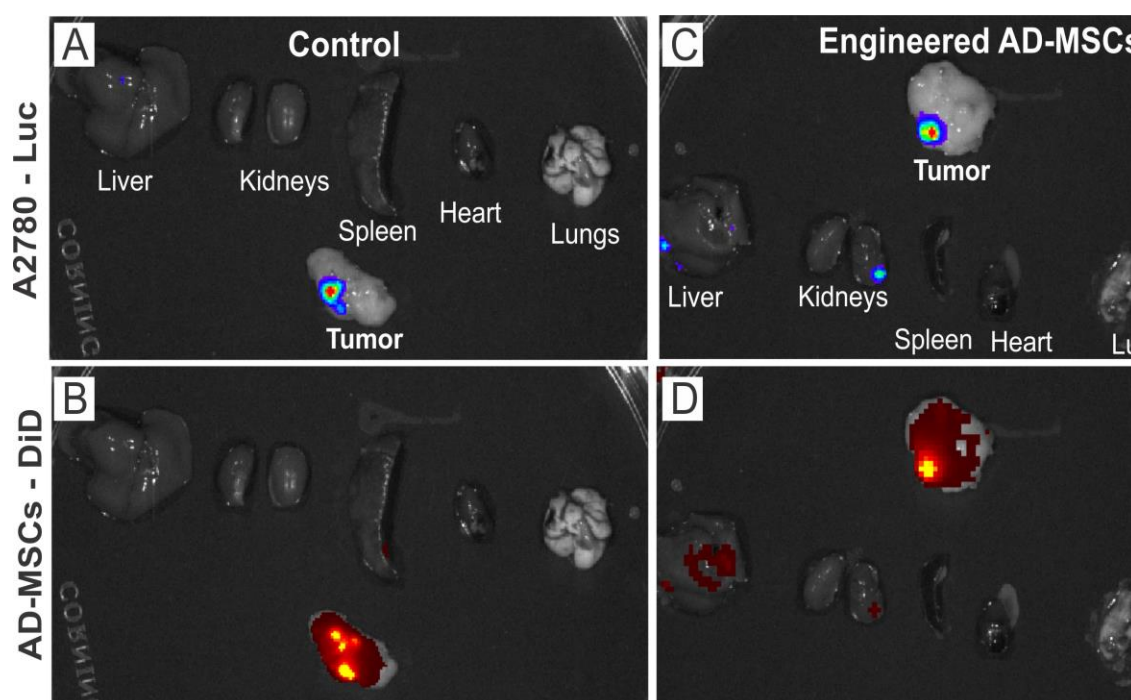
Figure 3.8. **Tumor colocalization of the engineered and unengineered ADMSCs.** 7 days after injection of engineered or unengineered ADMSCs, animals were sacrificed and organs and tumors were collected. A) Luminescence image showing A2780 ovarian cancer cells. B) Fluorescence image showing colocalization of DiD-labeled unengineered control ADMSCs in the tumors but not in the other organs. C) Luminescence image showing A2780 ovarian cancer cells. D) Fluorescence image showing colocalization of DiD-labeled engineered control ADMSCs in the tumors and not in the other organs.

tumors (collected at week 3), the DiD-labeled engineered ADMSCs (Fig 3.8F) co-localized with the luciferase labeled A2780 cells (Fig**.** 3.8G) within one week of ADMSC injection (Figs. 3.9). Critically, there is no significant difference between the co-localization of engineered and unengineered ADMSCs. As such, the engineered

ADMSCs can act as an effective delivery vehicle for MCNP-mediated mild magnetic
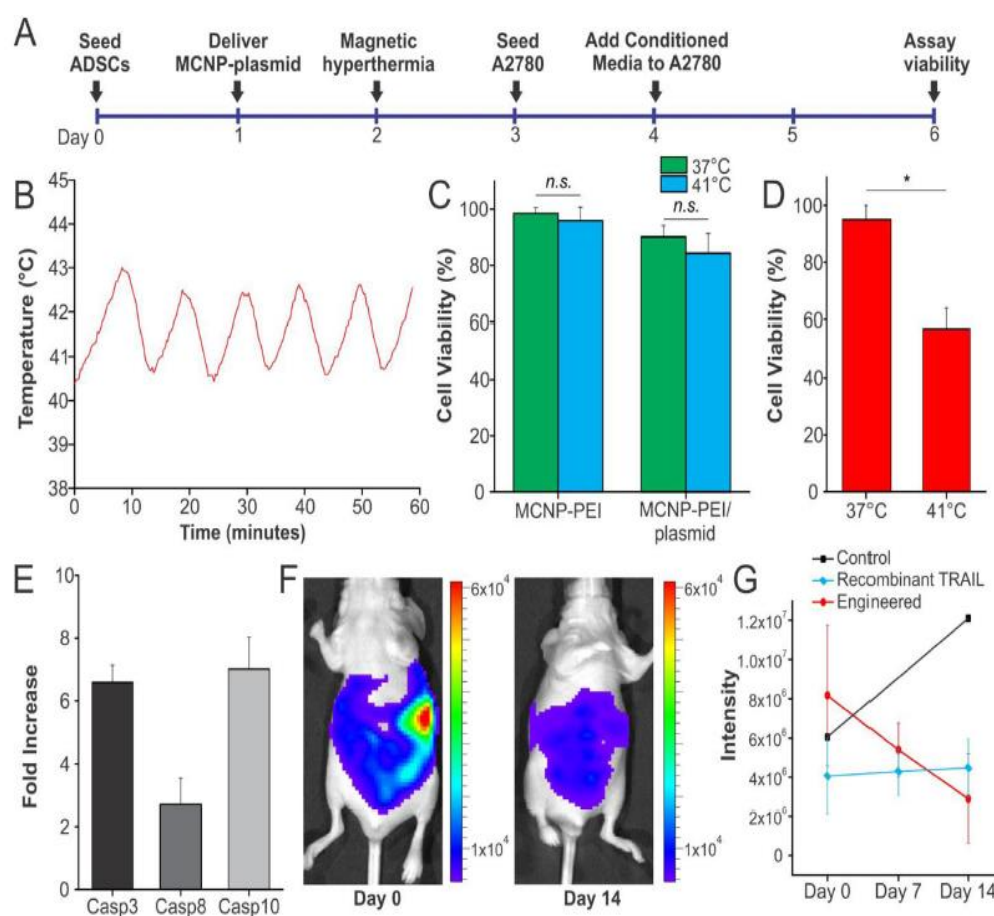
Figure 3.9. Engineered ADMSCs Can Effectively Induce Apoptosis When Exposed to Heat. A) Timeline of *in vitro* study. B) Mild magnetic hyperthermia maintains an average temperature of 41.5 ^{O}C for 1 hour by exposing the engineered ADMSCs to an AMF for 5 minutes on, then 5 minutes off. C) Mild magnetic hyperthermia by itself did not significantly affect ADMSC viability. Furthermore, the engineering process did not significantly affect ADMSC viability. D) To examine the therapeutic efficacy, A2780 ovarian cancer cells were exposed to conditioned media from the engineered ADMSCs exposed to mild magnetic hyperthermia. There is a stark decrease in the viability of the A2780 cells as compared to A2780 cells exposed to conditioned media from engineered ADMSCs not exposed to mild magnetic hyperthermia. E) To verify the mechanism of action, we ran qPCR for caspases, which are downstream of TRAIL. F) To evaluate *in vivo* efficacy, we injected half a million engineered ADMSCs, where the plasmid was sTRAIL-EGFP. Unengineered ADMSCs and a single dose of recombinant TRAIL (5mg/kg) were controls. Tumor volume was monitored over two weeks. It was found that the size of the tumors decreased significantly (max value at day 0 was 6 x 10^4 whereas the max value on day 14 was 8 x 10^3) when treated with engineered ADMSCs. G) Quantification of luminescence intensity, showing the engineered ADMSCs are significantly better than a single dose of recombinant TRAIL.

hyperthermia based gene therapy.

Mild Magnetic Hyperthermia-Activated TRAIL Expression from ADMSCs Can Effectively Induce Apoptosis in Ovarian Cancer Cells

TRAIL-expressing MSCs have been previously shown to induce cancer cell death and decrease tumor and metastasis development *in vivo*.[202] However, in these
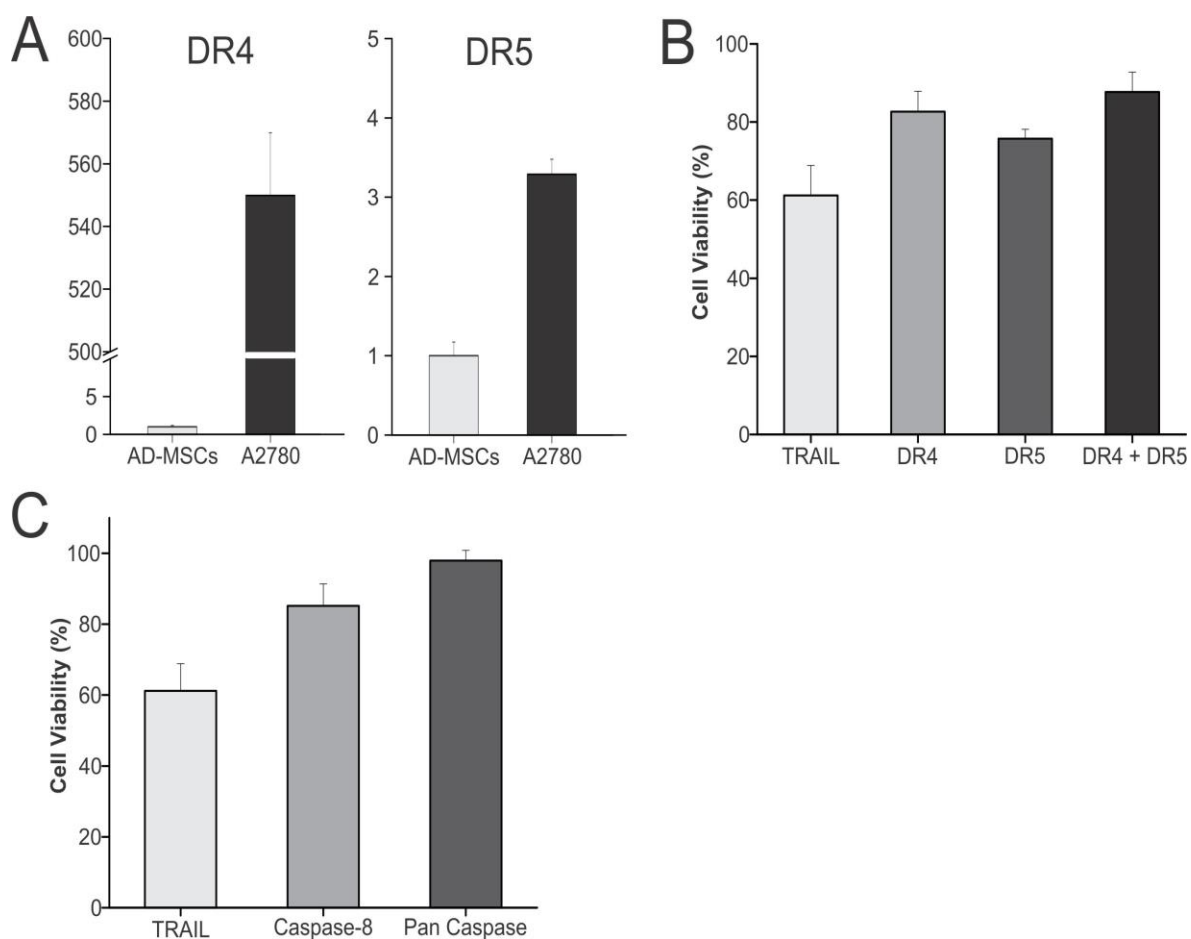
Figure 3.10. Mechanistic studies. A) qPCR demonstrates that DR4 and DR5 are both expressed at much higher levels in A2780 ovarian cancer cells as compared to ADMSCs. The results were normalized to ADMSCs. GAPDH was used as the housekeeping gene. B) Blocking DR4 and/or DR5 with monoclonal antibodies reverses the apoptotic effect of mild magnetic hyperthermia activated secretion of TRAIL from engineered ADMSCs on A2780 cells. A2780 cell viability was measured 24 hours after treatment. C) Specific Inhibition of caspase-8 and non-specific inhibition of caspases could also abrogate the effect of mild magnetic hyperthermia activated secretion of TRAIL from the engineered ADMSCs on A2780 cells. A2780 cell viability was measured 24 hours after treatment.

experiments the TRAIL secretion was either constitutively active or under the control of a doxycycline promoter. However, since TRAIL does possess considerable hepatotoxicity, the ability to remotely express TRAIL in a spatiotemporally controlled manner would enhance the safety and efficacy of TRAIL-expressing stem cell based therapies.

Critically, our experiment design allows us to overcome this major limitation and gain spatiotemporal control over ADMSC-based TRAIL secretion in response to mild magnetic hyperthermia in a remote and non-invasive manner. To this end, we employed the experimental design depicted in Fig.3.10A. 24 hours after transfection of the ADMSCs with the MCNP-PEI/Plasmid complexes, we exposed the cells to an AMF (conditions described previously) to maintain a temperature of approximately 41 $^{\circ}$C for 1 hour (Fig. 3.10B). After about 72 hours from transfection, the conditioned media from the engineered ADMSCs, which contains the secreted TRAIL, was collected. The conditioned media was added to the A2780 ovarian cancer cells (60:40 conditioned:growth media) and after 48 hours its therapeutic efficacy was evaluated. Importantly, the mild magnetic hyperthermia alone did not significantly affect ADMSC viability, in agreement with the effects of heat on stem cell viability in the literature (Fig. 3.10C).[214] After exposure of the A2780 cells in the conditioned media to an AMF, we saw a significant decrease in cell viability of 40%, as compared to control cells which had not been exposed to an AMF.

To confirm that the loss in cell viability was due to mild magnetic hyperthermia activated TRAIL secretion from the engineered ADMSCs, we investigated the underlying mechanism of cell apoptosis. It is known that TRAIL primarily induces apoptosis through death receptor 4 (DR4) and death receptor 5 (DR5), which we confirmed are expressed in A2780 ovarian cancer cells via qPCR.[215] As such, we first investigated the contribution of DR4 and DR5 to the decrease in cell viability. We did this by blocking the DRs with

monoclonal antibodies before the addition of the conditioned media from the mild

magnetic hyperthermia induced TRAIL secretion from ADMSCs. We found that by

blocking DR4 and DR5 alone (82.7% and 75.7% cell viability, respectively) and both

DR4 and DR5 together (87.7% cell viability) was able to abrogate the effect of

conditioned media on A2780 cells.This agrees with the results from our qPCR and

previous literature results.[216,217] Furthermore, upon immunodepletion of TRAIL from the

conditioned media utilizing MNPs functionalized with anti-TRAIL antibodies, it was

observed that the apoptotic effect of the conditioned media on A2780 cells was

abrogated (90.1% cell viability). We next sought to determine whether there was

significant activation of caspases in response to our engineered TRAIL therapy, as it has

been reported that TRAIL acts primarily through the activation of caspase-8 and

subsequent activation of caspase-3.[218] Indeed, only MCNP-PEI/Plasmid engineered

cells exposed to an AMF were found to have significant activation of caspases (Fig.

3.10E). Finally, we demonstrated that the specific inhibition of caspase-8 (85.2% cell

viability) vs the non-specific inhibition of caspases (97.9%) were able to abrogate the

effects of the conditioned media on A2780 cells. These results confirm that the observed

decrease in cell viability is in fact due to the mild magnetic hyperthermia0activated

secretion of TRAIL from the engineered ADMSCs.

Lastly, we conducted *in vivo* studies, where engineered ADMSCs were delivered

into a metastatic ovarian cancer mouse model through i.p. injection. The results from this

study suggest that TRAIL secreting engineered ADMSCs are highly efficient and can

significantly decrease tumor volume as compared to control unengineered ADMSCs, as

well as a control treatment of a single dose of recombinant TRAIL (5mg/kg via i.p.

injection) over a 2 week period (Fig. 3.10F). In particular, we found that a single dose of

a half million engineered ADMSCs, the overall tumor volume (assessed via

luminescence intensity) decreased by over 50% (Fig 3.10G). Conversely, a single dose of recombinant TRAIL did not decrease tumor size. In these animals, the tumor volume remained approximately constant. This is in agreement with previous literature reports due to the short half-life of TRAIL.[219]

3.1.3 Conclusions

We developed a stimuli-responsive stem cell based gene therapy to increase the efficacy of ovarian cancer treatment. In this work, MCNPs were used for the dual purpose of delivering our heat-inducible therapeutic plasmid encoding TRAIL and initiating mild magnetic hyperthermia in response to an AMF, which activates the expression and secretion of TRAIL from our engineered ADMSCs. The ability to control when TRAIL is expressed, in combination with the tumor tropism of ADMSCs, gives us great control over when and where to express therapeutic TRAIL. We showed that this engineering process did not affect the ability of the ADMSCs to proliferate, differentiate, or migrate towards tumors *in vivo*. Furthermore, the mild magnetic hyperthermia induced expression of TRAIL induced significant ovarian cancer cell death both *in vitro* and *in vivo.* As such, we have demonstrated a stimuli-responsive stem cell based gene therapy using MCNPs which can have great potential for both cancer and tissue regeneration.

3.1.4 Materials and Methods

Nanoparticle Synthesis and Characterization

The synthesis of $ZnFe_2O_4$ magnetic nanoparticles (MNPs) has previously been reported and modified by our group.[208-210] Briefly, 1.35 mmol, 0.3 mmol, and 0.7 mmol of Fe(acac)3, ZnCl2, andFeCl2, respectively, were mixed in a round bottom flask with 20 mL of tri-n-octylamine, 6 mmol of both oleic acid and oleylamine, and 10 mmol of 1,2 hexadecanediol. The reaction mixture was heated to 200 ^{O}C for 2 hours. The mixture

was then heated to 305 ^{O}C for 2 hours and the nanoparticles were purified by repeatedly

washing with ethanol. To coat the MNP cores with a mSi shell, a modified procedure

from Hyeon et al. was used [**26**]. 5 mg of the alkyl-capped MNP cores dispersed in

chloroform were sonicated using a probe type sonicator in a 0.1 M aqueous

cetyltrimethylammonium bromide (CTAB) solution. Upon chloroform evaporation, the

CTAB capped MNP cores were diluted to 50 mL with water and the pH of this mixture

was adjusted to ~11 using a 2M NaOH solution. This reaction mixture was heated to 70

^{O}C and, under vigorous stirring, 0.4 mL of tetraethylorthosilicate (TEOS) in 2.4 mL of

ethyl acetate was slowly added. After the addition of TEOS, the reaction was allowed to

continue for 4 h. The MCNPs were collected and washed several times with ethanol. To

remove the template, the nanoparticles were heated to 60 ^{O}C in an ammonium nitrate

solution. The extracted MCNPs were again washed with ethanol. Lastly, the MCNPs

were characterized by high-resolution Transmission electron microscopy (HRTEM) and

Fourier-transform infrared spectra (FTIR). To characterize the magnetic properties of the

nanoparticles, the resulting MCNPs (25 mg/mL in H_2O) were exposed to an AMF (5

kA/m, 225 kHz) using a solid-state induction heating system (Superior Induction

Company) for 1 h. The temperature of the solution was monitored using a fiber optic

temperature probe (LumaSenseTechnologies). To calculate the specific absorption rate (SAR), the following equation was used:

SAR (W/g) = C (dT/dt)(m_s/m_m)

Where C is the specific heat capacity, m_s is the solution mass, m_m is the total magnetic nanoparticle mass, T is the temperature, and t is the time.**27**

Construction of the Plasmids

      To construct the plasmids, we first cloned the recombinant gene that encodes a secreted form of the human TRAIL protein into the pEGFNP-N1 backbone (Clonetech) thereby creating a secretable TRAIL-EGFP fusion that is constitutively active (e.g. via CMV promoter) to allow for monitoring (sTRAIL-EGFP plasmid). In particular, the secreted form of TRAIL was kindly provided by Drs. Leaf Huang (Department of Biomedical Engineering, University of North Carolina at Chapel Hill) and Yukai He (Cancer Center, Georgia Health Sciences University).[211] This recombinant TRAIL gene (sTRAIL)was composed of the soluble form of the human Flt3L gene (hFlex) at the 50 end and the human TRAIL gene at the 30 end (aa residues 95e281) with an isoleucine zipper at the N-terminal of TRAIL, which was previously shown to significantly enhance trimerization of the fusion protein as well as its anti-tumor activity.[211] As such, the cDNA for sTRAIL was amplified using PCR by employing the 50 and 30 primers 50-CGGCCGCTCGAGATGACAGTGCTGGCGCCA- 30 and 50-CGCCGCAAGCTTTTAGCCAACTAA AAAGGC-30, respectively. In this way, the 50 end of the PCR product contained the XhoI restriction site and the 30 end of the PCR product contained the HindIII site. This 1 kb PCR product was digested with XhoI/HindIII and then cloned into pEGFNP-N1 to create the sTRAIL-EGFP fusion. The plasmid was denoted sTRAILEGFP. Similarly, HSP70B0 was ordered from Addgene (Plasmid

#19486) [**29**]. The cDNA for the HSP70B0 promoter was amplified using PCR by employing the 50 and 30 primers 50-GACAATTAATACCATGCAGGCCCCACGGGAGCT- 30 and 50-CGGCGCTCGAGTCAAT CAACCTCCTCAATGA-30, respectively. In this way, the 50 end of the PCR product contained the AseI restriction site and the 30 end of the PCR product contained the XhoI site. This 200 bp PCR product was digested with AseI/XhoI and then cloned into the sTRAIL-EGFP plasmid thereby creating the final HSP-sTRAIL plasmid. The open reading frames of the fusion proteins were confirmed by DNA sequencing (Macrogen).

Formation of MCNP-PEI/Plasmid Complexes

To prepare the MCNPs for plasmid delivery, the negatively charged MCNPs were coated with polyethyleneimine (PEI), a branched cationic polymer, which grants the MNPs with an overall positive charge. PEI is partially protonated under physiological conditions, allowing for the formation of complexes in the presence of nucleic acids [**30**]. PEIs have been used extensively for the delivery of plasmids and nucleic acids including small interfering RNAs (siRNAs) and microRNAs.[220-222] Specifically, it has been demonstrated that PEI-based complexes are able to enter the cell via caveolae- or clathrin-dependent routes and are able to facilitate release from the endosome with high efficiency via the "proton sponge effect.[223] To coat MCNPs in PEI, the MCNPs, dispersed in a minimal amount of ethanol, were added to a stirring solution containing excess PEI (MW ¼ 25,000; Mn ¼ 10,000) and 20 mM NaCl. This PEI molecular weight (MW) and structure was chosen based on the literature.[224] After stirring overnight, the PEI-coated MCNPs were filtered using a centrifugal filter unit (EMD Millipore, 10,000 MW) to remove excess PEI. To complex the PEI coated MCNPs with plasmid, MCNP-PEI was diluted in a 20 mM NaCl solution and plasmid was added to the solution.

Complexing occured for 20 min. To determine the initial concentration of MNP-PEI that needed to be added to complex 200 ng/mL of plasmid, complexes with increasing concentrations of MNP-PEI were incubated with 200 ng/ mL of plasmid. Afterwards, 100 mL of solution was transferred to a 96-well (black-walled, clear-bottom, non-adsorbing) plate (Corning, NY, USA). A total of 100 mL of diluted PicoGreen dye (1:200 dilution in TriseEDTA (TE) buffer) was added to each sample. Fluorescence measurements were made after 10 min of incubation at room temperature using a M200 Pro Multimode Detector (Tecan USA Inc, NC, USA), at an excitation and emission wavelength of 480 and 520 nm, respectively. All measurements were corrected for background fluorescence from a solution containing only buffer and PicoGreen dye. To characterize the MCNP-PEI/plasmid complexes, dynamic light scattering (DLS) and Zeta Potential analyses were performed using a Malvern Instruments Zetasizer Nano ZS-90 instrument (Southboro, MA). MCNP-PEI/plasmid complexes were prepared using purified water (resistivity ¼ 18.5MU-cm). DLS measurements were performed at a 90° scattering angle at $25\ ^OC$. Z-average sizes of three sequential measurements were collected and analyzed. Zeta potential measurements were collected at $25\ ^OC$, and the Z-average potentials following three sequential measurements were collected and analyzed.

Transfecting Cells with MCNP-PEI/Plasmid Complexes

Twenty-four hours before the magnetofection of MCNP complexes, A2780 ovarian cancer (ATCC) or human adipose-derived mesenchymal stem cells (ADMSCs from Lonza [catalog # PT- 5006]) were seeded into each well of a 12-well plate, so as to attain 80% confluency at the time of transfection. MNP-PEI/plasmid complexes were formed as described above. Thereafter, the MCNP complexes were mixed with Opti MEM (Life Technologies) and added to each well to attain the desired final concentration of plasmid/well. Subsequently, the cell culture plates were placed on a static Nd-Fe-B

magnetic plate (OZ Biosciences, France) for 10 min (as optimized from previous reports).[174] The culture plates were placed back into the incubator for 5 hours and afterwards, the cells were washed with DPBS and the transfection medium was replaced with fresh growth medium. The growth mediums for the cell lines (obtained from ATCC or Lonza) used in the study are as follows: A2780 (DMEM supplemented with 10% FBS, 1% Penicillin-Streptomycin, and 1% Glutamax) and ADMSCs (Lonza ADSC Basal Medium [Catalog # PT-3273] with ADSCGM SQ kit [Catalog # PT-4503]).

Magnetic Hyperthermia

Twenty-four hours after transfection, cells were washed with DPBS, trypsinized, and exposed to an AMF (5 kA/m, 225 kHz) for the desired amount of time. In particular, to achieve a constant temperature of ~41 ^{O}C, the cells were initially exposed to an AMF for 20 min to achieve a temperature of ~43 ^{O}C. Afterwards, the cells were exposed to the AMF for 5 min on, and 5 min off) to maintain the temperature at ~41 ^{O}C. Thereafter, fresh media was added to the treated cells and the cells were plated back into 12-well plates.

Cell Viability Assays

The percentage of viable cells was determined via MTT assay following the standard protocols set by the manufacturer. All measurements were taken 48 hours after transfection. All experiments were conducted in triplicate and averaged. The data is

the absorbance of formazan at 490 nm, considering the control cells (untreated) as 100% viable.

Mild Magnetic Hyperthermia Activated TRAIL Expression From ADMSCs to Induce Apoptosis in Ovarian Cancer Cells

24 hours after the transfection of AD-MSCs with MCNP-PEI/Plasmid complexes (50 mg/mL MCNP, 200 ng/mL of plasmid), we exposed the cells to an AMF (same conditions described previously) to maintain a temperature of approximately 41 ^{O}C for 1 hour. About 72 hours after initial transfection, we collected the conditioned media from the engineered ADMSCs, which contain TRAIL that was secreted from the engineered ADMSCs, and added it (60:40 ratio using normal A2780 growth media) to the A2780 ovarian cancer cells. Following further incubation for 48 hours, the therapeutic efficacy was evaluated using an MTT assay.

Cell Differentiation

To confirm the osteogenic differentiation of the MSCs used, ADMSCs were incubated in CEM until a confluent layer was achieved and then osteogenic medium was added, containing IMDM supplemented with 9% FBS, 9% HS, 2mML-glutamine, 100 U/mL penicillin, 100 mg/mL streptomycin, 50 ng/mL L-thyroxine (Sigma Aldrich), 20 mM b-glycerol phosphate, (Sigma Aldrich), 100 nM dexamethansone (Sigma Aldrich) and 50 mM ascorbic acid (Sigma Aldrich). Medium was changed every 3 to 4 days. After 21 days, cells were fixed in 10% formalin, rinsed with DPBS and Alizarin Red S assay was used to verify mature bone differentiation. To do so, DPBS was removed and the Alizarin Red solution (40 mM, pH 4.2) was added to each well and kept for 30 min with gentle shaking. The pH of the Alizarin Red solution was adjusted using a pH meter (Accumet Basic, AB15, Fisher Scientific, USA). The solution was then removed and cells were

washed with DI water five times. Then, the calcium-stained cells were imaged using an optical microscope (Eclipse TieU, Nikon, Japan). To quantify the results, cells were destained using 10% cetylpyridinium chloride (CPC) in 10 mM sodiumphosphate (pH 7.0) for 30 min at room temperature. Lastly, the concentration Alizarin Red S was determined by measuring its absorbance at 562 nm on a multiplate reader (Tecan, Switzerland).

Immunocytochemistry

Cells were fixed with 4% formaldehyde (Thermo-Scientific) for 15 min, then blocked for 1 hour with 5% normal goat serum (NGS, Life Technologies), and permeabilized with 0.3% Triton X-100 to stain for intracellular markers (Ki-67). The primary antibody for Ki-67 (1:400, Cell Signaling, catalog # 9449S) was incubated overnight at 4 ^{O}C. Alexa Fluor 546-conjugated secondary antibodies were used to detect the primary antibodies (1:200, Molecular Probes) and Hoechst 33342 (1:100, Life Technologies) was used as a nuclear counterstain. The substrates were mounted on glass slides using ProLong® Gold antifade (Life Technologies) and imaged using a Nikon TE2000 Fluorescence Microscope.

PCR Analysis

Total RNA was extracted 48 hours post transfection using Trizol Reagent (Life Technologies) and the mRNA expression level of genes of interest were analyzed using quantitative PCR (qPCR). cDNA was generated from 1 mg of total RNA using the Superscript III First-Strand Synthesis System (Life Technologies). Analysis of the mRNA was accomplished using primers specific to each of the target mRNAs. qPCR reactions were carried out using SYBR Green PCR Master Mix (Applied Biosystems) on a StepOnePlus Real-Time PCR System (Applied Biosystems) and the resulting Ct values

were normalized to GAPDH. Standard cycling conditions were used for all reactions with a melting temperature of 60 ^{O}C.

Mechanistic Studies

For blocking experiments, A2780 ovarian cancer cells were incubated in growth media containing 10 ug/mL of the appropriate blocking antibodies for 1 hour before the addition of conditioned media from the engineered ADMSCs (60:40 ratio with normal A2780 growth media). Mouse monoclonal TRAIL-R1/ DR4 (Enzo Life Sciences) and mouse monoclonal TRAIL-R2/DR5 (Enzo Life Sciences) antibodies were used for these experiments. Cell viability was evaluated 24 hours using an MTT assay after the addition of conditioned media. To inhibit caspases, the pan-caspase inhibitor, Z-VAD-FMK (Enzo Life Sciences), and the caspase-8 inhibitor, Z-IETD-FMK (Enzo Life Sciences), was used. For Z-VAD-FMK, a 10 mM stock solution of the inhibitor was prepared using DMSO and the final concentration of the inhibitor and DMSO that the A2780 ovarian cancer cells were exposed to was 20 mM and 0.1%, respectively. For Z-IETDFMK, a 10 mM stock solution of the inhibitor was prepared using DMSO and the final concentration of the inhibitor and DMSO that the A2780 ovarian cancer cells were exposed to was 2 mM and 0.1%, respectively. The A2780 ovarian cancer cells were treated with the inhibitors at the same time as the addition of the conditioned media (60:40 ratio with normal A2780 growth media). Cell viability was evaluated 24 hours after the addition of conditioned media and inhibitors using MTT assay. For TRAIL immunoprecipitation, MCNPS were conjugated with TRAIL monoclonal antibodies (Santa Cruz Biotechnology). For this purpose, the MCNPs were first functionalized with primary amines via the grafting of aminopropyltriethoxysilane (APTES). This was carried out by refluxing 50 mg of MCNPs in 40 mL of toluene with 20 uL of APTES overnight under dry conditions. The resulting amine-functionalized MCNPs were washed several times with

ethanol and resuspended in DMF. The TRAIL antibody (30 uL of 0.1 mg/mL solution) was activated with EDC/NHS coupling in 250 uL of DMF. Then, 1 mg of MCNPs dispersed in 250 uL of DMF was added to the activated TRAIL antibody and allowed to stir overnight. The resulting particles were washed several times with water and resuspended in DPBS. To perform MCNP-based immunoprecipitations, 200 ml of the antibody-conjugated MCNPs (1 mg/mL) was added to 500 ml of conditioned media and incubated on ice for 30 min. To separate the nanoparticles from the conditioned media, a magnet was placed on the side of the vial for 5 minutes and the supernatant was collected and transferred to a new vial. This supernatant was then added to A2780 ovarian cancer cells (60:40 ratio with normal A2780 growth media) and cell viability was evaluated 24 hours afterwards using an MTT assay.

Animal Studies

Human ovarian cancer cells (A2780) expressing luciferase enzymes were purchased from Cell Biolabs, Inc (San Diego, CA). Cells were cultured in DMEM media with L-glutamine (Lonza, Walkersvile, MD) supplemented with 10% fetal bovine serum (Invitrogen, Carlsbad, CA), and 1.2 mL/100 mL penicillinstreptomycin (Gibco, Grand Island, NY). All cells were grown in a humidified atmosphere of 5% $CO2$ (v/v) at 37 ^{O}C. All experiments were performed on cells in the exponential growth phase. 6 to 8 weeks old Athymic nu/nu mice (NCRNU-M, CrTac: NCr- Foxn1nu) were obtained from Taconic (Hudson, NY, USA). All mice were maintained in micro-isolated cages under pathogen free conditions in the animal maintenance facilities of Rutgers, The State University of New Jersey. The research involving animals has been reviewed and approved by the Institutional Animal Care and Use Committee before any research was conducted. Orthotopic (intraperitoneal) ovarian cancer model was created by intraperitoneally injecting 2 x 10^6 A2780 ovarian cancer cells labeled with luciferase into the mice.

Luciferase expressing cancer cells were visualized in live anesthetized animals using an in vivo bioluminescence IVIS system (Xenogen, Alameda, CA). Luciferin (150 mg/kg) was intraperitoneally administered 10 min before imaging. Mice were anesthetized with isoflurane (4% for induction of anesthesia and 1 to 2% for maintenance) using a XGI-8 Gas Anesthesia System (Xenogen, Alameda, CA) for imaging as previously described .[225,226] After allowing 2 weeks for the tumors to develop, ADMSCs were administered. For ADMSC injection, ADMSCs were engineered with MCNP-PEI/Plasmid complexes as previously above. 24 hours after transfection, Vybrant DiD Cell-labeling solutionwas used (Molecular Probes, Catalog # V-22887) to label the cells prior to administration to animals. Specifically, staining media was prepared by adding 5 mL of the supplied DiD solution for every 1 mL of normal growth media required. The media from the engineered or unengineered ADMSCs was then removed and replaced with staining media. ADMSCs were incubated with staining media for 30 min. Afterwards, the labeled AD-MSCs were washed thrice with DPBS, trypsinized, and resuspended such that there were 5×10^5 cells per 300 mL DPBS. Each animal received an intraperitoneal injection of 5×10^5 cells in 300 mL of DPBS. For a control, a single dose of 200 mL (5 mg/kg) of recombinant TRAIL (ProSpec) in DPBS was injected intraperitoneally on day 0. Tumor volume for all animals was then monitored over two weeks by monitoring tumor luminescence. Please note that each group in each experiment had at least three mice.

Chapter 4

4.1 The Use of a Novel Core-Shell Architecture to Manage Energy Migration for Enhanced Upconversion Emissions

This work is Pending Publication. The first author is Nicholas Pasquale.

4.1.1 Introduction

Near infrared to visible upconverting lanthanide doped nanoparticles (UCNPs) are an interesting class of inorganic phosphors with the unique capability of absorbing near-infrared light (NIR) and converting it, through the step-wise absorption of photons, to ultraviolet (UV) and visible emissions[227]. Together, with their high photostability[228], weak autofluoresence background[133], and the ability of NIR excitation to deeply penetrate biological tissues[229], UCNPs are advancing the fields of sub-cellular labeling[102,230], in vivo bioimaging[83,231], biosensing[91,103,232] and biomanipulation, such as optogenetics, in fascinating new ways. However, despite their great potential, the most efficient upconversion nanomaterial to date, co-doped NaYF4:Yb,Ln (where Ln=Lanthanide), suffers from relatively poor upconversion efficiencies, especially in response to low-intensity laser excitation.[90,91,233] This is due to several factors such as i) the small absorption cross-section of Yb^{3+}, which sensitizes the UCNPs to the absorption of 980 nm NIR light[234], and ii) the parity forbidden nature of the 4f-4f transitions of the lanthanides[139], iii) and the incorporation of relatively low concentrations of luminescent lanthanides to prevent quenching[235]. As such, UCNPs are typically irradiated with relatively high power density excitations, exceeding the safe dose in many biological applications[83,236] owing to the heating effect of 980 nm NIR excitation.[95]

In order to circumvent these limitations and increase the potential of UCNPs, it is essential to synthesize UCNPs which are able to absorb relatively low power density

excitations and convert them into intense UV and visible emissions. One of the most popular methods for increasing the upconversion efficiency of UCNPs is the creation of core@shell architectures, such as UCNPs coated with a Yb^{3+} doped sensitizing $NaYF_4$ shell[134,237]. This serves to increase the absorption of 980 nm NIR light over the Yb^{3+} sub-
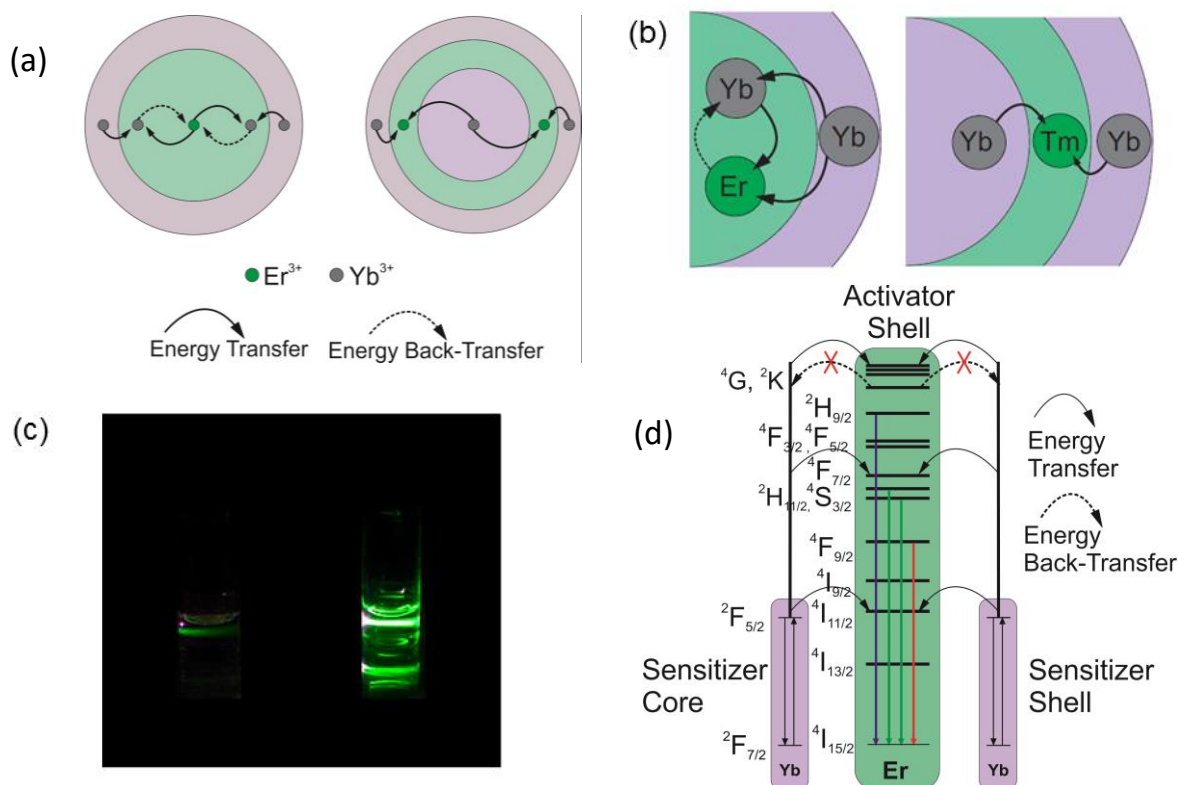
Figure 4.1: Schematic Core@Shell@Shell Sandwich Structured UCNP. A) Depiction of $NaYF_4$:Yb/Er@$NaYF_4$:Yb (left) and $NaYF_4$:Yb/@$NaYF_4$:Er@$NaYF_4$:Yb (right) UCNPs and A,B,) the mitigation of energy back transfer from the sandwich structured UCNP C) leading to significantly increased luminescence, particularly in the green channel. This is largely due to D) the mitigation of energy back transfer due to the sandwich structured architecture.

lattice. The delocalized excitation energy hops along the Yb^{3+} sub-lattice, in a random walk, from the Yb^{3+} doped

sensitizing shell, to the Yb/Ln co-doped core, where it then migrates, via sequential photon absorption, to luminescent lanthanide centers. Since the distance between from the Ln ions to Yb^{3+} is small, and the long lanthanides possess lifetimes orders of magnitude longer than organic dyes, this promotes the excitation of

electrons to successively higher energy levels, resulting in upconversion emission in the UV-visible range[238]. Other energy transfer pathways exist in UCNPs besides the stepwise migration of energy across the Yb^{3+} sub-lattice to luminescent lanthanide, such as Ln-Ln cross-relaxation, and Ln-Yb energy back transfer. It has been

well documented that increases in the concentration of Ln ions beyond 0.2-2 mol% can lead to significant quenching of upconversion luminescence due to Ln-Ln cross-relaxation[4]. However, the

significance of Ln-Yb energy back-transfer has been less well studied. Moreover, it has been demonstrated that the red emissions from Er^{3+} doped $NaYF_4$ are the result of a 3-photon process, involving energy back transfer from the upper lying $^4G/^2K$ manifold to

the $^{5}F_{5/2}$ Yb^{3+} ground state. As such, energy back transfer has a large impact on the

shape of the spectral profile, causing red emissions to occur at the expense of the
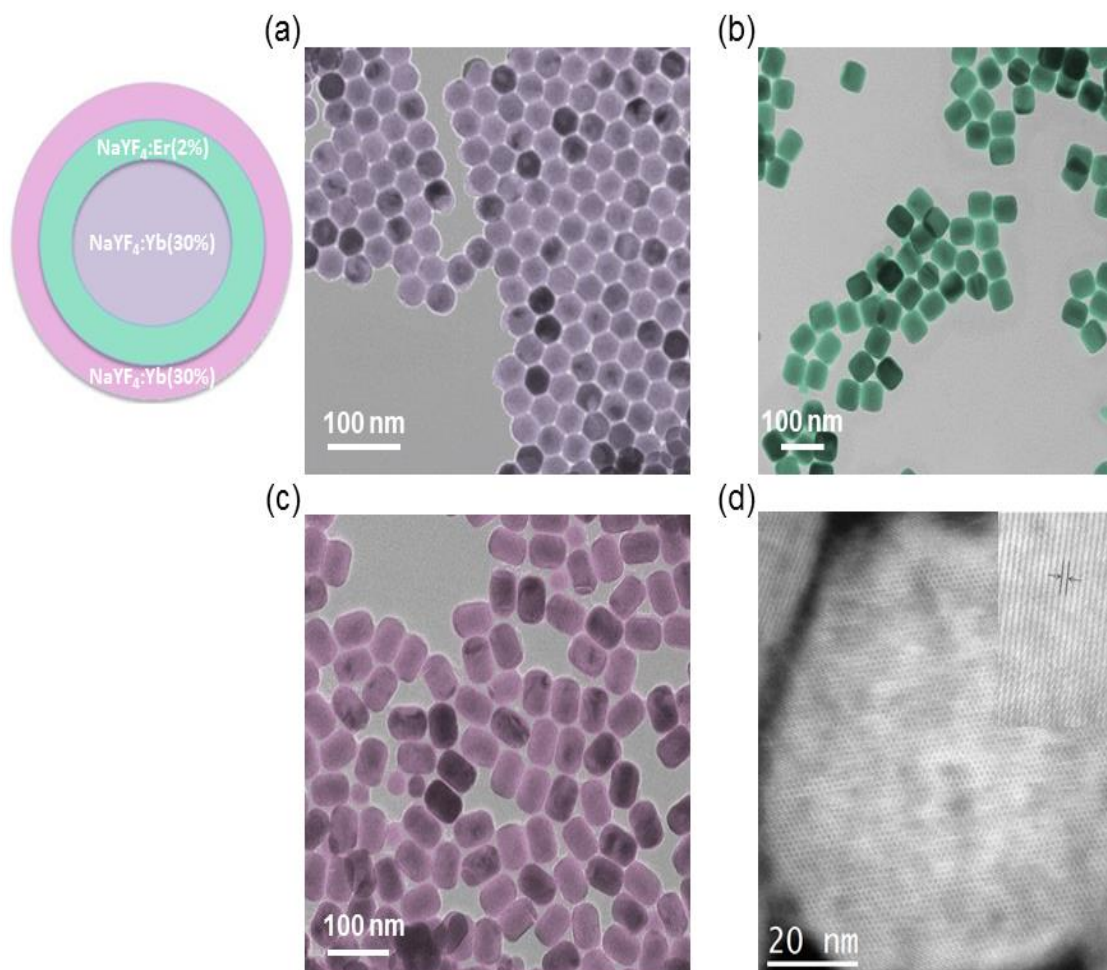
Figure 4.2. Physical Characterization of Yb@Ln@Yb Sandwich Structured UCNPs. A)

Composition of each layer of Yb@Ln@Yb UCNPs. Each layer, corresponding to the UCNPs

shown in A-C) is false colored according to the inset on the left. A-C) Low-Resolution TEM

images of Yb@Ln@Yb sandwich structured UCNPs, constructed layer by layer, using epitaxial

growth. D) High-Resolution Scanning TEM (HR-STEM) characterization of a single Yb@Ln@Yb

UCNP. The uninterrupted lattice and the corresponding d-spacing D, inset) are indicative of

monocrystalline β-hexagonal-phase NaYF$_4$.

dominant higher order green emissions, decreasing the luminescence intensity[239].
Critically, these energy migration dynamics will critically affect the ability of UCNPs to
emit intense higher order UV/visible emissions at the expense of lower order red and
NIR emissions in response to low power density laser excitation, hampering their
potential in bioimaging, sub-cellular labelling, and bio-sensing.

Herein, we describe the design and synthesis of a novel core-shell structured β-
NaYF$_4$:Yb@NaYF$_4$:Ln@NaYF$_4$:Yb (Yb@Ln@Yb sandwich structure) UCNP. This
Yb@Ln@Yb architecture serves to minimize the amount of energy back-transfer from
excited state Ln ions to adjacent Yb^{3+} ions (Fig. 4.1 A,B,), by separating them through
distance into different layers, which significantly increases the higher order multi-photon
emissions from our sandwich structured UCNPs in response to low power density NIR
excitation (Fig. 4.1C). This is accomplished by spatially isolating the sensitizers and
activators in separate layers, which decreases the amount of Yb^{3+} ions close to
luminescent lanthanide centers, and as such decreases the probability of Ln-Yb energy
back transfer (Fig. 4.1D). When compared to traditional co-doped cores (Yb/Ln), and
even co-doped cores coated with sensitizing shells (Yb/Ln@Yb) our Yb@Ln@Yb UCNP
architecture provides significantly more intense higher order multiphoton emissions due
to the mitigation of Ln-Yb energy back transfer. Moreover, this allows our UCNPs to
produce intense upconversion emissions at smaller power densities than possible with
traditional core@shell UCNP architectures. The intense emissions seen with this
sandwich structured Yb@Ln@Yb UCNP represent a large step forward in our
understanding of how to design these materials to enhance their performance as
biosensing, bioimaging, and bio-manipulation agents.

The general structure of the UCNP is composed of an activator (Er or Tm)
containing layer sandwiched between two sensitizing layers doped with Yb^{3+}, as

depicted in Fig. 4.1. This structure allows for the inner and outer Yb^{3+} doped sensitizing layers to harvest 980 nm NIR excitation with high efficiency, funneling it toward the
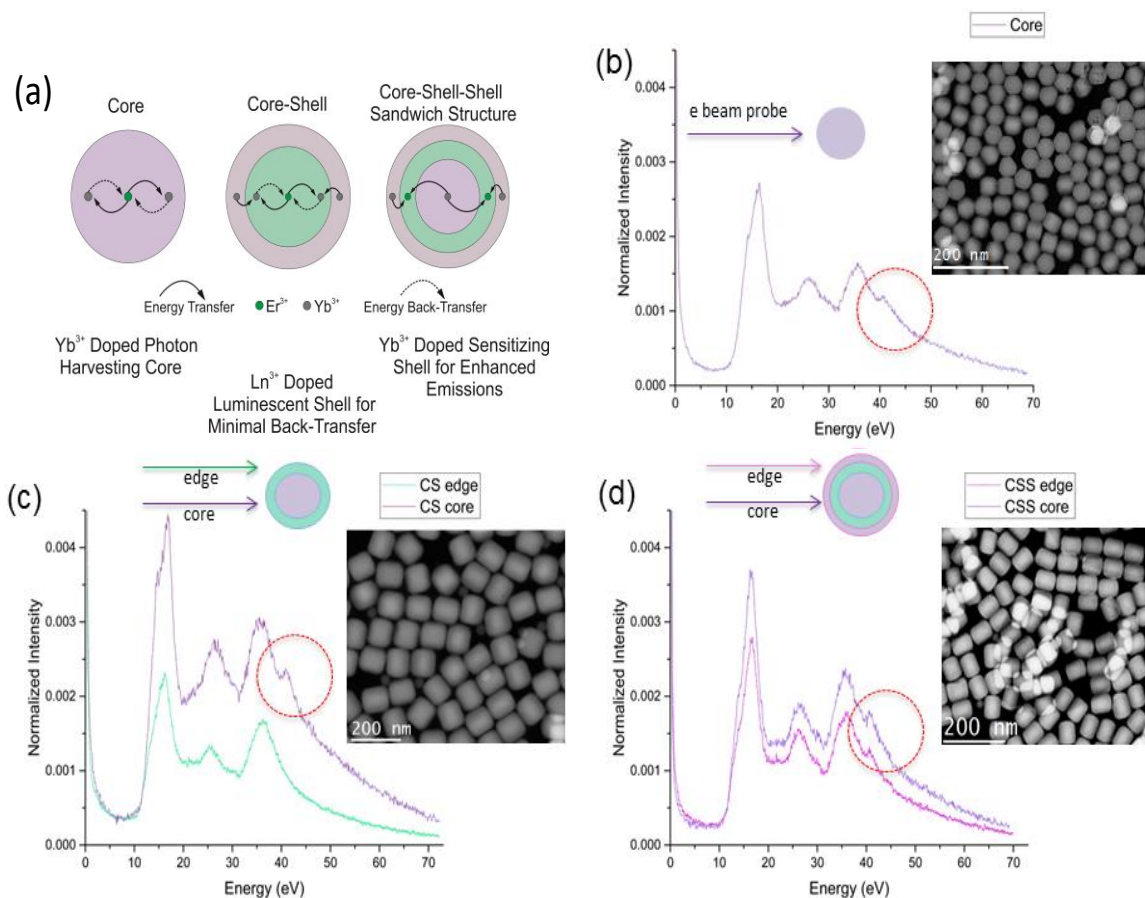
Figure 4.3. Step-by-Step STEM-EELS Characterization of UCNPs. A) Schematic diagram showing the construction of Yb@Ln@Yb structured UCNPs. B) STEM image (inset) and accompanying HR-EELS spectrum of Yb-doped cores. The red circle at 40 eV is indicative of Yb3+, and so is used as a marker for its presence. C) STEM image (inset) and accompanying HR-EELS spectrum of Yb@Er core@shell UCNPs. The peak at 40 eV ascribed to Yb is only present when the edge, or luminescent shell, of the UCNPs is exposed to the electron probe. D) STEM image (inset) and accompanying HR-EELS spectrum of Yb@Ln@Yb sandwich structured UCNPs. The Yb-related peak at 40 V is seen throughout the particle, since the electron probe will always scan through a Yb-doped area (purple on particle schematic).

activator containing luminescent layer where it can promote emissions from the higher energy emissive states of the activator ions. Moreover, this specific arrangement of layers minimizes the number of nearest neighbors between the activating lanthanides in the luminescent shell (LS) and sensitizing Yb^{3+} in the sensitizing core (SC) and sensitizing shell (SS), minimizing the probability of Ln to Yb^{3+} energy back transfer. Critically, this serves to enhance the multi-photon upconversion efficiency of the material at low power density excitations

4.1.2 Results and Discussion

Using these general design principles, we chose $NaYF_4$ as our host matrix due to its well characterized nature, low lattice phonon energies, and relatively higher upconversion efficiencies as compared to other materials[240]. We first synthesized a sensitizing core (SC) containing only Yb^{3+} as a sensitizer (Figure 4.2A). We then grew a 10 nm thick activator containing luminescent shell (LS), which contains only activator (in this work either Tm3+ or Er3+) (Figure 4.2B). We specifically designed the luminescent shell to be 10 nm thick, as this puts the innermost Ln ions of this layer within 5 nm of the Yb^{3+} doped layers, ensuring efficient energy migration to the luminescent Ln centers[241]. Finally, a 10 nm thick outer sensitizing shell (SS) was grown over the particle, sandwiching the LS between the Yb^{3+} containing SC and SS, allowing for efficient energy migration to the emitting lanthanide ions, and strong upconversion emissions[241] (Figure 4.2C). High-Resolution Scanning Transmission Electron Microscopy (HR-STEM) images verify the monocrystalline nature of the UCNPs, which possess the characteristic lattice fringe spacing of β-hexagonal $NaYF_4$ (Figure 4.2D)[125]. The anisotropic shape evolution of the UCNPs from semi-spherical, to hexagonal nanorods is due to the

preferred growth of the $NaYF_4$ along the (100) axis due to the thermodynamically preferential binding of the (0001) face by oleic acid during particle growth[242].

We performed step-by-step single particle Electron Energy Loss Spectroscopy (EELS) to confirm that Yb^{3+} is only present in the SC and SS and that we synthesized our Yb@Ln@Yb sandwich structure (Figure 4.3A). Due to the fact that $NaYF_4$ is extremely sensitive to electron beam irradiation, and can undergo compositional and morphological changes under electron beam irradiation, we rastered the stage through the electron probe by roughly 20 nm throughout the acquisition period for each EELS spectrum. This enabled us to constantly scan new sample area within a given particle, allowing us to ensure that we were below the critical electron dose to prevent structural/compositional changes to the UCNPs. We also verified after each the collection of each group of EELS spectra that there was no visible beam damage to the particle. The spectra were collected using a Gatan CCD. In the EELS spectrum of the Yb^{3+} containing SC, the unique shoulder at 40 eV can be solely ascribed to the 5p to 5d transition of Yb^{3+}[243,244]. Since this is an isolated electronic transition, nd not a collective plasmonic oscillation of electrons, the signal is local in nature, coming from individual Yb^{3+} toms. As such, this shoulder can be found in the SC, regardless of where the electron probe contacts the sample, as the SC contains Yb^{3+} throughout the entire layer(Figure 4.3B). Next, the LS, which contains only luminescent Ln, and no Yb^{3+}, was grown on top of the LC to form Yb@Ln UCNPs and analyzed for the distribution of Yb^{3+}. Since EELs operates via transmission of the electron probe through the sample, we can verify the existence of Yb^{3+} in the core of the UCNP, by rastering the particles central axis across the electron beam. However, when scanning across the edge of the UCNP
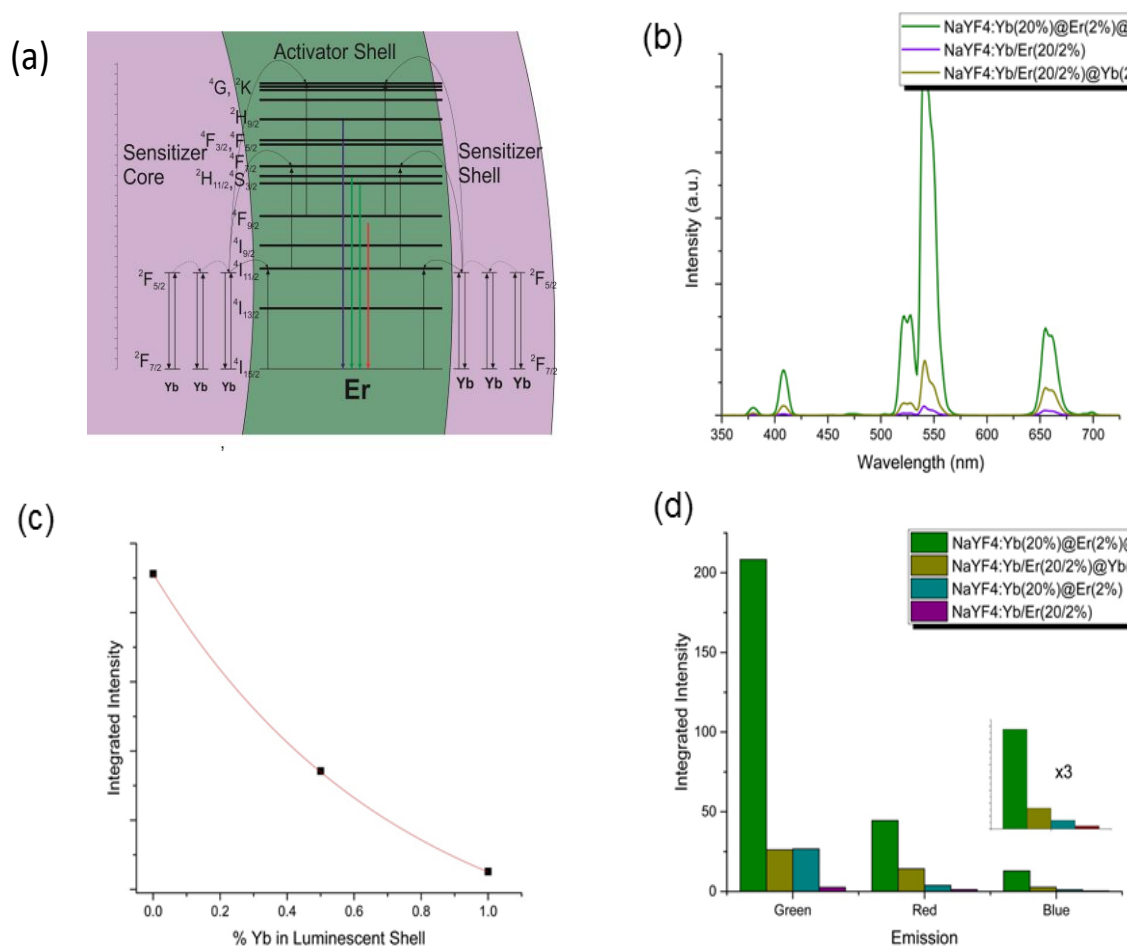
Figure 4.4. Luminescence Characterization of UCNPs . A) Schematic diagram of Yb@Er@Yb

structured UCNPs and the ability of the sandwich structure to mitigate energy back transfer,

via separation of activators and sensitizers. B) Luminescence spectra, demonstrating the large

increase in luminescence over Yb/Er (20/2%) co-dopred cores, and cores coated with an active

shell (Yb20%) that our Yb@Er@Yb (20@2@20%) UCNPs possess in response to low power (1

Watt) density 980 nm NIR light. C) Graph showing the decrease in integrated luminescence

intensity when a Yb is included in the luminescent shell, allowing for energy back transfer and

energy migration throughout the entire particle. D) Bar graph showing the integrated

luminescence intensity for the green, red, and blue channels for different UCNPs. Note the

large increase in the green channel and green to red ratios for our sandwich structured

Yb@Ln@Yb UCNPs.

which contains no Yb^{3+}. This is reflected in the EELS spectra (Figure

4.3C), where the peak at 40 eV, suggestive of Yb^{3+}, only appears during the scan

through the UCNP's central axis, where the electron probe transmits through the particle

core. However, upon scanning the edge of the UCNP, such that the electron beam is

transmitted within the LS, the peak at 40 eV, indicative of Yb^{3+}, is

completely abrogated. A similar result is obtained after the growth of the Yb^{3+} containing

SS, to form Yb@Ln@Yb UCNPs, where regardless of if we raster across the central axis

(analyzing the SC) or the edge (analyzing the SS) we see the presence of Yb^{3+} from the

unique peak at 40 eV (Fig. 4.3D). From these results, our single particle EELS

experiments show that we were able to grow our Yb@Ln@Yb multi-shell UCNPs to have

Yb^{3+} exclusively in the SC and SS layers. Since $NaYF_4$ is exquisitely electron beam

sensitive, and can undergo compositional and morphological changes under the electron

probe, we rastered the stage across the

electron probe by 20 nm for the acquisition period during the collection of each EELS

spectrum. This allowed us to constantly scan new area within a particular region of

particle, ensuring that we were below the critical

electron dose to prevent structural/compositional changes to the UCNPs. We also

confirmed after each set of EELS acquisitions that there was no visible beam damage to

the UCNPs.

After verifying the structure of the UCNPs, we examined the upconversion

spectra of our as synthesized Yb@Ln@Yb UCNPs. When comparing the upconversion

luminescence of our $NaYF_4$:Yb20@Er2@Yb20 sandwich structured UCNPs with

classical $NaYF_4$:Yb/Er (20/2%) co-doped cores, they show a markedly enhanced

luminescence 63 times greater than core UCNPs(Fig. 4.4B). Interestingly, this

enhancement is also seen over Yb/Er co-doped cores which were coated with a Yb^{3+} doped sensitizing shell. Based on our structural design, this is largely due to the mitigation of Er-Yb^{3+} energy back transfer, which occurs to a much greater extent in Yb/Er co-doped UCNP structures (Fig 4.4A). As further evidence of this, it was recently demonstrated that Er-Yb energy back transfer is a part of the 3 photon based red emission of Yb/Er co-doped UCNPs proceeds through relaxation of the population within the $^4G/^2K$ manifold, via energy back transfer to the Yb^{3+} $^2F_{7/2}$ ground state and the commensurate population of the $^4F_{9/2}$ state of Er^{3+}, resulting in red emission. As such, the energy back-transfer from Er-Yb can be said to depopulate the green emitting state in favor of red emissions, resulting in a larger ratio of red to green emissions (Fig. 4.4A)[239]. This result can be confirmed when comparing Yb/Er co-doped UCNPs to Yb@Er UCNPs of the same composition, where the only difference is the isolation of sensitizers and activators into spatially separated shells, which mitigates detrimental Er-Yb energy back transfer, resulting in a 35% increase in green emissions. By further coating the Yb@Ln UCNPs with a SS, to make Yb@Er@Yb UCNPs sandwich structured UCNPs, we see an 80 fold increase in green emissions as compared to Yb/Er co-doped UCNP controls and an 8 fold increase over Yb/Er@Yb core@sensitizing shell UCNP controls (Fig. 4.4D). Furthermore, upon the inclusion of Yb^{3+} into the LS, the luminescence is significantly diminished (Fig. 4.4C), due to the return of energy back transfer, since Yb^{3+} is doped in the luminescent layer in these control UCNPs.

The incredibly enhanced emissions of our sandwich structured UCNPs at low power density excitations provides them with significant advantages over traditionally structured UCNPs in fields such as bioimaging, sub-cellular labelling, and biosensing due to the mitigation of the heating effect from 980 nm NIR excitation and the much higher signal-to-noise ratio achievable with our brighter architecture. In order to demonstrate the utility

of our sandwich structured UCNPs, we designed a simple FRET-based UCNP biosensor utilizing our sandwich structured UCNPs to detect dopamine at extremely low detection limits (pM) (Fig. 3.5A). Dopamine is a critical neurotransmitter which plays an important role in many neuronal circuits, including those involved in mood, emotions, behavior, motor coordination and addiction[245]. Moreover, the loss of dopamine producing cells is a hallmark of Parkinson's disease, which currently affects up to 10 million people globally[246]. As such, it is extremely vital to develop simple, robust, and sensitive biosensors capable of monitoring dopamine production and release from neurons.

To construct the biosensor, we coated our sandwich structured UCNPs with a non-porous silica shell to allow for facile surface functionalization and the isolation of the UCNP from the aqueous environment to prevent water-based luminescence quenching. We then decorated the silica shell with a modified dopamine-specific aptamer.[247,248]. Finally, to complete the assembly of our turn-on biosensor we added 100 nm sized graphene oxide (GO) at increasing concentrations to the UCNP@SiO2-Aptamer complex. The dopamine aptamer interacts with the GO via pi-pi stacking between the GO and the nucleobases of the aptamer, as well as through hydrogen bonding between the nucleobases and the polar groups of GO, quenching the UCNP fluorescence in a concentration dependent fashion (Figure 3.5A,B)[249]. Upon the introduction and dopamine, the aptamer takes binds to it, taking on its 3-dimensional shape, destroying the pi-pi and hydrogen bonding interactions between it and GO, causing the release of GO and the subsequent recovery of fluorescence (Fig. 3.5C)[250]. Due to the extremely efficient upconversion process from our sandwich structured UCNPs it was possible to detect dopamine in the range from 1-10 pM with an R^2=0.94 (Fig. 3.5D). This is 3 orders of magnitude more sensitive than previously demonstrated UCNP-FRET based biosensors, which typically work in the uM to nM range[103,232,249,250]. Critically, this has

important implications for the ability of researchers to monitor the *in situ* production of

dopamine in the cytoplasm of neurons, where it is present in much lower
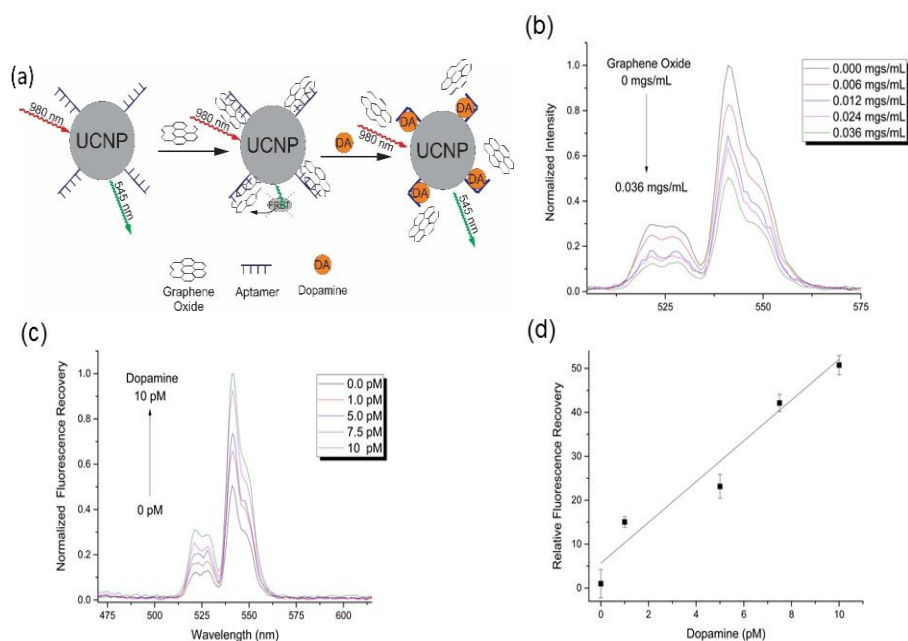
Figure 4.5. Construction of a UCNP-Based Biosensor for the Detection of Dopamine. A) Schematic

diagram showing the construction of the biosensor. The aptamer (left) binds the graphene oxide

(middle), suppressing the green emissions from our UCNPs. Then, in response to dopamine binding

(right), the fluorescence returns due to the separation of the UCNP and graphene oxide, allowing for

dopamine detection. B) UCNP quenching in response to graphene oxide conjugation. C) Return of

fluorescence in response to dopamine binding. D) The response of our UCNP-based biosensor for the

detection of Dopamine at various pM concentrations. All data points consist of 3 independent

measurements.

concentrations[251]. This can provide important findings for the study of related diseases such as Alzheimer's and Parkinson's.

4.1.3 Conclusion

In conclusion, we have successfully demonstrated the rational design and successful synthesis of a novel core@shell structured UCNP, which is able to produce extremely bright emissions in response to relatively low power density excitations. The use of low power 980 nm NIR excitation to produce bright emissions is critical in biological applications, as it minimizes the heating effect of 980 nm NIR excitation due to its overlap with the NIR absorption from water. Furthermore, we demonstrated the utility of our novel core@shell structured UCNP by designing a simple UCNP FRET-based turn-on biosensor, which was able to detect dopamine in low pM concentrations, which is three orders of magnitude lower than similarly designed UCNP-based biosensors. Accordingly, these results demonstrate the incredible potential our novel designed UCNPs can have in materials science and biological settings.

4.1.4 Materials and Methods

Synthesis of Upconversion Nanoparticles

The multi-shelled UCNPs, as well as the cores, were synthesized via a modified procedure. This procedure utilizes high temperature co-precipitation to ensure UCNPs with superior luminescent properties.[88,125]

Synthesis of core β-NaYF4: Yb/ Er (20/2%) nanoparticles.

Yttrium acetate hydrate (1.56mmol), Ytterbium acetate tetrahydrate (0.4mmol) and Erbium acetate hydrate (0.04mmol) were added to a 100-mL 3 neck flask containing 12 mL of oleic acid and 30 mL of 1-octadecene. The mixture was heated at 130 °C for

30 min under vacuum to form the lanthanide-oleate complexes and remove water. Then the solution was cooled down to 50 °C naturally under argon. Thereafter, 10 mL of methanol solution containing NH_4F (8 mmol) and NaOH (5 mmol) was added and the resultant solution was stirred for 30 min. After the methanol was evaporated, the solution was heated to 300 °C under argon for 90 min and then cooled down to room temperature. The resulting nanoparticles were precipitated by addition of ethanol, collected by centrifugation at 3000 rpm for 5 min, washed with ethanol several times, and re-dispersed in 10 mL of hexane.

Synthesis of core β -NaYF4: Yb (20%) nanoparticles.

Yttrium acetate hydrate (1.6 mmol), and Ytterbium acetate tetrahydrate (0.4 mmol) were added to a 100-mL 3 neck flask containing 12 mL of oleic acid and 30 mL of 1-octadecene. The mixture was heated at 130 °C for 30 min under vacuum to form the lanthanide-oleate complexes and remove water. Then the solution was cooled down to 50 °C naturally under argon. Thereafter, 10 mL of methanol solution containing NH_4F (8 mmol) and NaOH (5 mmol) was added and the resultant solution was stirred for 30 min. After the methanol was evaporated, the solution was heated to 300 °C under argon for 90 min and then cooled down to room temperature. The resulting nanoparticles were precipitated by addition of ethanol, collected by centrifugation at 7000 rpm for 5 min, washed with ethanol several times, and re-dispersed in 10 mL of hexane.

Synthesis of core β -NaYF4:Yb(20%)@NaYF4: Er (2%) nanoparticles.

Yttrium acetate hydrate (1.76 mmol), and erbium acetate tetrahydrate (0.036 mmol) were added to a 100-mL 3 neck flask containing 12 mL of oleic acid and 30 mL of 1-octadecene. The mixture was heated at 130 °C for 30 minvunder vacuum to form the lanthanide-oleate complexes and remove water. The solution was then cooled down,

and the B-NaYF4:Yb(20%) UCNPs in hexanes from the previous step were injected as seeds, before distilling off the hexanes. Then the solution was cooled down to 50 °C naturally under argon. Thereafter, 10 mL of methanol solution containing NH₄F (7.2 mmol) and NaOH (4.5 mmol) was added and the resultant solution was stirred for 30 min. After the methanol was evaporated, the solution was heated to 300 °C under argon for 90 min and then cooled down to room temperature. The resulting nanoparticles were precipitated by addition of ethanol, collected by centrifugation at 6000 rpm for 5 min, washed with ethanol several times, and re-dispersed in 10 mL of hexane.

Synthesis of core β -NaYF4:Yb(20%)@NaYF4: Er (2%)@NaYF4:Yb (20%) nanoparticles.

Yttrium acetate hydrate (1.28 mmol), and ytterbium acetate tetrahydrate (0.32 mmol) were added to a 100-mL 3 neck flask containing 12 mL of oleic acid and 30 mL of 1-octadecene. The mixture was heated at 130 °C for 30 minutes under vacuum to form the lanthanide-oleate complexes and remove water. The solution was then cooled down, and the B-NaYF4:Yb(20%)@NaYF4:Er(2%) UCNPs in hexanes from the previous step were injected as seeds, before distilling off the hexanes. Then the solution was cooled down to 50 °C naturally under argon. Thereafter, 10 mL of methanol solution containing NH₄F (6.4 mmol) and NaOH (4 mmol) was added and the resultant solution was stirred for 30 min. After the methanol was evaporated, the solution was heated to 300 °C under argon for 90 min and then cooled down to room temperature. The resulting nanoparticles

were precipitated by addition of ethanol, collected by centrifugation at 5000 rpm for 5 min, washed with ethanol several times, and re-dispersed in 10 mL of hexane.

Synthesis of UCNPs@non-porous silica core-shell nanoparticle, UCNP@SiO2

In a typical procedure, 10 mg of core@shell@shell UCNPs in 8 mL of cyclohexane were mixed with 600 uL of Igepal CO-520 and 80 uL of 30% NH4OH and sonicated using a probe type sonicator at 400W for 60 minutes resulting in a clear stable colloidal solution. Then, the particles were transferred to a round bottom flask, where 60 uL of TEOS was slowly added at room temperature. The microemulsion was allowed to stir overnight. Thereafter, the particles were washed 3 times with ethanol. To coat them with thiol groups, the particles were suspended in 8 mL of dry ethanol, and 6 uL of mercaptopropyltrimethoxysilane was added to the reaction mixture, which was refluxed overnight. The resulting thiol modified UCNP@SiO2 particles were washed three times and suspended in distilled water.

High Resolution Scanning Transmission Electron Microscope (STEM) and Electron Energy Loss Spectroscopy (EELS)

To prepare samples for HAADF-HR-STEM-EELS analysis we dropcasted a freshly prepared colloidal solution of UCNPs onto a carbon coated (200 mesh) copper grid. We then baked the sample, under vacuum, at 150 °C for 5 hours. Upon cooling down we transferred the sample immediately into a Nion UltraSTEM with C1-C4 aberration correction. The microscope was operated at an accelerating voltage of 60 kV, with a condenser setting of 35mrad3i, and a probe diameter of 1 Angstrom for high

resolution STEM imaging. For EELS spectroscopy a 30mrad3i condenser setting was used.

Synthesis of Nano Graphene Oxide

A modified Hummers method was used for the synthesis of nano graphene oxide (NGO). Into a 12 ml concentrated H_2SO_4 solution (98%, Sigma-Aldrich), 1.0 g of graphite (Natural flakes, Sigma-Aldrich), 2.5 g of $K_2S_2O_8$ and 2.5 g P_2O_5 were carefully and slowly added and the mixture was stirred at 80 degree in an oil bath for 8 h to obtain the pre-oxidized graphite. After peroxidation, the graphite was carefully transferred into 500 ml distilled water, stirred for 24 hours and then filtered out. After drying in vacuum for 12 hours, 1.0 g of the pre-oxidized graphite was slowly added into 12.0 ml of H_2SO_4 in an ice bath, followed by a slow addition of 15.0 g $KMnO_4$. The mixture was stirred for 20 minutes and then the temperature was raised to 35 °C and continued to react for 3 hours. Then 250 ml of distilled water was added drop by drop and stirred vigorously for 2 hours. Finally, 700 ml of distilled water and 20 ml 30% H_2O_2 solution were added to quench the reaction, with a bright yellow color appearing for the final solution, indicating the successful synthesis of graphite oxide. The solution was washed with 10% wt. HCl solution and water for 3 times, respectively. After bath sonication for 3 hours and probe type sonication at 400W for 1 hour, the graphene oxide solution was obtained and filtered by a 0.2 μm filter followed by centrifuging at 10,000 rpm for 30 minutes. The concentration of single or few-layered graphene oxide was measured to be 3.0 mg/ml by evaporating water in an oven for overnight.

Dopamine Binding Aptamer Design

To improve the stability of the aptamer and aid in its facile conjugation to the UCNP@SiO_2 surface, we modified the original sequence of the RNA based dopamine

aptamer to a DNA based sequence of /5ThioMC6-D/

GTCTCTGTGTGCGCCAGAGAACACTGGGGCAGATATGGGCCAGCACAGAATGAGG

CCC, where MC6 is a 6 carbon spacer between the actual DNA sequence and the

added thiol group. The thiol group allows for the formation of a disulfide bond to

specifically conjugate the aptamer to the particle surface, with its binding site oriented

away from the particle surface to ensure its ability to bind dopamine.

Aptamer Conjugation to thiol modified UCNP@SiO2 particles

The thiol modified UCNPs suspended in distilled water were transferred to

methanol and allowed to react overnight with dithiopyridine to prepare disulfide modified

UCNP@SiO$_2$ particles. These were then reacted with a thiol modified aptamer at a

concentration of 5 uM and allowed to react overnight. The resulting aptamer modified

UCNPs were washed three times in distilled water and suspended in 2 mL of distilled

water.

Biosensing of Dopamine Using Aptamer Modified UCNP@SiO2 nanoparticles

The UCNP-Aptamer solution was dispersed in PBS at a concentration of 1mg/mL

(UCNP concentration = 0.3mg/mL). To this solution, increasing amounts of graphene

oxide (100 nm) were added to observe the quenching effect of GO on the UCNPs as

they complex with the aptamer. Then, to the UCNP-Aptamer-GO complex, varying

amounts of dopamine were added to observe the recovery in fluorescence. This

fluorescence signal recovery was then correlated to the dopamine concentration added

to solution.

Chapter 5

Conclusions and Perspectives

As is evident from the previous chapters, core-shell inorganic nanoparticles have great potential for use in various biological settings such as cancer treatment and biosensing. Previous works have demonstrated the use of core-shell nanoparticles for simple biological applications such as targeted drug delivery, discussed in the above chapters. However, this thesis has shown several examples of how core-shell nanoparticles can be used for advanced biological applications such as i) targeted drug delivery and hyperthermia for synergistic cancer therapy and imaging ii) magnetically facilitated stem cell engineering for targeted head inducible cancer therapy and iii) the use of core shell architectures to modulate energy migration in upconversion nanoparticles to enhance their luminescent efficiency. Importantly, the use of core-shell architectures in these systems allows for the combination of multiple materials properties into a single nanoparticle to provide multifunctionality to the platform. Moreover, in some cases, the use of core-shell inorganic nanoparticles can offer synergism between the material properties, allowing for new and interesting properties, such as seen in Chapter 4.

In Chapter 2, we successfully demonstrated the use of magnetic core gold shell nanoparticles which were able to increase the efficacy of ATAP treatment in breast cancer cells. The gold shell allowed for facile surface functionalization to conjugate both ATAP and targeting ligands to imbue the core shell nanoparticle with tumor homing capabilities. Moreover, though it was not shown in the associated work, the gold shell can be used for dark field imaging. Likewise, we have previously demonstrated that the

magnetic core can be used for MRI imaging in previous work. Importantly, we demonstrated that the magnetic core can be used to achieve magnetic hyperthermia, which critically, acts to synergistically induce significant apoptosis with ATAP. This is due to the ability of both ATAP and hyperthermia to increase permiabilization of the MOM, causing cytochrome C release, caspase activation and subsequent apoptosis.

In Chapter 3, we successfully demonstrated the novel use of magnetic core mesoporous silica shell nanoparticles to deliver a heat inducible plasmid encoding TRAIL, a therapeutic protein which is largely specific to cancer, despite showing hepatotoxicity. In this work, the nanoparticles act to deliver the therapueetic TRAIL encoding plasmid under the aid of magnetically facilitated delivery. After stem cell engineering, we showed that the stem cells retained their tumor targeting capabilities. We also demonstrated that in response to mild magnetic hyperthermia, the stem cells secreted therapeutic TRAIL protein which induced significant cell death in human ovarian cancer cells. Importantly, the mesoporous silica allowed for the facile delivery of the large DNA plasmid due to its large size and ability to coat with large cationic polymers.Moreover, due to its low density, the mesoporous silica shell did not significantly suppress the magnetic properties of the MNP core, allowing us to initiate mild magnetic hyperthermia under mild conditions using low concentrations of nanoparticle. Furthermore, the pores can be used to load anticancer drugs such as Doxorubicin, which can potentially have synergistic effects on apoptosis.

In Chapter 4, we successfully demonstrated the design and synthesis of a novel core-shell structured UCNP. This novel core-shell architecture served to spatially isolate the sensitizers and activators. In particular, this design mitigated energy back transfer from the sensitizers to the activators, due to their spatially isolated nature.This led to a significant enhancement in upconversion luminescence. We further displayed the utility

of this novel architecture by constructing a simple UCNP FRET-based biosensor. Due to the bright emissions from our novel UCNPs, the biosensor was able to operate in concentrations (pM) three orders of magnitude lower than typical UCNP FRET-based biosensors. This work demonstrated how core-shell structures can be used to manage energy migration in UCNPs to significantly enhance their emissions and modulate the photophysical properties of the UCNPs themselves.

Collectively, this work demonstrates the power and utility of core-shell inorganic nanoparticles for use in cancer therapy, biosensing, and other biological settings. We believe that as research continues to advance, core-shell nanoparticles will be the standard platform for use in biological settings due to their ability to imbue systems with multifunctionality and new materials properties. As such, I hope the work presented in this thesis inspires the use of inorganic core-shell nanoparticles in advanced and novel biological settings. Particularly, in settings where researchers can take advantage of the synergism between the components to use them in new interesting ways.

References

(1)   Lai, J.; Shah, B. P.; Garfunkel, E.; Lee, K.-B. *ACS Nano* **2013**, *7*, 2741.

(2)   Frey, N. A.; Peng, S.; Cheng, K.; Sun, S. *Chemical Society Reviews* **2009**, *38*, 2532.

(3)   Yeh, Y.-C.; Creran, B.; Rotello, V. M. *Nanoscale* **2012**, *4*, 1871.

(4)   Tu, L.; Liu, X.; Wu, F.; Zhang, H. *Chemical Society reviews* **2014**.

(5)   Lübbe, A. S.; Bergemann, C.; Brock, J.; McClure, D. G. *Journal of Magnetism and Magnetic Materials* **1999**, *194*, 149.

(6)   Luo S, W. L., Ding WJ, Wang H, Zhou JM, Jin HK, Su SF, Ouyang WW. *OA Cancer* **2014**, *18*, 1.

(7)   Bulte, J. W. *AJR. American journal of roentgenology* **2009**, *193*, 314.

(8)   Li, X.; Zhang, F.; Zhao, D. *Chemical Society reviews* **2014**.

(9)   Sardar, R.; Shumaker-Parry, J. S. *Journal of the American Chemical Society* **2011**, *133*, 8179.

(10)   Grzelczak, M.; Perez-Juste, J.; Mulvaney, P.; Liz-Marzan, L. M. *Chemical Society reviews* **2008**, *37*, 1783.

(11)   Turkevich, J.; Stevenson, P. C.; Hillier, J. *Discussions of the Faraday Society* **1951**, *11*, 55.

(12)   Frens, G. *Nature Physical Sciences* **1973**, *241*, 2.

(13)   Ji, X.; Song, X.; Li, J.; Bai, Y.; Yang, W.; Peng, X. *Journal of the American Chemical Society* **2007**, *129*, 13939.

(14)   Aslan, K.; Pérez-Luna, V. H. *Langmuir* **2002**, *18*, 6059.

(15)   Brust, M.; Walker, M.; Bethell, D.; Schiffrin, D. J.; Whyman, R. *Journal of the Chemical Society, Chemical Communications* **1994**, 801.

(16)   Xue, Y.; Li, X.; Li, H.; Zhang, W. *Nature communications* **2014**, *5*, 4348.

(17)   Love, J. C.; Estroff, L. A.; Kriebel, J. K.; Nuzzo, R. G.; Whitesides, G. M. *Chemical reviews* **2005**, *105*, 1103.

(18)   Smith, A. M.; Marbella, L. E.; Johnston, K. A.; Hartmann, M. J.; Crawford, S. E.; Kozycz, L. M.; Seferos, D. S.; Millstone, J. E. *Analytical Chemistry* **2015**, *87*, 2771.

(19)   D. Howes, P.; Rana, S.; M. Stevens, M. *Chemical Society reviews* **2014**, *43*, 3835.

(20)   Huang, X.; El-Sayed, M. A. *Journal of Advanced Research* **2010**, *1*, 13.

(21)   Hu, M.; Chen, J.; Li, Z.-Y.; Au, L.; Hartland, G. V.; Li, X.; Marquez, M.; Xia, Y. *Chemical Society reviews* **2006**, *35*, 1084.

(22)   Cao, J.; Sun, T.; Grattan, K. T. V. *Sensors and Actuators B: Chemical* **2014**, *195*, 332.

(23)   Bullen, C.; Zijlstra, P.; Bakker, E.; Gu, M.; Raston, C. *Crystal Growth & Design* **2011**, *11*, 3375.

(24)   Wu, Z.-S.; Jiang, J.-H.; Fu, L.; Shen, G.-L.; Yu, R.-Q. *Analytical Biochemistry* **2006**, *353*, 22.

(25)   Lin, Y. W.; Huang, C. C.; Chang, H. T. *Analyst* **2011**, *136*, 863.

(26)   Yigit, M. V.; Medarova, Z. *American Journal of Nuclear Medicine and Molecular Imaging* **2012**, *2*, 232.

(27)   Rehault, J.; Crisafi, F.; Kumar, V.; Ciardi, G.; Marangoni, M.; Cerullo, G.; Polli, D. *Opt Express* **2015**, *23*, 25235.

(28)   Camp, C. H.; Lee, Y. J.; Heddleston, J. M.; Hartshorn, C. M.; Hight Walker, A. R.; Rich, J. N.; Lathia, J. D.; Cicerone, M. T. *Nature photonics* **2014**, *8*, 627.

(29)   Ghosh, S. K.; Pal, T. *Chemical reviews* **2007**, *107*, 4797.

(30)   Bantz, K. C.; Meyer, A. F.; Wittenberg, N. J.; Im, H.; Kurtulus, O.; Lee, S. H.; Lindquist, N. C.; Oh, S.-H.; Haynes, C. L. *Physical Chemistry Chemical Physics* **2011**, *13*, 11551.

(31)   Cordray, M. S.; Amdahl, M.; Richards-Kortum, R. R. *Analytical Biochemistry* **2012**, *431*, 99.

(32)   Li, T.; Guo, L.; Wang, Z. *Analytical sciences : the international journal of the Japan Society for Analytical Chemistry* **2008**, *24*, 907.

(33)   Nath, N.; Chilkoti, A. *Analytical Chemistry* **2002**, *74*, 504.

(34)   Stringer, R. C.; Schommer, S.; Hoehn, D.; Grant, S. A. *Sensors and Actuators B: Chemical* **2008**, *134*, 427.

(35)   Hutter, E.; Maysinger, D. *Microscopy research and technique* **2011**, *74*, 592.

(36)   Wan, X.-Y.; Zheng, L.-L.; Gao, P.-F.; Yang, X.-X.; Li, C.-M.; Li, Y. F.; Huang, C. Z. *Scientific reports* **2014**, *4*, 4529.

(37)   Kresge, C. T.; Leonowicz, M. E.; Roth, W. J.; Vartuli, J. C.; Beck, J. S. *Nature* **1992**, *359*, 710.

(38)   Trewyn, B. G.; Slowing, I. I.; Giri, S.; Chen, H.-T.; Lin, V. S. Y. *Accounts of Chemical Research* **2007**, *40*, 846.

(39)   Sadasivan, S.; Khushalani, D.; Mann, S. *Journal of Materials Chemistry* **2003**, *13*, 1023.

(40)   Kumar, R.; Chen, H.-T.; Escoto, J. L. V.; Lin, V. S. Y.; Pruski, M. *Chemistry of Materials* **2006**, *18*, 4319.

(41)   Hanrahan, J. P.; Donovan, A.; Morris, M. A.; Holmes, J. D. *Journal of Materials Chemistry* **2007**, *17*, 3881.

(42)   Lim, M. H.; Stein, A. *Chemistry of Materials* **1999**, *11*, 3285.

(43)   Wu, C.-C.; Sailor, M. J. *ACS Nano* **2013**, *7*, 3158.

(44)   Lai, C.-Y.; Trewyn, B. G.; Jeftinija, D. M.; Jeftinija, K.; Xu, S.; Jeftinija, S.; Lin, V. S. Y. *Journal of the American Chemical Society* **2003**, *125*, 4451.

(45)   Quan, G.; Pan, X.; Wang, Z.; Wu, Q.; Li, G.; Dian, L.; Chen, B.; Wu, C. *Journal of Nanobiotechnology* **2015**, *13*, 7.

(46)   Bharti, C.; Nagaich, U.; Pal, A. K.; Gulati, N. *International Journal of Pharmaceutical Investigation* **2015**, *5*, 124.

(47)   Guardado-Alvarez, T. M.; Sudha Devi, L.; Russell, M. M.; Schwartz, B. J.; Zink, J. I. *Journal of the American Chemical Society* **2013**, *135*, 14000.

(48)   Wu, W.; He, Q.; Jiang, C. *Nanoscale Research Letters* **2008**, *3*, 397.

(49)   Massart, R. *IEEE Transactions on Magnetics* **1981**, *17*, 1247.

(50)   Wei, W.; Zhaohui, W.; Taekyung, Y.; Changzhong, J.; Woo-Sik, K. *Science and Technology of Advanced Materials* **2015**, *16*, 023501.

(51)   Scholten, P. C. *Thermodynamics of Magnetic Fluids*; Hemisphere: Washington, DC, 1978.

(52)   Jafari, A.; Farjami Shayesteh, S.; Salouti, M.; Boustani, K. *Journal of Magnetism and Magnetic Materials* **2015**, *379*, 305.

(53)   Lin, X.; Ji, G.; Liu, Y.; Huang, Q.; Yang, Z.; Du, Y. *CrystEngComm* **2012**, *14*, 8658.

(54)   A, L. R. **2004**.

(55)   Kwon, S. G.; Hyeon, T. *Small (Weinheim an der Bergstrasse, Germany)* **2011**, *7*, 2685.

(56)   Strey, R.; Wagner, P. E.; Viisanen, Y. *The Journal of Physical Chemistry* **1994**, *98*, 7748.

(57)   Ling, D.; Lee, N.; Hyeon, T. *Accounts of Chemical Research* **2015**, *48*, 1276.

(58)   Talapin, D. V.; Rogach, A. L.; Kornowski, A.; Haase, M.; Weller, H. *Nano Letters* **2001**, *1*, 207.

(59)   Jang, J. T.; Nah, H.; Lee, J. H.; Moon, S. H.; Kim, M. G.; Cheon, J. *Angew Chem Int Ed Engl* **2009**, *48*, 1234.

(60)   Yu, H.; Li, J.; Loomis, R. A.; Wang, L.-W.; Buhro, W. E. *Nature materials* **2003**, *2*, 517.

(61)   Issa, B.; Obaidat, I. M.; Albiss, B. A.; Haik, Y. *International Journal of Molecular Sciences* **2013**, *14*, 21266.

(62)   Novoselov, K. S.; Geim, A. K.; Dubonos, S. V.; Hill, E. W.; Grigorieva, I. V. *Nature* **2003**, *426*, 812.

(63)   Varón, M.; Beleggia, M.; Kasama, T.; Harrison, R. J.; Dunin-Borkowski, R. E.; Puntes, V. F.; Frandsen, C. *Scientific reports* **2013**, *3*, 1234.

(64)   Cullity, B. D. *Introduction to Magnetic Materials* Addison-Wesley Publishing Company: Reading MA, 1972.

(65)   Stoner, E. C.; Wohlfarth, E. P. *Philosophical Transactions of the Royal Society of London A: Mathematical, Physical and Engineering Sciences* **1948**, *240*, 599.

(66)   Skomski, R.; Coey, J. M. D. *Permanent magnetism*; Institute of Physics Pub.: Bristol, UK; Philadelphia, PA, 1999.

(67)   Neel, L. *C. R. Acad. Sci.* **1949**, 7.

(68)   CP., B. *J. Appl Phys.* **1955**, 2.

(69)   Laurent, S.; Dutz, S.; Häfeli, U. O.; Mahmoudi, M. *Advances in Colloid and Interface Science* **2011**, *166*, 8.

(70)   Terris, B. D.; Thomson, T. *Journal of Physics D: Applied Physics* **2005**, *38*, R199.

(71)   Huang, J.; Li, Y.; Orza, A.; Lu, Q.; Guo, P.; Wang, L.; Yang, L.; Mao, H. *Advanced Functional Materials* **2016**, n/a.

(72)   Hervault, A.; Thanh, N. T. K. *Nanoscale* **2014**, *6*, 11553.

(73)   Sosnovik, D. E.; Nahrendorf, M.; Weissleder, R. *Basic research in cardiology* **2008**, *103*, 122.

(74)   Mishra, S. R.; Dickey, M. D.; Velev, O. D.; Tracy, J. B. *Nanoscale* **2016**, *8*, 1309.

(75)   Zhang, J.; Shin, M. C.; Yang, V. C. *Pharmaceutical research* **2014**, *31*, 579.

(76)   Yin, P. T.; Shah, S.; Pasquale, N. J.; Garbuzenko, O. B.; Minko, T.; Lee, K.-B. *Biomaterials* **2016**, *81*, 46.

(77)   Rosensweig, R. E. *Journal of Magnetism and Magnetic Materials* **2002**, *252*, 370.

(78)   Dong, J.; Zink, J. I. *ACS Nano* **2014**, *8*, 5199.

(79)   Yoo, D.; Jeong, H.; Noh, S.-H.; Lee, J.-H.; Cheon, J. *Angewandte Chemie International Edition* **2013**, *52*, 13047.

(80)   Jayakumar, M. K. G.; Idris, N. M.; Zhang, Y. *Proceedings of the National Academy of Sciences of the United States of America* **2012**, *109*, 8483.

(81)   Park, Y. I.; Lee, K. T.; Suh, Y. D.; Hyeon, T. *Chemical Society reviews* **2015**, *44*, 1302.

(82)   Ushenko, Y. A.; Arkhelyuk, A. D.; Sidor, M. I.; Bachynskyi, V. T.; Wanchuliak, O. Y. *Applied optics* **2014**, *53*, B181.

(83)   Nadort, A.; Sreenivasan, V. K.; Song, Z.; Grebenik, E. A.; Nechaev, A. V.; Semchishen, V. A.; Panchenko, V. Y.; Zvyagin, A. V. *PloS one* **2013**, *8*, e63292.

(84)   Chuang, Y.-J.; Zhen, Z.; Zhang, F.; Liu, F.; Mishra, J. P.; Tang, W.; Chen, H.; Huang, X.; Wang, L.; Chen, X.; Xie, J.; Pan, Z. *Theranostics* **2014**, *4*, 1112.

(85)   Zeng, J. H.; Su, J.; Li, Z. H.; Yan, R. X.; Li, Y. D. *Advanced materials* **2005**, *17*, 2119.

(86)   Mai, H.-X.; Zhang, Y.-W.; Si, R.; Yan, Z.-G.; Sun, L.-d.; You, L.-P.; Yan, C.-H. *Journal of the American Chemical Society* **2006**, *128*, 6426.

(87)   Boyer, J.-C.; Vetrone, F.; Cuccia, L. A.; Capobianco, J. A. *Journal of the American Chemical Society* **2006**, *128*, 7444.

(88)   Li, Z.; Zhang, Y. *Nanotechnology* **2008**, *19*, 345606.

(89)   Peng, X.; Wickham, J.; Alivisatos, A. P. *Journal of the American Chemical Society* **1998**, *120*, 5343.

(90)   Dyck, N. C.; van Veggel, F. C. J. M.; Demopoulos, G. P. *ACS Applied Materials & Interfaces* **2013**, *5*, 11661.

(91)   Huang, P.; Zheng, W.; Zhou, S.; Tu, D.; Chen, Z.; Zhu, H.; Li, R.; Ma, E.; Huang, M.; Chen, X. *Angewandte Chemie* **2014**, *53*, 1252.

(92)   Reid, M. F. *Crystal Field Handbook, ed.*; Cambridge University Press: Cambridge, 2000.

(93)   Liu, G. *Chemical Society reviews* **2014**.

(94)   Auzel, F. *Chemical reviews* **2004**, *104*, 139.

(95)   Ai, F.; Ju, Q.; Zhang, X.; Chen, X.; Wang, F.; Zhu, G. *Scientific reports* **2015**, *5*, 10785.

(96)   Berezin, M. Y.; Achilefu, S. *Chemical reviews* **2010**, *110*, 2641.

(97)   Ye, S.; Chen, G.; Shao, W.; Qu, J.; Prasad, P. N. *Nanoscale* **2015**, *7*, 3976.

(98)   Chan, E. M. *Chemical Society reviews* **2015**, *44*, 1653.

(99)   Chen, F.; Bu, W.; Cai, W.; Shi, J. *Current molecular medicine* **2013**, *13*, 1613.

(100)   Li, X.; Wang, R.; Zhang, F.; Zhou, L.; Shen, D.; Yao, C.; Zhao, D. *Scientific reports* **2013**, *3*, 3536.

(101)   Naczynski, D. J.; Tan, M. C.; Zevon, M.; Wall, B.; Kohl, J.; Kulesa, A.; Chen, S.; Roth, C. M.; Riman, R. E.; Moghe, P. V. *Nature communications* **2013**, *4*, 2199.

(102)   Achatz, D. E.; Ali, R.; Wolfbeis, O. S. *Topics in current chemistry* **2011**, *300*, 29.

(103)   Hao, S.; Chen, G.; Yang, C. *Theranostics* **2013**, *3*, 331.

(104)   Li, Y.; Qi, L.; Shen, Y.; Ma, H. *Analytica chimica acta* **2014**, *811*, 36.

(105)   Khandhar, A. P.; Ferguson, R. M.; Krishnan, K. M. *Journal of Applied Physics* **2011**, *109*, 07B310.

(106)   Mejac, I.; Bryan, W. W.; Lee, T. R.; Tran, C. D. *Anal Chem* **2009**, *81*, 6687.

(107)   Ammar, M.; Mazaleyrat, F.; Bonnet, J. P.; Audebert, P.; Brosseau, A.; Wang, G.; Champion, Y. *Nanotechnology* **2007**, *18*, 285606.

(108)   Prevo, B. G.; Esakoff, S. A.; Mikhailovsky, A.; Zasadzinski, J. A. *Small (Weinheim an der Bergstrasse, Germany)* **2008**, *4*, 1183.

(109)   Ma, L. L.; Borwankar, A. U.; Willsey, B. W.; Yoon, K. Y.; Tam, J. O.; Sokolov, K. V.; Feldman, M. D.; Milner, T. E.; Johnston, K. P. *Nanotechnology* **2013**, *24*, 025606.

(110)   Wang, L.; Park, H.-Y.; Lim, S. I. I.; Schadt, M. J.; Mott, D.; Luo, J.; Wang, X.; Zhong, C.-J. *Journal of Materials Chemistry* **2008**, *18*, 2629.

(111)   Han, P.; Bester, G. *Physical Review B* **2015**, *92*, 125438.

(112)   Junggoo, L.; Joonho, L.; Toshihiro, T.; Hirotaro, M. *Nanotechnology* **2009**, *20*, 475706.

(113)   Schadt, M. J.; Cheung, W.; Luo, J.; Zhong, C.-J. *Chemistry of Materials* **2006**, *18*, 5147.

(114)   Bizmark, N.; Ioannidis, M. A. *Langmuir* **2015**, *31*, 9282.

(115)   Radisic, M.; Iyer, R. K.; Murthy, S. K. *International Journal of Nanomedicine* **2006**, *1*, 3.

(116)   Daniel, M.-C.; Astruc, D. *Chemical reviews* **2004**, *104*, 293.

(117)   Park, H. Y.; Schadt, M. J.; Wang, L.; Lim, II; Njoki, P. N.; Kim, S. H.; Jang, M. Y.; Luo, J.; Zhong, C. J. *Langmuir* **2007**, *23*, 9050.

(118)   Kim, J.; Kim, H. S.; Lee, N.; Kim, T.; Kim, H.; Yu, T.; Song, I. C.; Moon, W. K.; Hyeon, T. *Angewandte Chemie International Edition* **2008**, *47*, 8438.

(119)   Zheng, H.; Gao, C.; Che, S. *Microporous and Mesoporous Materials* **2008**, *116*, 299.

(120)   Backes, S.; Witt, M. U.; Roeben, E.; Kuhrts, L.; Aleed, S.; Schmidt, A. M.; von Klitzing, R. *The Journal of Physical Chemistry B* **2015**, *119*, 12129.

(121)   Chang, B.; Guo, J.; Liu, C.; Qian, J.; Yang, W. *Journal of Materials Chemistry* **2010**, *20*, 9941.

(122)   Conley, G. M.; Nöjd, S.; Braibanti, M.; Schurtenberger, P.; Scheffold, F. *Colloids and Surfaces A: Physicochemical and Engineering Aspects* **2016**, *499*, 18.

(123)   Liu, C.; Guo, J.; Yang, W.; Hu, J.; Wang, C.; Fu, S. *Journal of Materials Chemistry* **2009**, *19*, 4764.

(124)	Thomas, C. R.; Ferris, D. P.; Lee, J.-H.; Choi, E.; Cho, M. H.; Kim, E. S.; Stoddart, J. F.; Shin, J.-S.; Cheon, J.; Zink, J. I. *Journal of the American Chemical Society* **2010**, *132*, 10623.

(125)	Lai, J.; Zhang, Y.; Pasquale, N.; Lee, K. B. *Angewandte Chemie* **2014**, *53*, 14419.

(126)	Boyer, J.-C.; Carling, C.-J.; Gates, B. D.; Branda, N. R. *Journal of the American Chemical Society* **2010**, *132*, 15766.

(127)	Lai, J.; Shah, B. P.; Zhang, Y.; Yang, L.; Lee, K.-B. *ACS Nano* **2015**, *9*, 5234.

(128)	MacDougall, S. K. W.; Ivaturi, A.; Marques-Hueso, J.; Krämer, K. W.; Richards, B. S. *Opt. Express* **2012**, *20*, A879.

(129)	Ma, X.; Ni, X. *J Nanopart Res* **2013**, *15*, 1.

(130)	Shalav, A.; Richards, B. S.; Trupke, T.; Krämer, K. W.; Güdel, H. U. *Applied Physics Letters* **2005**, *86*, 013505.

(131)	van Sark, W. G.; de Wild, J.; Rath, J. K.; Meijerink, A.; Schropp, R. E. I. *Nanoscale Research Letters* **2013**, *8*, 81.

(132)	Wang, Y.-F.; Liu, G.-Y.; Sun, L.-D.; Xiao, J.-W.; Zhou, J.-C.; Yan, C.-H. *ACS Nano* **2013**, *7*, 7200.

(133)	DaCosta, M. V.; Doughan, S.; Han, Y.; Krull, U. J. *Analytica chimica acta* **2014**, *832*, 1.

(134)	Wang, F.; Deng, R.; Liu, X. *Nature protocols* **2014**, *9*, 1634.

(135)	Cui, S.; Yin, D.; Chen, Y.; Di, Y.; Chen, H.; Ma, Y.; Achilefu, S.; Gu, Y. *ACS Nano* **2013**, *7*, 676.

(136)	Park, Y. I.; Kim, H. M.; Kim, J. H.; Moon, K. C.; Yoo, B.; Lee, K. T.; Lee, N.; Choi, Y.; Park, W.; Ling, D.; Na, K.; Moon, W. K.; Choi, S. H.; Park, H. S.; Yoon, S. Y.; Suh, Y. D.; Lee, S. H.; Hyeon, T. *Advanced materials* **2012**, *24*, 5755.

(137)	Wang, C.; Cheng, L.; Liu, Z. *Biomaterials* **2011**, *32*, 1110.

(138)	Downing, E.; Hesselink, L.; Ralston, J.; Macfarlane, R. *Science* **1996**, *273*, 1185.

(139)	Vetrone, F.; Naccache, R.; Mahalingam, V.; Morgan, C. G.; Capobianco, J. A. *Advanced Functional Materials* **2009**, *19*, 2924.

(140)	Wang, F.; Wang, J.; Liu, X. *Angewandte Chemie* **2010**, *49*, 7456.

(141)	Boyer, J. C.; Manseau, M. P.; Murray, J. I.; van Veggel, F. C. *Langmuir* **2010**, *26*, 1157.

(142)	Xie, X.; Gao, N.; Deng, R.; Sun, Q.; Xu, Q. H.; Liu, X. *Journal of the American Chemical Society* **2013**, *135*, 12608.

(143)	Zhong, Y.; Tian, G.; Gu, Z.; Yang, Y.; Gu, L.; Zhao, Y.; Ma, Y.; Yao, J. *Advanced materials* **2014**, *26*, 2831.

(144)	Deng, R.; Qin, F.; Chen, R.; Huang, W.; Hong, M.; Liu, X. *Nat Nano* **2015**, *10*, 237.

(145)	Chow, E. K.-H.; Ho, D. *Science Translational Medicine* **2013**, *5*, 216rv4.

(146)	Ferrari, M. *Nat Rev Cancer* **2005**, *5*, 161.

(147)	Duncan, R. *Nature reviews. Drug discovery* **2003**, *2*, 347.

(148)	Kievit, F. M.; Zhang, M. *Advanced materials* **2011**, *23*, H217.

(149)	Torchilin, V. P.; Lukyanov, A. N. *Drug Discovery Today* **2003**, *8*, 259.

(150)	Sugahara, K. N.; Teesalu, T.; Karmali, P. P.; Kotamraju, V. R.; Agemy, L.; Greenwald, D. R.; Ruoslahti, E. *Science* **2010**, *328*, 1031.

(151)	Langer, R. *Nature* **1998**, *392*, 5.

(152)	Hail, N., Jr. *Apoptosis : an international journal on programmed cell death* **2005**, *10*, 687.

(153)	Solary, E.; Bettaieb, A.; Dubrez-Daloz, L.; Corcos, L. *Leukemia & lymphoma* **2003**, *44*, 563.

(154)	Green, D. R.; Kroemer, G. *Science* **2004**, *305*, 626.

(155)	Green, D. R.; Reed, J. C. *Science* **1998**, *281*, 1309.

(156)	Zhou, F.; Wu, S.; Wu, B.; Chen, W. R.; Xing, D. *Small (Weinheim an der Bergstrasse, Germany)* **2011**, *7*, 2727.

(157)   D'Souza, G. G.; Wagle, M. A.; Saxena, V.; Shah, A. *Biochimica et biophysica acta* **2011**, *1807*, 689.

(158)   Fulda, S.; Galluzzi, L.; Kroemer, G. *Nature reviews. Drug discovery* **2010**, *9*, 447.

(159)   Chen, W.-H.; Xu, X.-D.; Luo, G.-F.; Jia, H.-Z.; Lei, Q.; Cheng, S.-X.; Zhuo, R.-X.; Zhang, X.-Z. *Scientific reports* **2013**, *3*, 3468.

(160)   Constance, J. E.; Lim, C. S. *Therapeutic delivery* **2012**, *3*, 961.

(161)   Ko, J. K.; Choi, K. H.; Pan, Z.; Lin, P.; Weisleder, N.; Kim, C. W.; Ma, J. *Journal of cell science* **2007**, *120*, 2912.

(162)   Ko, J. K.; Choi, K. H.; Peng, J.; He, F.; Zhang, Z.; Weisleder, N.; Lin, J.; Ma, J. *The Journal of biological chemistry* **2011**, *286*, 9038.

(163)   Jacotot, E.; Deniaud, A.; Borgne-Sanchez, A.; Touat, Z.; Briand, J.-P.; Le Bras, M.; Brenner, C. *Biochimica et Biophysica Acta (BBA) - Bioenergetics* **2006**, *1757*, 1312.

(164)   Goldberg, M.; Langer, R.; Jia, X. *Journal of biomaterials science. Polymer edition* **2007**, *18*, 241.

(165)   Cho, K.; Wang, X.; Nie, S.; Chen, Z. G.; Shin, D. M. *Clinical cancer research : an official journal of the American Association for Cancer Research* **2008**, *14*, 1310.

(166)   McCarthy, J. R.; Weissleder, R. *Advanced drug delivery reviews* **2008**, *60*, 1241.

(167)   Pankhurst, Q. A.; Connolly, J.; Jones, S. K.; Dobson, J. *Journal of Physics D: Applied Physics* **2003**, *36*, R167.

(168)   Wust, P.; Hildebrandt, B.; Sreenivasa, G.; Rau, B.; Gellermann, J.; Riess, H.; Felix, R.; Schlag, P. M. *The Lancet. Oncology* **2002**, *3*, 487.

(169)   Shellman, Y. G.; Howe, W. R.; Miller, L. A.; Goldstein, N. B.; Pacheco, T. R.; Mahajan, R. L.; LaRue, S. M.; Norris, D. A. *The Journal of investigative dermatology* **2008**, *128*, 949.

(170)   Salah-Eldin, A. E.; Inoue, S.; Tsukamoto, S.; Aoi, H.; Tsuda, M. *International journal of cancer* **2003**, *103*, 53.

(171)   Nijhuis, E. H.; Le Gac, S.; Poot, A. A.; Feijen, J.; Vermes, I. *International journal of hyperthermia : the official journal of European Society for Hyperthermic Oncology, North American Hyperthermia Group* **2008**, *24*, 357.

(172)   Song, X.; Kim, H. C.; Kim, S. Y.; Basse, P.; Park, B. H.; Lee, B. C.; Lee, Y. J. *Journal of cellular biochemistry* **2012**, *113*, 1547.

(173)   White, M. G.; Saleh, O.; Nonner, D.; Barrett, E. F.; Moraes, C. T.; Barrett, J. N. *Journal of neurophysiology* **2012**, *108*, 2203.

(174)   Shah, B.; Yin, P. T.; Ghoshal, S.; Lee, K.-B. *Angewandte Chemie International Edition* **2013**, *52*, 6190.

(175)   Charafe-Jauffret, E.; Ginestier, C.; Iovino, F.; Wicinski, J.; Cervera, N.; Finetti, P.; Hur, M. H.; Diebel, M. E.; Monville, F.; Dutcher, J.; Brown, M.; Viens, P.; Xerri, L.; Bertucci, F.; Stassi, G.; Dontu, G.; Birnbaum, D.; Wicha, M. S. *Cancer Res* **2009**, *69*, 1302.

(176)   Plank, C.; Schillinger, U.; Scherer, F.; Bergemann, C.; Remy, J. S.; Krotz, F.; Anton, M.; Lausier, J.; Rosenecker, J. *Biological chemistry* **2003**, *384*, 737.

(177)   Scherer, F.; Anton, M.; Schillinger, U.; Henke, J.; Bergemann, C.; Kruger, A.; Gansbacher, B.; Plank, C. *Gene Ther* **2002**, *9*, 102.

(178)   Cherukuri, P.; Glazer, E. S.; Curley, S. A. *Advanced drug delivery reviews* **2010**, *62*, 339.

(179)   Xu, Z.; Hou, Y.; Sun, S. *Journal of the American Chemical Society* **2007**, *129*, 8698.

(180)   Pack, D. W.; Hoffman, A. S.; Pun, S.; Stayton, P. S. *Nature reviews. Drug discovery* **2005**, *4*, 581.

(181)   Liu, Y.; Shipton, M. K.; Ryan, J.; Kaufman, E. D.; Franzen, S.; Feldheim, D. L. *Analytical Chemistry* **2007**, *79*, 2221.

(182)   Kim, C.; Shah, B. P.; Subramaniam, P.; Lee, K.-B. *Molecular Pharmaceutics* **2011**, *8*, 1955.

(183) Mellinghoff, I. K.; Wang, M. Y.; Vivanco, I.; Haas-Kogan, D. A.; Zhu, S.; Dia, E. Q.; Lu, K. V.; Yoshimoto, K.; Huang, J. H.; Chute, D. J.; Riggs, B. L.; Horvath, S.; Liau, L. M.; Cavenee, W. K.; Rao, P. N.; Beroukhim, R.; Peck, T. C.; Lee, J. C.; Sellers, W. R.; Stokoe, D.; Prados, M.; Cloughesy, T. F.; Sawyers, C. L.; Mischel, P. S. *The New England journal of medicine* **2005**, *353*, 2012.

(184) Agemy, L.; Friedmann-Morvinski, D.; Kotamraju, V. R.; Roth, L.; Sugahara, K. N.; Girard, O. M.; Mattrey, R. F.; Verma, I. M.; Ruoslahti, E. *Proceedings of the National Academy of Sciences* **2011**, *108*, 17450.

(185) von Wallbrunn, A.; Holtke, C.; Zuhlsdorf, M.; Heindel, W.; Schafers, M.; Bremer, C. *European journal of nuclear medicine and molecular imaging* **2007**, *34*, 745.

(186) Reers, M.; Smiley, S. T.; Mottola-Hartshorn, C.; Chen, A.; Lin, M.; Chen, L. B. *Methods in enzymology* **1995**, *260*, 406.

(187) Salvioli, S.; Maseroli, R.; Pazienza, T. L.; Bobyleva, V.; Cossarizza, A. *Biochemistry. Biokhimiia* **1998**, *63*, 235.

(188) Fang, M. Z.; Liu, C.; Song, Y.; Yang, G. Y.; Nie, Y.; Liao, J.; Zhao, X.; Shimada, Y.; Wang, L. D.; Yang, C. S. *Carcinogenesis* **2004**, *25*, 865.

(189) Guo, S.; Huang, Y.; Jiang, Q.; Sun, Y.; Deng, L.; Liang, Z.; Du, Q.; Xing, J.; Zhao, Y.; Wang, P. C.; Dong, A.; Liang, X.-J. *ACS Nano* **2010**, *4*, 5505.

(190) Khaider, N. G.; Lane, D.; Matte, I.; Rancourt, C.; Piche, A. *American journal of cancer research* **2012**, *2*, 75.

(191) Bevis, K. S.; Buchsbaum, D. J.; Straughn Jr, J. M. *Gynecologic Oncology* **2010**, *119*, 157.

(192) Aletti, G. D.; Gallenberg, M. M.; Cliby, W. A.; Jatoi, A.; Hartmann, L. C. *Mayo Clinic Proceedings* **2007**, *82*, 751.

(193) McGuire , W. P.; Hoskins , W. J.; Brady , M. F.; Kucera , P. R.; Partridge , E. E.; Look , K. Y.; Clarke-Pearson , D. L.; Davidson , M. *New England Journal of Medicine* **1996**, *334*, 1.

(194) Peer, D.; Karp, J. M.; Hong, S.; Farokhzad, O. C.; Margalit, R.; Langer, R. *Nat Nano* **2007**, *2*, 751.

(195) Pittenger, M. F.; Mackay, A. M.; Beck, S. C.; Jaiswal, R. K.; Douglas, R.; Mosca, J. D.; Moorman, M. A.; Simonetti, D. W.; Craig, S.; Marshak, D. R. *Science* **1999**, *284*, 143.

(196) Spaeth, E. L.; Marini, F. C. In *Stem Cell Migration: Methods and Protocols*; Filippi, M.-D., Geiger, H., Eds.; Humana Press: Totowa, NJ, 2011, p 241.

(197) Ponte, A. L.; Marais, E.; Gallay, N.; Langonné, A.; Delorme, B.; Hérault, O.; Charbord, P.; Domenech, J. *STEM CELLS* **2007**, *25*, 1737.

(198) Yagi, H.; Soto-Gutierrez, A.; Parekkadan, B.; Kitagawa, Y.; Tompkins, R. G.; Kobayashi, N.; Yarmush, M. L. *Cell transplantation* **2010**, *19*, 667.

(199) Coffelt, S. B.; Marini, F. C.; Watson, K.; Zwezdaryk, K. J.; Dembinski, J. L.; LaMarca, H. L.; Tomchuck, S. L.; zu Bentrup, K. H.; Danka, E. S.; Henkle, S. L.; Scandurro, A. B. *Proceedings of the National Academy of Sciences* **2009**, *106*, 3806.

(200) Gao, Z.; Zhang, L.; Hu, J.; Sun, Y. *Nanomedicine: Nanotechnology, Biology and Medicine* **2013**, *9*, 174.

(201) Dwyer, R. M.; Khan, S.; Barry, F. P.; O'Brien, T.; Kerin, M. J. *Stem cell research & therapy* **2010**, *1*, 25.

(202) Loebinger, M. R.; Eddaoudi, A.; Davies, D.; Janes, S. M. *Cancer Research* **2009**, *69*, 4134.

(203) Ehtesham, M.; Kabos, P.; Kabosova, A.; Neuman, T.; Black, K. L.; Yu, J. S. *Cancer Research* **2002**, *62*, 5657.

(204) Walczak, H.; Miller, R. E.; Ariail, K.; Gliniak, B.; Griffith, T. S.; Kubin, M.; Chin, W.; Jones, J.; Woodward, A.; Le, T.; Smith, C.; Smolak, P.; Goodwin, R. G.; Rauch, C. T.; Schuh, J. C. L.; Lynch, D. H. *Nature Medicine* **1999**, *5*, 157.

(205)   Volkmann, X.; Fischer, U.; Bahr, M. J.; Ott, M.; Lehner, F.; MacFarlane, M.; Cohen, G. M.; Manns, M. P.; Schulze-Osthoff, K.; Bantel, H. *Hepatology* **2007**, *46*, 1498.

(206)   Lawrence, D.; Shahrokh, Z.; Marsters, S.; Achilles, K.; Shih, D.; Mounho, B.; Hillan, K.; Totpal, K.; DeForge, L.; Schow, P.; Hooley, J.; Sherwood, S.; Pai, R.; Leung, S.; Khan, L.; Gliniak, B.; Bussiere, J.; Smith, C. A.; Strom, S. S.; Kelley, S.; Fox, J. A.; Thomas, D.; Ashkenazi, A. *Nat Med* **2001**, *7*, 383.

(207)   Rohmer, S.; Mainka, A.; Knippertz, I.; Hesse, A.; Nettelbeck, D. M. *The Journal of Gene Medicine* **2008**, *10*, 340.

(208)   Yin, P. T.; Shah, B. P.; Lee, K. B. *Small (Weinheim an der Bergstrasse, Germany)* **2014**, *10*, 4106.

(209)   Shah, B. P.; Pasquale, N.; De, G.; Tan, T.; Ma, J.; Lee, K.-B. *ACS Nano* **2014**, *8*, 9379.

(210)   Sun, S.; Zeng, H.; Robinson, D. B.; Raoux, S.; Rice, P. M.; Wang, S. X.; Li, G. *Journal of the American Chemical Society* **2004**, *126*, 273.

(211)   Wu, X.; He, Y.; Falo, L. D.; Hui, K. M.; Huang, L. *Mol Ther* **2001**, *3*, 368.

(212)   Salem, H. K.; Thiemermann, C. *Stem Cells* **2010**, *28*, 585.

(213)   Kim, T.-H.; Shah, S.; Yang, L.; Yin, P. T.; Hossain, M. K.; Conley, B.; Choi, J.-W.; Lee, K.-B. *ACS Nano* **2015**, *9*, 3780.

(214)   Reissis, Y.; García-Gareta, E.; Korda, M.; Blunn, G. W.; Hua, J. *Stem cell research & therapy* **2013**, *4*, 1.

(215)   Johnstone, R. W.; Frew, A. J.; Smyth, M. J. *Nat Rev Cancer* **2008**, *8*, 782.

(216)   Kurbanov, B. M.; Geilen, C. C.; Fecker, L. F.; Orfanos, C. E.; Eberle, J. *Journal of Investigative Dermatology* **2005**, *125*, 1010.

(217)   Arts, H. J. G.; de Jong, S.; Hollema, H.; ten Hoor, K.; van der Zee, A. G. J.; de Vries, E. G. E. *Gynecologic Oncology* **2004**, *92*, 794.

(218)   Deng, Y.; Lin, Y.; Wu, X. *Genes & development* **2002**, *16*, 33.

(219)   Ashkenazi, A.; Pai, R. C.; Fong, S.; Leung, S.; Lawrence, D. A.; Marsters, S. A.; Blackie, C.; Chang, L.; McMurtrey, A. E.; Hebert, A.; DeForge, L.; Koumenis, I. L.; Lewis, D.; Harris, L.; Bussiere, J.; Koeppen, H.; Shahrokh, Z.; Schwall, R. H. *The Journal of clinical investigation* **1999**, *104*, 155.

(220)   Boussif, O.; Lezoualc'h, F.; Zanta, M. A.; Mergny, M. D.; Scherman, D.; Demeneix, B.; Behr, J. P. *Proceedings of the National Academy of Sciences* **1995**, *92*, 7297.

(221)   Urban-Klein, B.; Werth, S.; Abuharbeid, S.; Czubayko, F.; Aigner, A. *Gene Ther* **2004**, *12*, 461.

(222)   Babar, I. A.; Cheng, C. J.; Booth, C. J.; Liang, X.; Weidhaas, J. B.; Saltzman, W. M.; Slack, F. J. *Proceedings of the National Academy of Sciences* **2012**, *109*, E1695.

(223)   Behr, J.-P. *CHIMIA International Journal for Chemistry* **1997**, *51*, 34.

(224)   Hobel, S.; Aigner, A. *Wiley interdisciplinary reviews. Nanomedicine and nanobiotechnology* **2013**, *5*, 484.

(225)   Savla, R.; Garbuzenko, O. B.; Chen, S.; Rodriguez-Rodriguez, L.; Minko, T. *Pharmaceutical Research* **2014**, *31*, 3487.

(226)   Zhang, M.; Garbuzenko, O. B.; Reuhl, K. R.; Rodriguez-Rodriguez, L.; Minko, T. *Nanomedicine* **2012**, *7*, 185.

(227)   Auzel, F. *Chem. Rev.* **2004**, *104*, 139.

(228)   Wu, S.; Han, G.; Milliron, D. J.; Aloni, S.; Altoe, V.; Talapin, D. V.; Cohen, B. E.; Schuck, P. J. *Proceedings of the National Academy of Sciences* **2009**, *106*, 10917.

(229)   Ramasamy, P.; Chandra, P.; Rhee, S. W.; Kim, J. *Nanoscale* **2013**, *5*, 8711.

(230)   Wang, F.; Banerjee, D.; Liu, Y.; Chen, X.; Liu, X. *Analyst* **2010**, *135*, 1839.

(231)   Tian, G.; Gu, Z.; Zhou, L.; Yin, W.; Liu, X.; Yan, L.; Jin, S.; Ren, W.; Xing, G.; Li, S.; Zhao, Y. *Advanced materials* **2012**, *24*, 1226.

(232)   Mattsson, L.; Wegner, K. D.; Hildebrandt, N.; Soukka, T. *RSC Advances* **2015**, *5*, 13270.

(233)   Fischer, S.; Martín-Rodríguez, R.; Fröhlich, B.; Krämer, K. W.; Meijerink, A.; Goldschmidt, J. C. *Journal of Luminescence* **2014**, *153*, 281.

(234)   Wang, Y.-L.; Mohammadi Estakhri, N.; Johnson, A.; Li, H.-Y.; Xu, L.-X.; Zhang, Z.; Alù, A.; Wang, Q.-Q.; Shih, C.-K. *Scientific reports* **2015**, *5*, 10196.

(235)   Su, Q.; Han, S.; Xie, X.; Zhu, H.; Chen, H.; Chen, C. K.; Liu, R. S.; Chen, X.; Wang, F.; Liu, X. *Journal of the American Chemical Society* **2012**, *134*, 20849.

(236)   Gargas, D. J.; Chan, E. M.; Ostrowski, A. D.; Aloni, S.; Altoe, M. V.; Barnard, E. S.; Sanii, B.; Urban, J. J.; Milliron, D. J.; Cohen, B. E.; Schuck, P. J. *Nature nanotechnology* **2014**, *9*, 300.

(237)   Wen, H.; Zhu, H.; Chen, X.; Hung, T. F.; Wang, B.; Zhu, G.; Yu, S. F.; Wang, F. *Angewandte Chemie* **2013**, *52*, 13419.

(238)   Liu, G. *Chemical Society reviews* **2015**, *44*, 1635.

(239)   Berry, M. T.; May, P. S. *The Journal of Physical Chemistry A* **2015**, *119*, 9805.

(240)   Tu, D.; Liu, Y.; Zhu, H.; Li, R.; Liu, L.; Chen, X. *Angewandte Chemie* **2013**, *52*, 1128.

(241)   Wang, Y.; Liu, K.; Liu, X.; Dohnalová, K.; Gregorkiewicz, T.; Kong, X.; Aalders, M. C. G.; Buma, W. J.; Zhang, H. *The Journal of Physical Chemistry Letters* **2011**, *2*, 2083.

(242)   Shang, Y.; Hao, S.; Liu, J.; Tan, M.; Wang, N.; Yang, C.; Chen, G. *Nanomaterials* **2015**, *5*, 218.

(243)   Orchard, A. F.; Thornton, G.; Elsevier.

(244)   Kimura, S.-i.; Arai, F.; Ikezawa, M. *Journal of the Physical Society of Japan* **2000**, *69*, 3451.

(245)   Ferris, M. J.; España, R. A.; Locke, J. L.; Konstantopoulos, J. K.; Rose, J. H.; Chen, R.; Jones, S. R. *Proceedings of the National Academy of Sciences* **2014**, *111*, E2751.

(246)   Hickey, P.; Stacy, M. *Current Neurology and Neuroscience Reports* **2012**, *12*, 376.

(247)   Walsh, R.; DeRosa, M. C. *Biochemical and Biophysical Research Communications* **2009**, *388*, 732.

(248)   Farjami, E.; Campos, R.; Nielsen, J. S.; Gothelf, K. V.; Kjems, J.; Ferapontova, E. E. *Analytical Chemistry* **2013**, *85*, 121.

(249)   Liu, C.; Wang, Z.; Jia, H.; Li, Z. *Chemical Communications* **2011**, *47*, 4661.

(250)   Wang, Y.; Bao, L.; Liu, Z.; Pang, D.-W. *Analytical Chemistry* **2011**, *83*, 8130.

(251)   Olefirowicz, T. M.; Ewing, A. G. *Journal of Neuroscience Methods* **1990**, *34*, 11.